PROCEEDINGS OF THE ROYAL SOCIETY A MATHEMATICAL, PHYSICAL & ENGINEERING SCIENCES

Spirals on the sea

Walter Munk, Laurence Armi, Kenneth Fischer and F. Zachariasen

Proc. R. Soc. Lond. A 2000 **456**, doi: 10.1098/rspa.2000.0560

THE ROYAL SOCIETY

Spirals on the sea

By Walter Munk[1], Laurence Armi[1], Kenneth Fischer[2] and F. Zachariasen[3]†

[1]*Scripps Institution of Oceanography, La Jolla, CA 92093, USA*
[2]*ERIM International, Ann Arbor, MI 48105, USA*
[3]*California Institute of Technology, Pasadena, CA 91125, USA*

Received 23 September 1999; revised 15 December 1999; accepted 20 January 2000

Spiral eddies were first seen in the sunglitter on the Apollo Mission 30 years ago; they have since been recorded on synthetic aperture radar (SAR) images and in the infrared. We present a small sample of images. The spirals are broadly distributed over the world's oceans, 10–25 km in size and overwhelmingly cyclonic. Under light winds favourable to visualization, linear surface features with high surfactant density and low surface roughness are of common occurrence. The linear features are wound into spirals in vortices associated with horizontal shear instability, modified by rotation, in regions where the shear is comparable with the Coriolis frequency. Two models for concentrating shear are presented: a softened version of the classical sharp Margules front, and the time-dependent Lagrangian model of Hoskins & Bretherton. Horizontal shear instabilities and both frontal models favour cyclonic shear and cyclonic spirals, but for different reasons.

Keywords: spirals; shear instabilities; frontogenesis

1. Introduction and outline

The ability to observe the ocean surface from space on a scale of the order of 100 km with resolution of the order of 50 m has revealed a host of phenomena which had not been accessible to traditional ocean sampling. Progress in interpreting some of the phenomena has been very slow. Among the difficulties we emphasize that (i) 'sea truth' coordinated with overhead measurements is difficult and expensive, and (ii) the space platforms move at the order of 10 km s^{-1} and so provide only a few seconds of observations, far too short for developing an insight into the dynamics of the observed features. One incentive here is to provide a framework for future experiments involving sea truths and prolonged stares or multiple looks.

Sections 2 and 3 give a brief account of the fascinating history of the discovery of ocean spirals, followed by the primary observational material. The material poses three basic questions:

(A) How are the spirals wound? What determined the 10–25 km space scales and the one-day time-scale?

(B) How is symmetry broken in favour of cyclonic rotation?

† Deceased 9 December 1999.

(C) What makes the spirals visible?

We note the total absence of spirals within 6° of the Equator (in spite of two dedicated search efforts (Stevenson 1999)), and the remarkable concentration of spiral images in the Mediterranean in the autumn.

Section 4 addresses the question of what makes the spirals visible? Surface-active agents (surfactants), formed mostly by marine organisms, are generally present. The surfactant film is associated with a thin viscous boundary layer and enhanced attenuation of capillary and short gravity waves (Reynolds 1880; Lamb 1932, p. 631). Surfactants are organized by surface straining into coherent surface patterns. The resulting differential roughness (smoothness) makes the strain pattern visible in the sunglitter and in images of radar backscatter. Strain patterns are associated with internal waves, near-surface convection and fronts. Spiral features are likewise made visible by surface straining. We note that spiral features, unlike other surface features, reveal strong cyclonic displacements of ship tracks. This has a bearing on questions A and B.

For the large (50 km) spiral along the Greenland Sea shelf (§ 5) the three foregoing questions have been reasonably answered by field and laboratory experiments (Bruce 1995; Whitehead *et al*. 1990). Pulses of dense water through the Denmark Strait lead to a 'doming' of the deep dense layers. Symmetry is broken by vortex stretching associated with the gravitational collapse, constrained by rotation (the 'Rossby adjustment problem'). The thermal front along the East Greenland shelf provides for the visualization in the infrared images. We find that an analytical model of the associated Rossby adjustment problem (Appendix B) captures many of the observed features, but we have reluctantly abandoned this hypothesis as an explanation for the widespread occurrence of smaller spirals elsewhere.

The remainder of the paper is devoted to alternate hypotheses of spiral formation. Many of the observed features have the signature of the classical cat's-eyes, suggesting a horizontal shear instability. We begin (§ 6) with the well-known Stuart (1967) solution for two-dimensional flow of a homogeneous fluid in non-rotating coordinates (usually applied to vertical shear). With appropriate modifications, the solution can account for many of the observed features. It requires, however, a preconditioning phase during which particles and shear are concentrated along linear frontal zones.

We consider two models of frontal formation. The classical model consists of a density discontinuity along a tilting front, with infinite shear across the front (the Margules front). We have analytically softened a Margules front to derive possible states of density and velocity distributions (§ 7). This analysis, though containing no temporal evolution *per se*, allows us to connect various states of like potential vorticity. The frontal zones are subject to instabilities which favour the formation of cyclonic over anticyclonic shear (question B).

In order to explicitly include time development, we adapt in § 8 the Lagrangian model of Hoskins & Bretherton (1972). This achieves a required preconditioning: a sharp concentration of particles and shear on the cyclonic side of a frontal jet at a time when the anticyclonic side has only weak gradients.

There is more than one way to generate spirals. The fact that some of the data do not fit a given hypothesis does not necessarily mean the hypothesis is wrong. Any convincing 'solutions' will require, as always, a dedicated field experiment.

2. The discovery of spiral eddies

> The almost ubiquitous occurrence (of spiral eddies), whenever submesoscale dynamics was revealed in the sunglitter, indicates that they are perhaps the most fundamental entity in ocean dynamics at this scale. The difficulty is in explaining their structure.
>
> (Scully-Power 1986)

> There is as yet no useful explanation for the origin of oceanic spiral eddies, nor is there information on their life histories and persistence.
>
> (Stevenson 1989)

Space oceanography began in the summer of 1964 when Gifford Ewing convened an 'Oceanography from Space' workshop at Woods Hole. As a result of the early *Gemini* photographs, Robert Stevenson persuaded NASA to mount a Hasselblad camera in the pilot's window starting with the *Gemini XII* flight in November 1966. Among the results were the first photographs of large internal waves (solitons) in the west African waters where they had been first observed on *Meteor* anchor station 366 in 1937 (Defant 1949).

The first photographs of spiral eddies appear to have been taken on Apollo-Saturn 7 in October 1968. Much later, in 1978, *SEASAT*, with its synthetic aperture radar (SAR), generally confirmed the discoveries from crewed spaceflights. The earliest planned observations of spiral eddies took place in 1981 on the first Space Shuttle flight of the *Columbia* (Stevenson 1989, p. 166). An eddy in the Gulf of Oman had been observed on NOAA infrared imagery, and the crew of STS-1 was briefed to look for it. On the first day of the mission, the commander of the *Columbia* observed a series of eddies in the Gulf of Oman (Stevenson 1989, pp. 164–167) and these compared very closely with a NOAA infrared image obtained a few hours after the Shuttle transit. On the very next flight a synthetic aperture radar SIR-A imaged a well-formed cyclonic spiral in the Caribbean. Photographs on the STS-8 mission revealed a field of cyclonic spiral eddies in the South Indian Ocean, each turning in a direction opposite to the anticlockwise rotation in the Northern Hemisphere. For a comprehensive account we refer to Stevenson (1998, 1999).

NASA decided to fly a trained oceanographer on a subsequent mission. Most of the existing material on spiral eddies was collected by Paul Scully-Power during 5–13 October 1984 on flight 41-G (STS-17). Scully-Power (1986) reports in his post-mission analysis:

> On orbit, it soon became clear that by far the most information on ocean dynamics and features can be obtained from the sun glitter ... The available range of useful sun glitter angles is far greater than we had expected, (and) extends from a directly overhead sun angle down to a sun elevation of *ca.* 15 degrees.
>
> About 1700 Earth-looking views (land and ocean) were photographed, of which approximately 25% showed significant ocean dynamics. Far and away the most impressive discovery ... is that the submesoscale ocean (less than 100 km) is far more complex dynamically than ever imagined ... Yet patterns of this complexity could be seen to be interconnected for hundreds and hundreds of kilometers.

> Many times, what you are able to perceive and verbally record cannot be seen on film.

It is for this reason that some of Scully-Power's in-flight recordings are reproduced in Appendix A. There is always a concern that the ocean observations collected by astronauts are biased in favour of coastal scenes.

> No significant site data were lost ... Some of the most important oceanographic discoveries ... were made in ocean areas and on orbits which were not called out in the preflight plan.

This brief account of discovery and the subsequent discussions are skewed toward measurements from crewed satellites. Related measurements from uncrewed spacecraft go back to NORSEX'79 and MIZEX'93 (Johannessen *et al.* 1983, 1987, 1992) with the first reports of cyclonic eddies with 10 km to 15 km diameters, consistent with the observations reported here. A SAR catalogue of ocean features (Johannessen *et al.* 1994*a*) contains some outstanding spiral images (cf. p. 49). There is surprisingly little overlap between the efforts to interpret the results from crewed and uncrewed satellite missions.

3. Space images

Since the start of the Shuttle operations, nearly a million still photographs have been taken by the astronauts. The photographs are kept in the archives of the Johnson Space Center in Houston, Texas. We collected 400 images containing spiral eddies and selected a dozen to illustrate features which we consider crucial to an understanding.† The photographs were taken with handheld Hasselblad 6×6 cm cameras using 100 mm and 250 mm focal length lenses. The Shuttles flew at altitudes ranging from 200 to 400 km. At a typical altitude of 300 km the resolution of these photographs is 50 m or 20 m for the two respective focal lengths.

We suggest that the reader glance at the halftone figures and captions to develop a sense of the features. We will refer to individual halftone figures as we develop our hypothesis.

Most of the images were taken exploiting sunglitter on the sea surface. The spirals are overwhelmingly cyclonic. We have included some images with ship tracks (figures 4, 5 and 7) that give a clear sense of the spirals' rotation since the tracks were originally straight lines on the sea surface. Some of these ship tracks also exhibit sharp breaks allowing an estimate of the magnitude of the shear. A very high resolution image (figure 6) shows line widths between 50 m and 200 m in the western portion of the spiral. All Shuttle images are single snapshots and provide no temporal information. However, a series of three infrared AVHRR (advanced very high resolution radiometer) images at 12 h intervals (figure 12) contains some information on spiral evolution.

† Satellite images of mesoscale features (such as Gulf Stream rings) are not included. They are an order of magnitude larger than the spiral features, and were discovered 20 years earlier.

Figure 1. Spirals on the Black Sea near Istanbul. Four spirals are visible, one interconnected pair within 20 km of the shoreline and one pair *ca.* 50 km offshore. Note the typical streak spacing is of the order of 3 km and when wound up in the spirals can be as small as 1 km. The spiral furthest to the northeast has entrained into its core surfactants from two sources, one to the SW and one to the NE. STS47-74-47 41.5° N, 30.0° E. 18 September 1992.

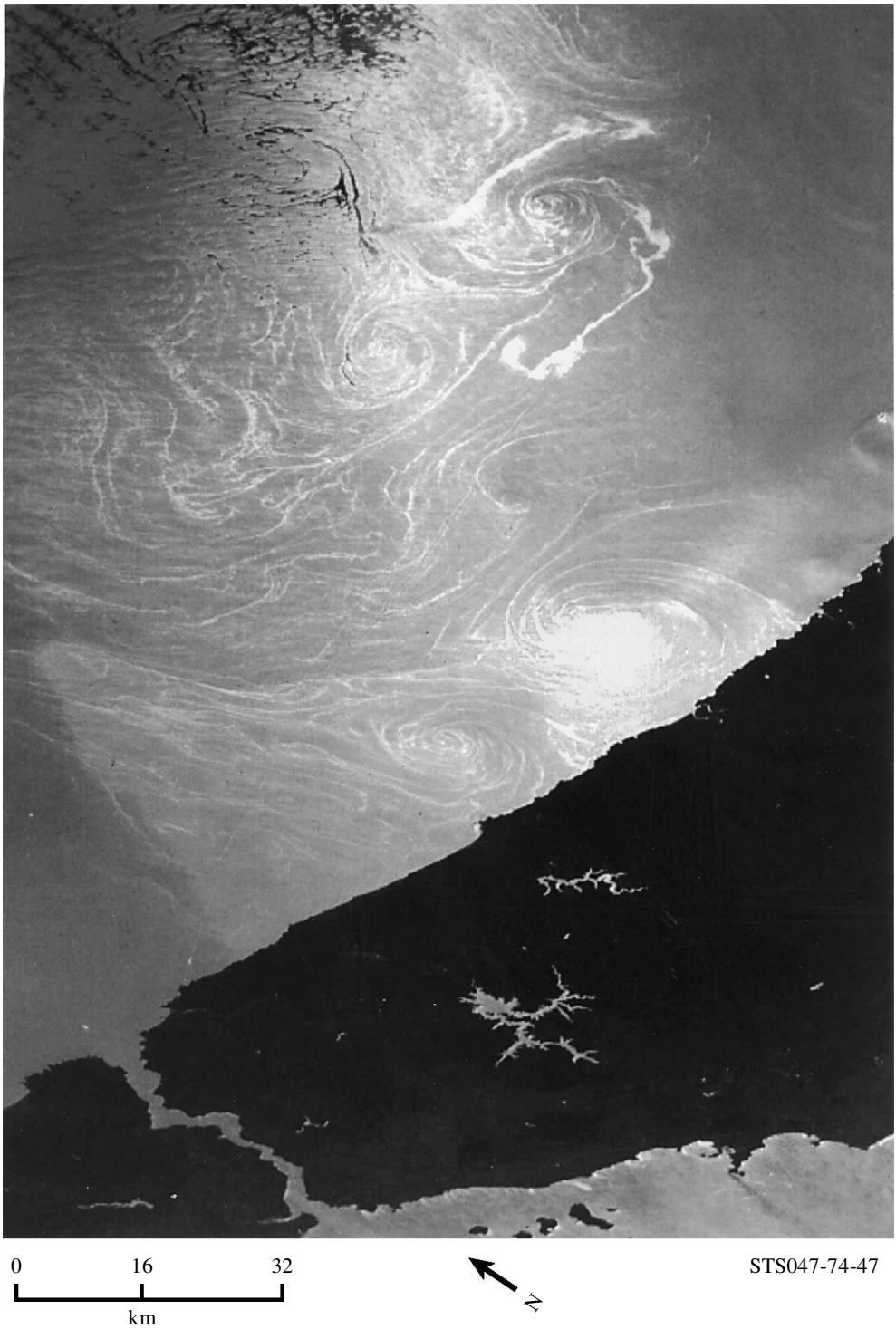

Figure 1. For description see opposite.

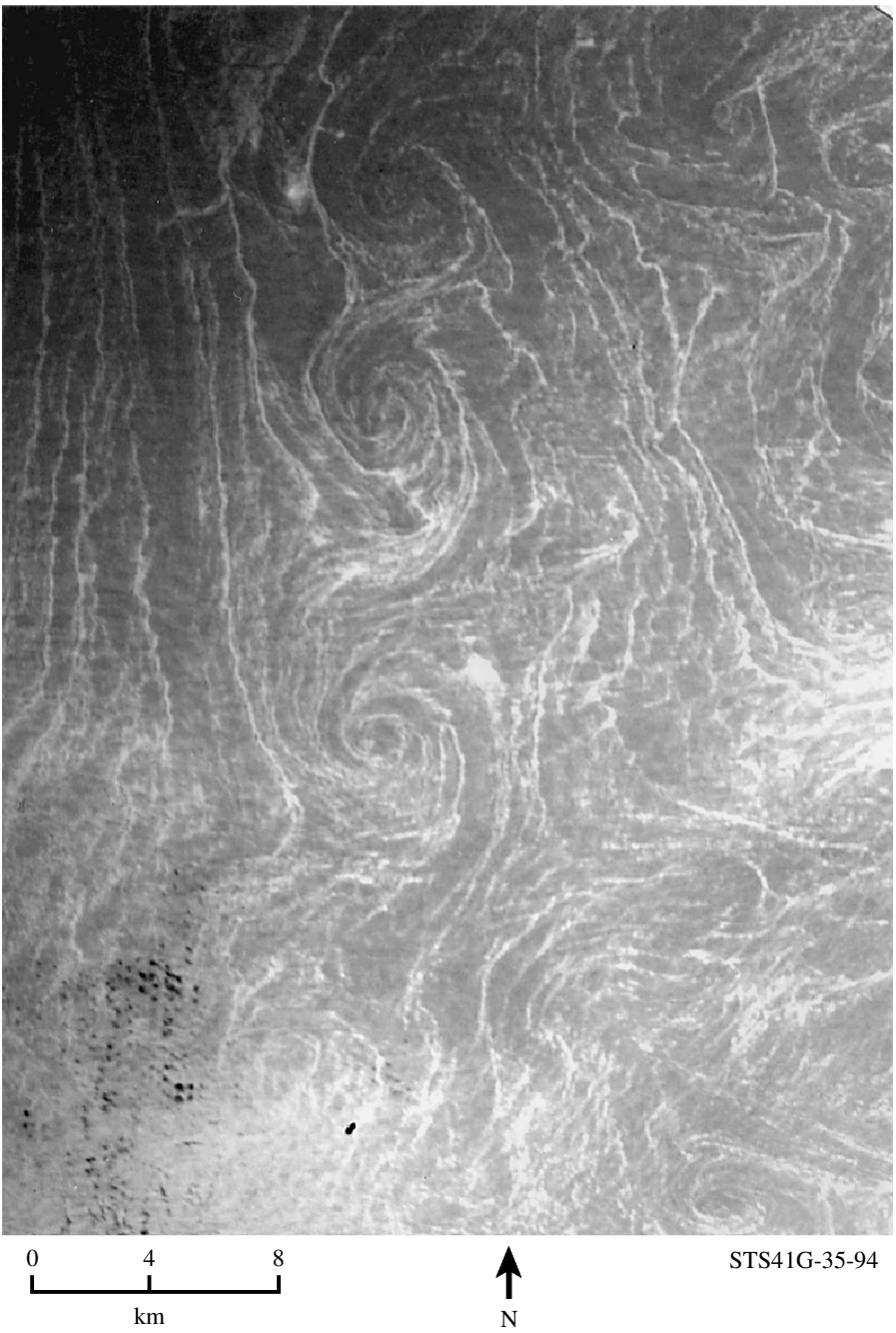

Figure 2. Four interconnected, fully developed spirals in the Mediterranean off Egypt. These are characteristic of horizontal shear aligned along the centres of the spirals. The preconditioning wind field and location of the image is shown in Figure 16. STS41G-35-94 32.0° N, 26.0° E. 7 October 1984.

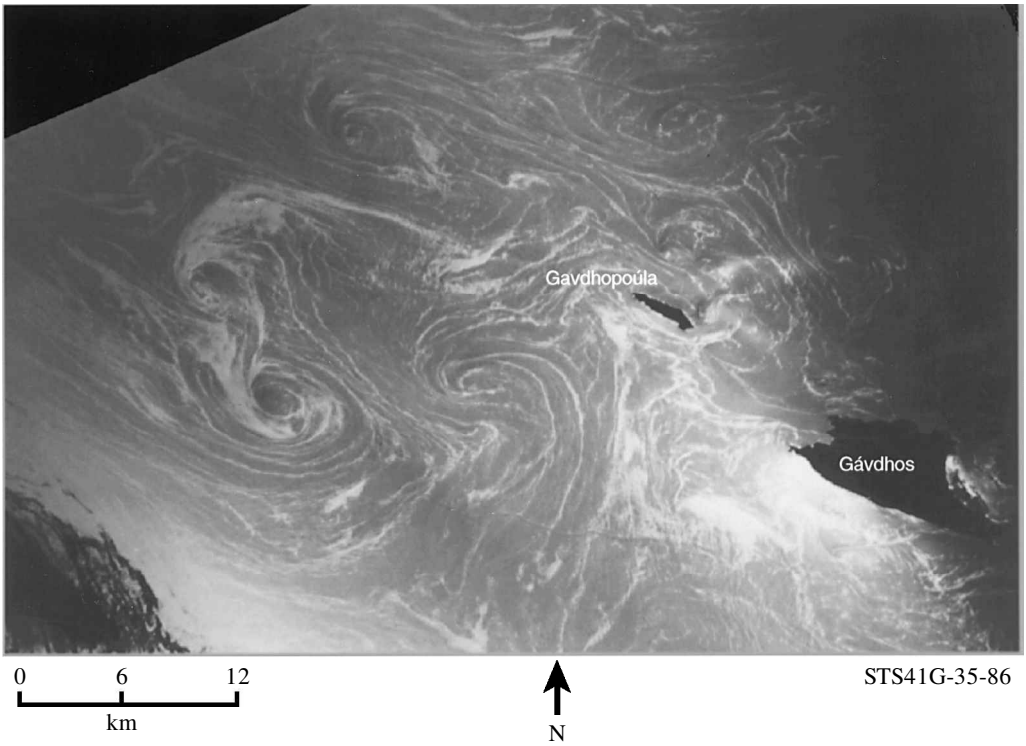

Figure 3. A pair of interconnected spirals in the Mediterranean Sea south of Crete. This vortex pair has a clearly visible stagnation point between the two spirals, the cores of which are aligned with the preconditioning wind field shown in figure 16. STS41G-35-86 34.5° N, 24.0° E. 7 October 1984.

Figure 11 is a synthetic aperture 1994 radar (XSAR) image. Earlier radar sightings at high latitudes were reported by O. M. Johannessen *et al.* (1983, 1987) and J. A. Johannessen *et al.* (1994*a*, *b*). The spiral features are similar regardless of whether imaged in sunglitter, XSAR, or in the advection of a tracer such as temperature or floating ice.

Figures 14 and 15 show the distributions in space and time of year. The September–October peak is biased by a heavy concentration in the Mediterranean, where the near-calm conditions required for sunglitter images are preceded by strong wind events at the end of the Meltemi season (figure 16). Figures 2, 3 and 4 were taken by Scully-Power from the Shuttle mission STS41-G, the ground track of which is shown in figure 16. Even with three images taken within seconds, only a small fraction of the Cretan Sea is covered. The record of the visual sightings (Appendix A) is an important source of information.

Figure 9 also shows cyclonic spirals near Mozambique. Their rotation is clockwise, opposite to the familiar anticlockwise rotation of Northern Hemisphere spirals. The only examples of incipient anticyclonic spirals that we have found occur in the wakes of islands (figure 10). There are cyclonic spirals downstream of the southern separation point of Santa Catalina island in the Gulf of California. The incipient anticyclone which forms at the northern separation point does not persist.

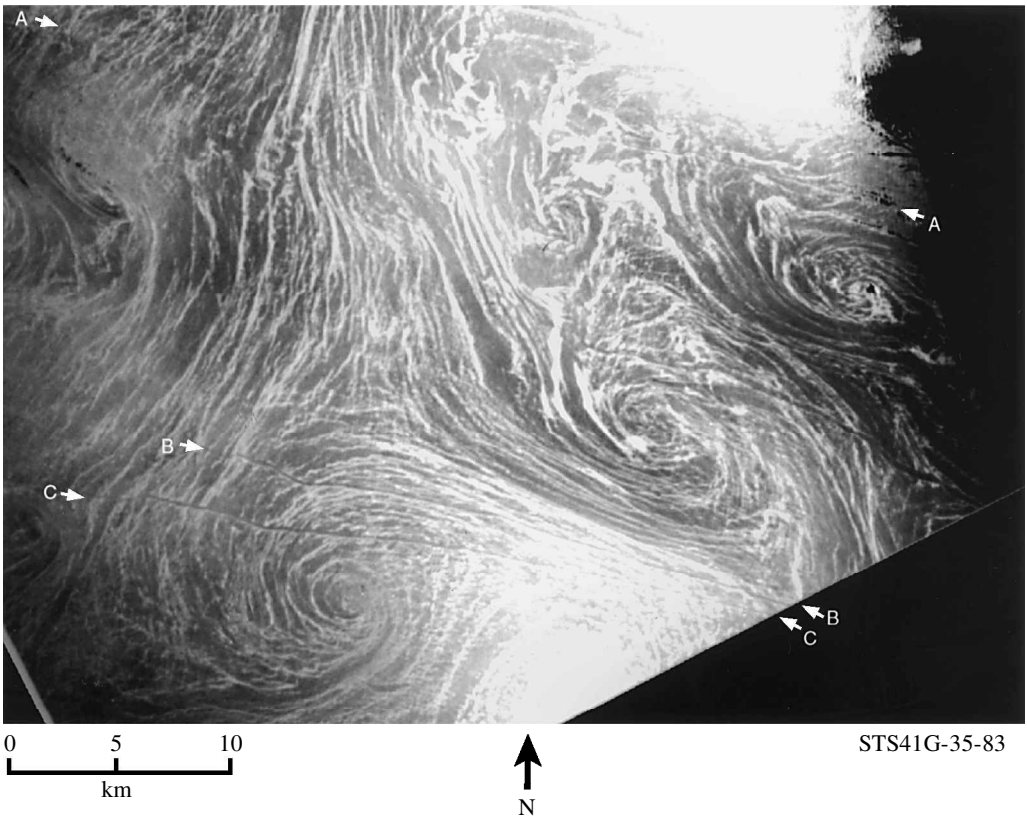

Figure 4. Spirals in the Andikithiron Channel northwest of Crete (see figure 16 for location and preconditioning wind field). Ship tracks are labelled A, B, C. Note how ship tracks B and C are distorted as the vortex core of the spiral is approached. STS41G-35-83, 35.5° N, 23.0° E. 7 October 1984.

4. What makes spirals visible?

There is a rich menu of features on the sea surface, variously referred to as streaks, lines, stripes, bands, lanes, windrows, streamers, tide-rips, suloys, slicks; a confusing mixture of different physical processes and different words for the same process. But what has become increasingly clear since the first days of space images is that the straining and damping of capillary and short gravity waves is an astonishingly sensitive indicator of what goes on above and beneath the surface. We need to discuss the visibility issue in a broader context than just with reference to spirals; these are only one manifestation of surface straining.

(*a*) *Surface signature of differential roughness*

Slicks are associated with concentrations of surfactants. Moum *et al.* (1990) obtained a quantitative measure with a towed microlayer sampler and found sharp maxima in surfactant concentration off Pt Arena, California, coincident with maxima in surface convergence. It might be thought that the presence of surfactants is a rather special circumstance, but it turns out to be the rule rather than the

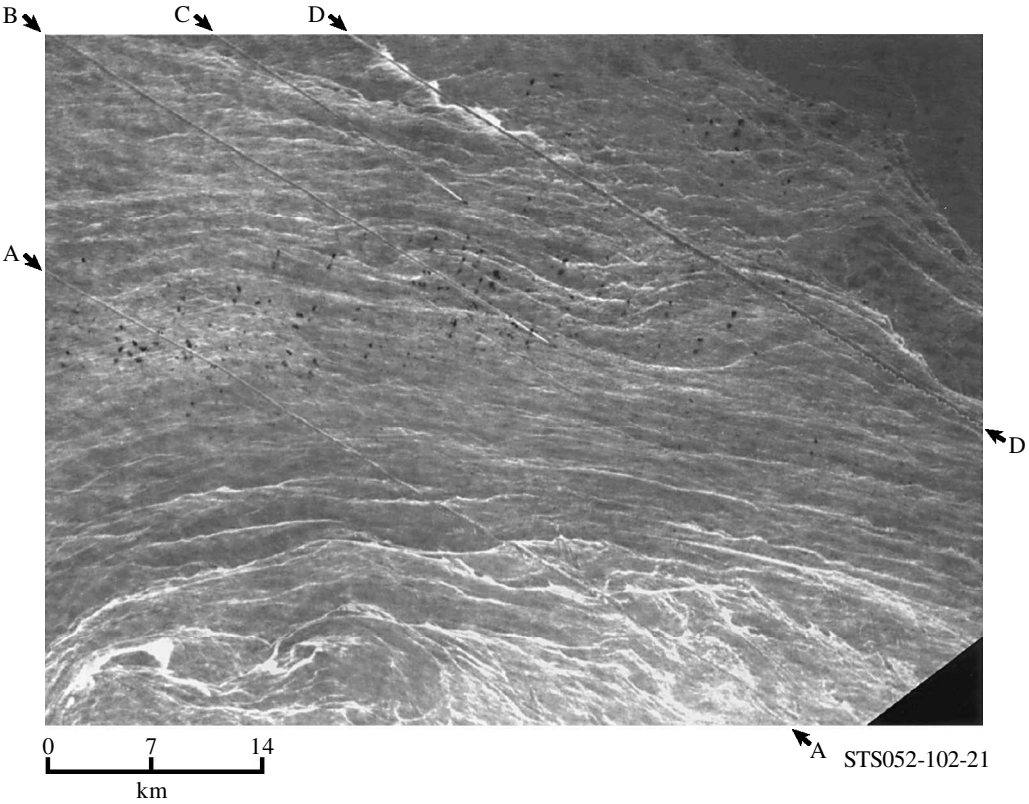

Figure 5. Ship tracks (A, B, C, D) in the Arabian Sea. The ships are visible for tracks B and C and for these young tracks, the ship wakes are undistorted. The oldest ship track, A, exhibits cyclonic offsets. The basic large-scale shear shows the beginnings of a developing Kelvin–Helmholtz instability across the centre of the image between ships B and C. STS52-102-21, 20.6° N, 65.4° E. 26 October 1992.

exception. Microlayer surfactants originate from at least two natural sources: the biological activities of plankton and fish, and petroleum oil seepage (MacDonald *et al*. 1993). Natural biogenic surface films are found in all parts of the oceans (Peltzer *et al*. 1992). But by no means are they evenly distributed; there is a relatively high level of occurrence in marginal seas and a relatively low level in the Southern Hemisphere (Bresciano *et al*. 1998).The films are detected visually at light winds. Off the Norwegian coast, Espedal *et al*. (1998) noted 40% of surfactant coverage for 2.5 m s^{-1} winds, but only 5% for 5–10 m s^{-1} winds. The coverage is below 1% for winds exceeding 12.5 m s^{-1}.

The concentration of surfactant is associated with nearly inextensible surface films which dissipate waves at the short wavelength limit of the spectrum, namely capillaries and the shortest gravity waves. Published values for film thicknesses required to dampen capillary waves and produce a visible effect are of the order of 0.01–0.1 μm. On a smooth surface the Sun appears as a single reflection. Sunglitter is governed by the reflection from very many wave facets of a roughened surface. The glitter pattern depends on the wave slope statistics (Cox & Munk 1954). This is heavily biased towards capillaries and short gravity waves, the very components that are

Figure 6. A high-resolution image (from National Technical Means) just west of Peloponnesus. Note the sharpness of some of the lines in the western quadrant. 37.6° N, 21.4° E. October 1983.

Figure 7. Ship tracks in the Ionian Sea. Tracks A and C are young with the ships visible. Track A shows minor distortion during passage through the developing core, the centre of which is *ca.* 3 km aft of the ship. Ship track B is old and shows significant offsets at cyclonic sharp fronts coincident with streaks. The rendition of the streaks changes from light in the inner sunglitter to the upper left, to dark in the outer sunglitter in the lower and right hand portion of the image. STS41G-38-60.

damped by surfactants. Differentially smooth lines will be dark in the outer glitter, where reflection into the camera requires large RMS slopes and bright in the inner glitter (figure 17 inset). Some of the same lines can be followed from dark to bright (figures 1 and 10).

The shortest capillary wavelength greatly exceeds the wavelength of light, and so the glitter is governed by geometric optics. Monostatic radar backscatter, however, is

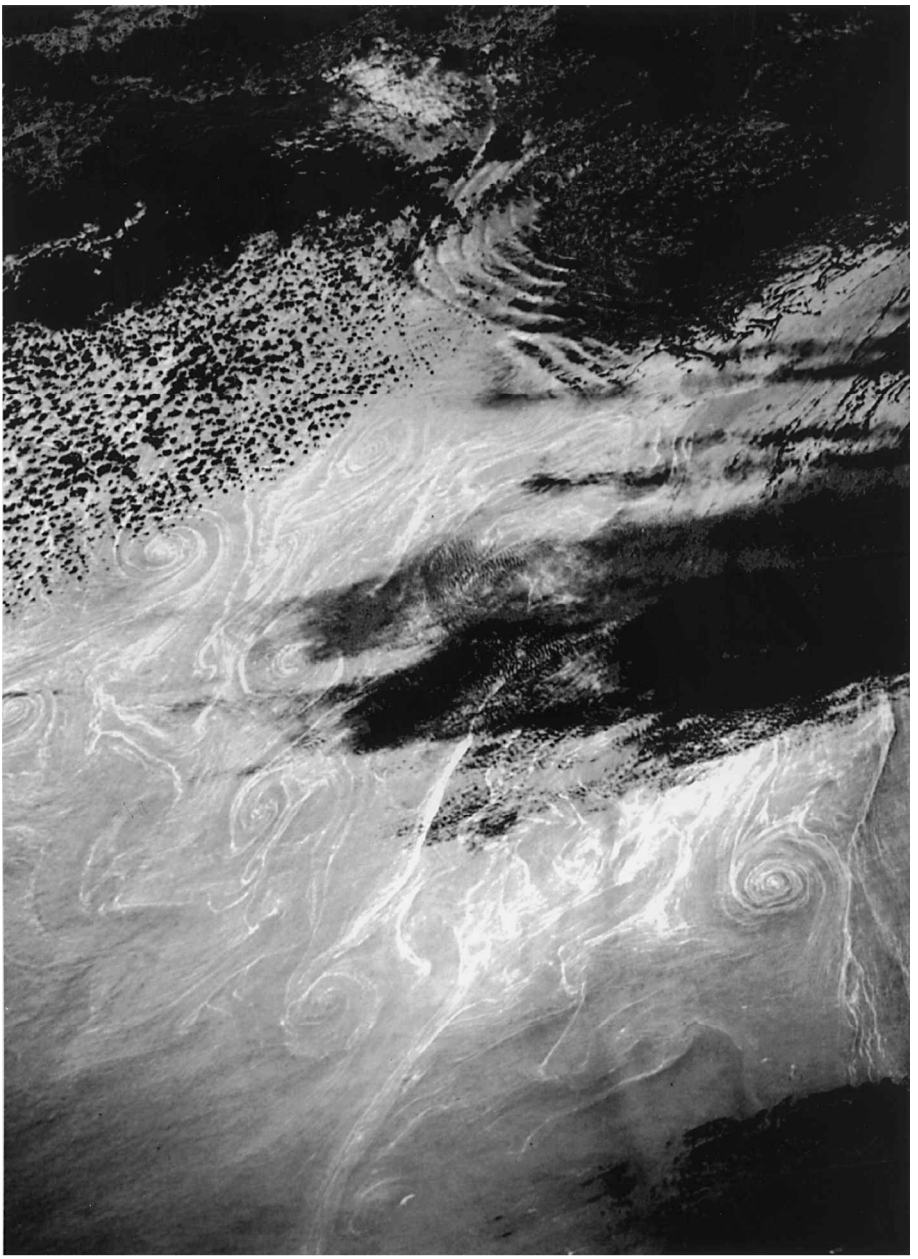

Figure 8. Radiating internal solitary waves in the upper part of the image are clearly distinguishable from the interconnected spirals in the Sea of Japan. Splotches are cumulus clouds and their shadows. STS47-94-86, 39.7° N, 128.6° E. 16 September 1982.

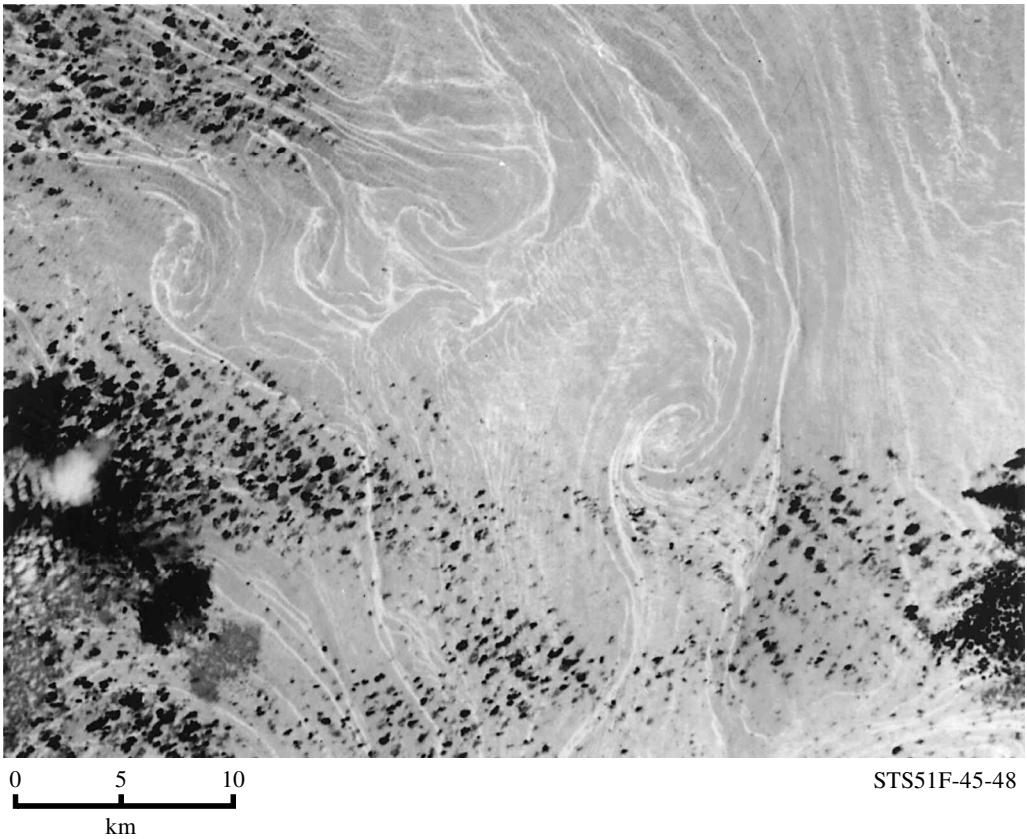

Figure 9. Cyclonic spirals in the Southern Hemisphere near Mozambique. Note clockwise rotation is opposite to that seen in the Northern Hemisphere. Splotches are cumulus clouds and their shadows. STS51F-45-48, 22.3° S, 37.5° E. 3 August 1985.

highly selective. For a given radar wavelength only those components of the surface wave spectrum which are in Bragg resonance determine the image intensity. X-band radar resonates with capillaries (wavelengths 1.8–3.2 cm for 60° to 30° angles of incidence), C-band with very short gravity waves (3.3–8.7 cm) and L-band with short gravity waves (14–25 cm). At low winds, C-band SAR backscatter is typically reduced by 2–3 dB (Espedal *et al*. 1998).

Contrary to folklore, the energetic longer surface waves are not appreciably damped by the surface film. The situation is then entirely different. The appropriate treatment is based on the interaction of capillary and short gravity wave trains with moving media (Bretherton & Garrett 1969; Phillips 1977, pp. 74–80; Lyzenga & Marmorino 1998). Maximum roughness occurs where the wave energy flux is blocked by opposing currents. We can have the concurrent occurrence of differentially smooth 1 cm waves and differentially rough 1 m waves (figure 17). Measured radar cross-sections during SARSEX in 1984 off the New York Bight generally agree with these considerations (Apel *et al*. 1998; Gasparovic *et al*. 1988). So we have the situation where the perception of the convergence lines depends strongly on where and how you observe: the lines appear bright in the inner sunglitter and dark in the outer glitter (cf. fig-

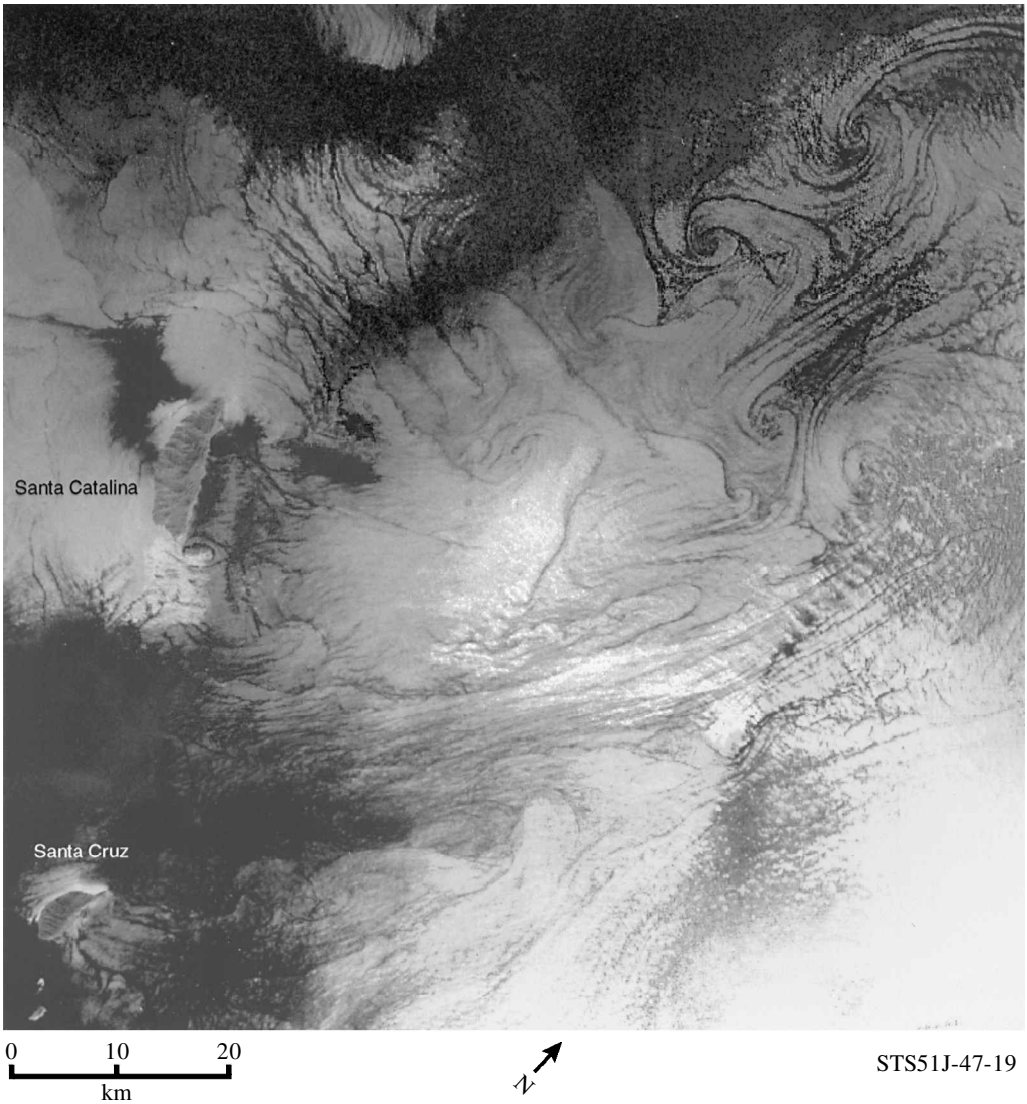

Figure 10. Separation vortices formed downstream of Santa Catalina Island in the Gulf of California. Cyclonic vortices formed at the southern separation point persist downstream to the east whereas the incipient anticyclonic vortex formed at the northern separation point does not persist. Note the dark spiral streaks in outer glitter in the NE corner. STS51J-47-19, 26.0° N, 110.5° W. 6 October 1985.

ure 7); dark on high frequency radar images (figure 11) and bright on low frequency radar.

The association of surface slicks with internal waves goes back to Ewing (1950). Their signature is easily recognized, especially that of organized nonlinear wave packets (figure 8). But internal waves are poor at concentrating surfactants. Convergence and divergence zones move across the surface in phase with internal wave troughs and crests, so that a particular Lagrangian surface element is alternately stretched

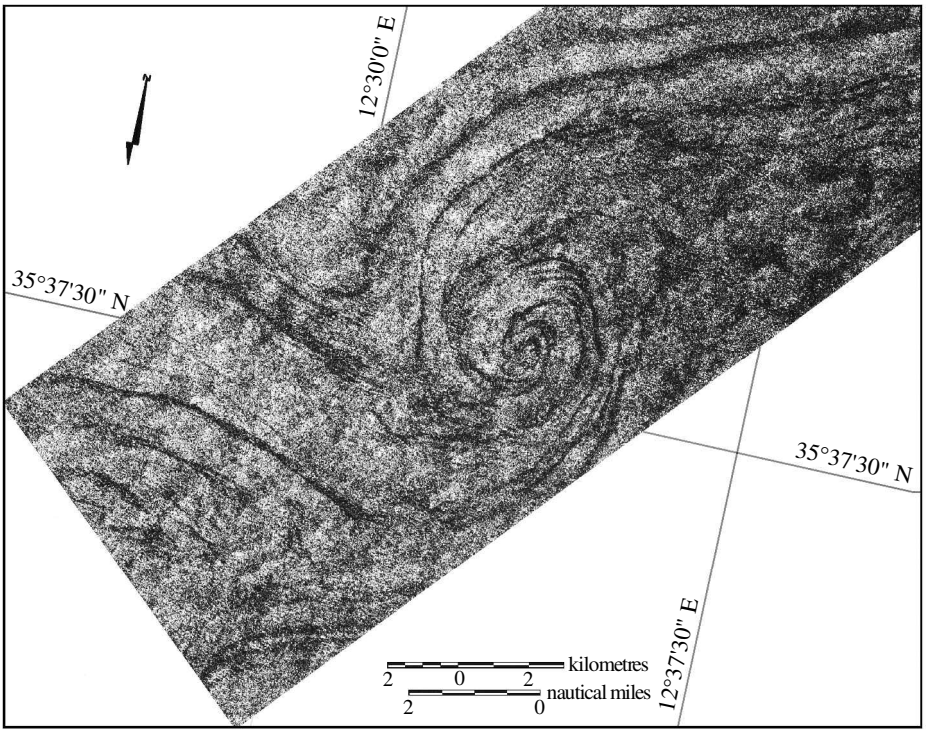

Figure 11. Spiral in the Mediterranean Sea visualized with Shuttle XSAR. The streaks are differentially smooth. STS068-28-03, 35.7° N, 12.6° E. 9 October 1994.

and compressed. Larger effects can be associated with processes having a monotonic strain pattern.

(*b*) *Convective lines*

Some linear atmospheric features, perhaps the majority, are related to convection in the oceanic and atmospheric layers. The spacing between convergence lines is of the order of three times the layer thickness. For the oceanic case (known as Langmuir convection) the spacing is of the order of 300 m, and the line thickness of the order of 30 m, too narrow to be well resolved on these images.

Flament *et al*. (1994) observed coherent horizontal temperature streaks at least 50 km long off the coast of California. They attribute the streaks to the surface winds associated with helical circulation rolls in the atmospheric boundary layer, with a possible upper-ocean participation to the atmospheric forcing (Brown 1980; Thompson *et al*. 1983; Gerling 1986; Etling & Brown 1993; Johannessen *et al*. 1994*b*). The rolls are aligned slightly to the left of the geostrophic wind at intervals of a few kilometres, 2–4 times the thickness of the atmospheric planetary boundary layer. The governing process appears to be a convective instability modified by an underlying velocity shear that imposes linearity on the features. This was recognized by Woodcock (1942) from observations of the soaring of herring gulls in an unstable atmosphere, showing a pronounced transition from circular to linear soaring. The strategy of linear soaring was limited to winds above (but not much above) 7 m s^{-1}.

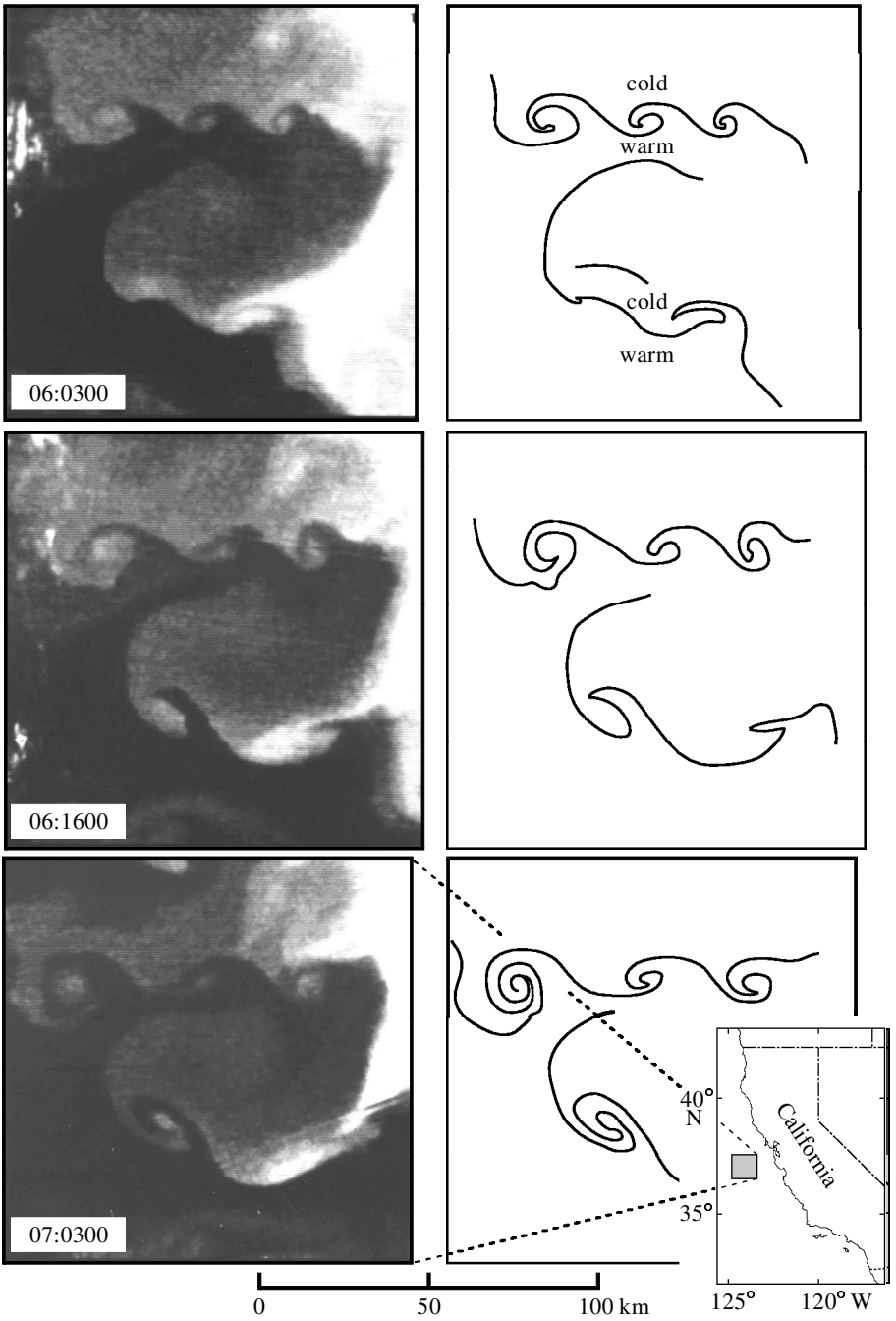

Figure 12. A series of NOAA 7 infrared satellite images collected 6–7 May 1981, showing the development over a day of shear instabilities at the southern boundary of upwelling filaments off Monterey, California. These filaments are narrow jets that advect cold (light in the false colour image) water offshore (Flament & Armi 1985).

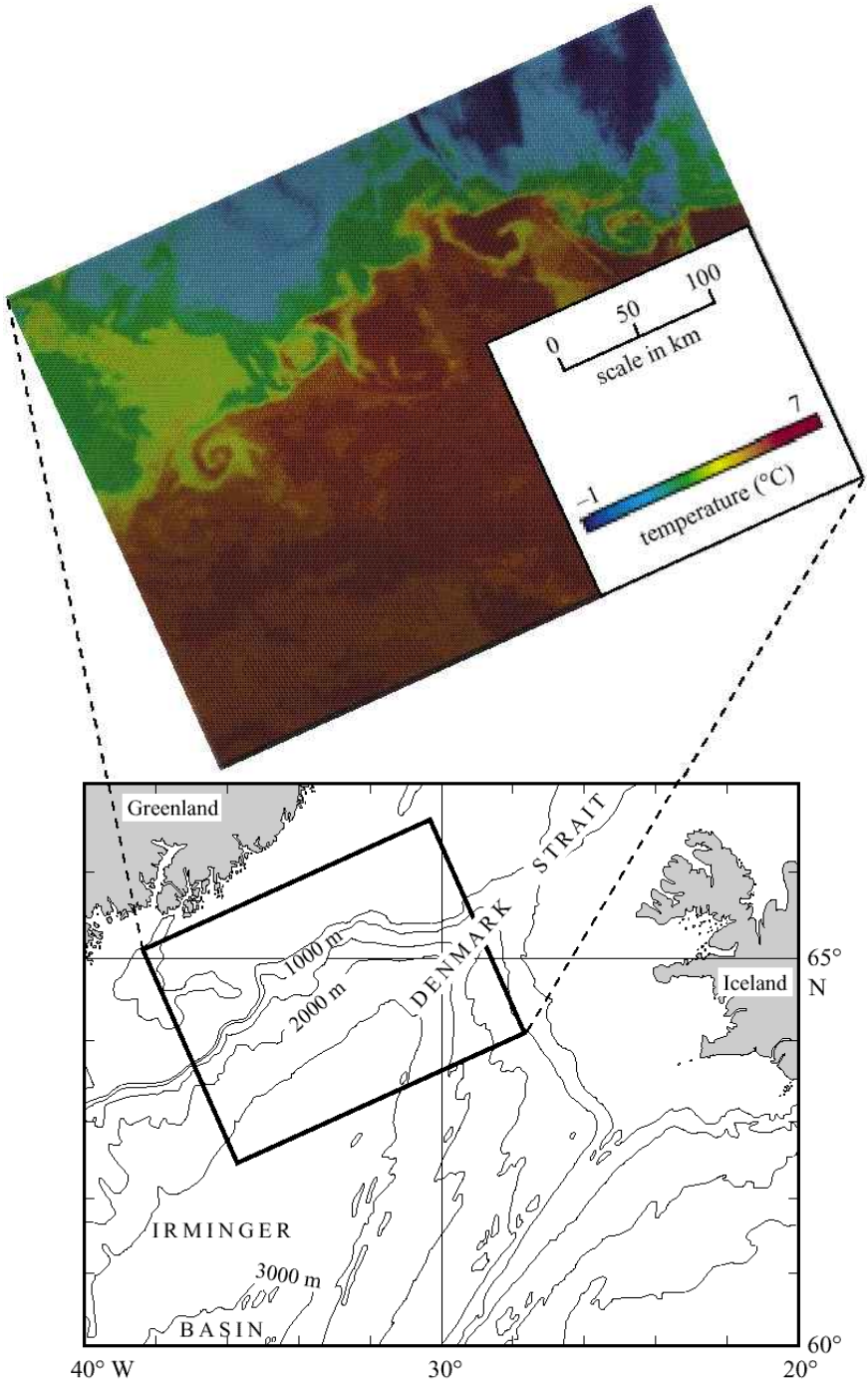

Figure 13. NOAA-11 infrared image of cold cyclonic spiral eddies (20–40 km diameter) along the edge of the East Greenland shelf (from Bruce 1995).

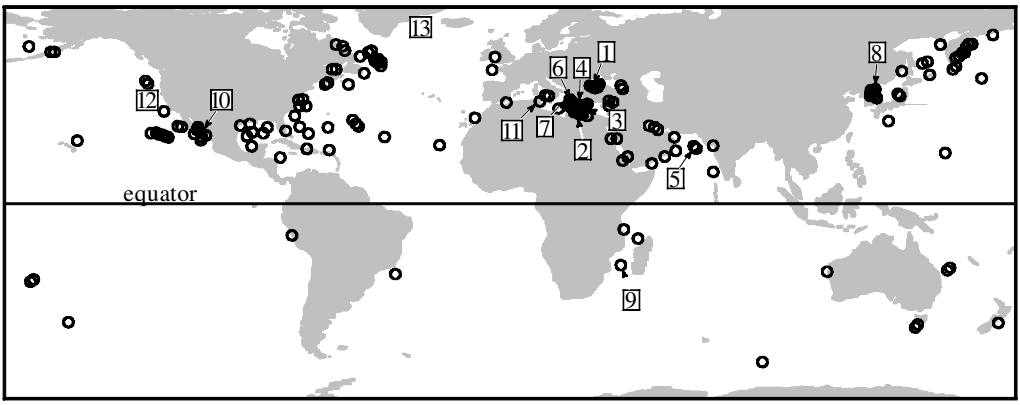

Figure 14. Distribution of spiral eddies from Scully-Power's (1986) visual observations and our collection of 400 images. The 13 numbered locations refer to the halftone figures.

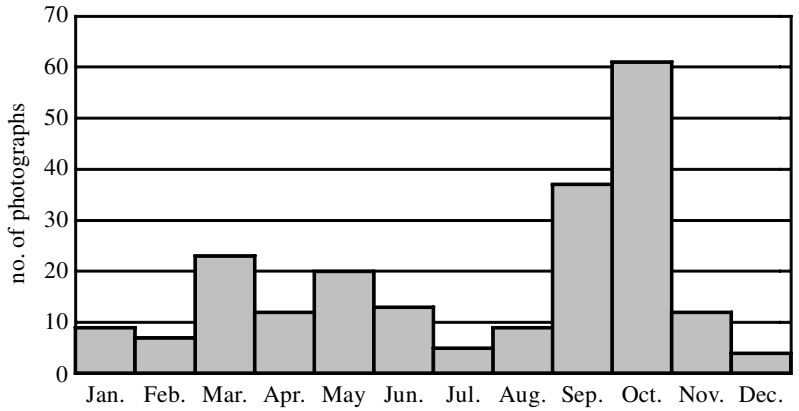

Figure 15. Distribution of the 400 spiral images by month.

The linearity of the convective features can be traced to the presence of an underlying moderate wind shear (gulls understand this perfectly well). We conclude that the astounding horizontal dimension of some linear features in the satellite images is a manifestation of the scale of the underlying wind structure.†

(*c*) *Shear lines*

One source of evidence comes from the intersection of the lines with the centreline wake‡ generated by the passage of surface ships. In some instances, mostly associated

† Radar polarization may give a clue as to the origin of the linear features (Lavrova *et al.* 1998). Horizontally polarized (HH) radar images tend to emphasize specular reflections which clearly show the internal wave field (akin to sunglitter in optical images). Vertically polarized (VV) radar images show a transition of linear to cellular surface structure with increasing $T_{\mathrm{water}} - T_{\mathrm{air}}$, associated with Bragg scattering (less so in HH) from capillaries that are modulated by the convective currents.

‡ Surfactants also play an important role in the signature of the centreline wake (Peltzer *et al.* 1992). A persistent feature is a pair of bands of compacted surface-active material along the edges of the (slowly spreading) centreline wake. The bands appear as dark lines ('railroad tracks') in SAR images and the outer sunglitter.

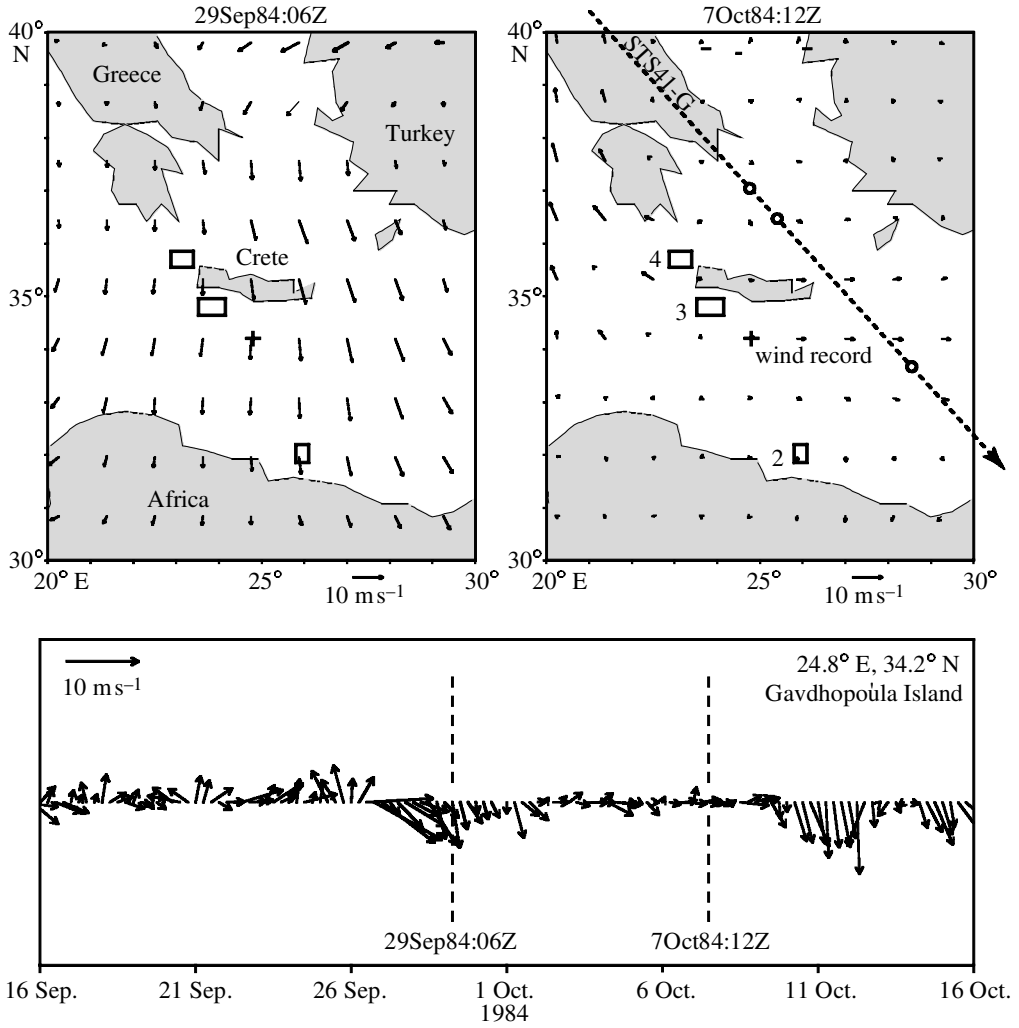

Figure 16. Winds in the Cretan Sea (V. Kourafalou, personal communication). □ show the areas covered by figures 2, 3 and 4 photographed by Scully-Power on Mission STS41-G from positions ○. Wind vectors in the lower panel were recorded at position +. Calm conditions during overflight contrast with strong north-northwesterlies during the previous week.

with the spiral structure, there is a sharp break of the wake as it crosses lines and bands; the vast majority of lines do not exhibit such a break (figures 4, 5 and 7). The breaks are in a direction consistent with cyclonic shear. Estimates of the width of the lines (100 m) and the age of the wake (1 h) suggest shears of the order of $10^{-3}\ \mathrm{s}^{-1}$, in agreement with the earlier estimates of Scully-Power (1986). Ochadlick *et al.* (1992) obtain velocity differences of $0.18 \pm 0.13\ \mathrm{m\ s}^{-1}$ from seven measurements across 200 m slick lines, yielding $10^{-3}\ \mathrm{s}^{-1}$ for the average shear. A similar value has been reported by Sheres *et al.* (1985) from the refraction of swell passing through a shear zone. These estimates play an important role in our attempt to interpret the spiral features.

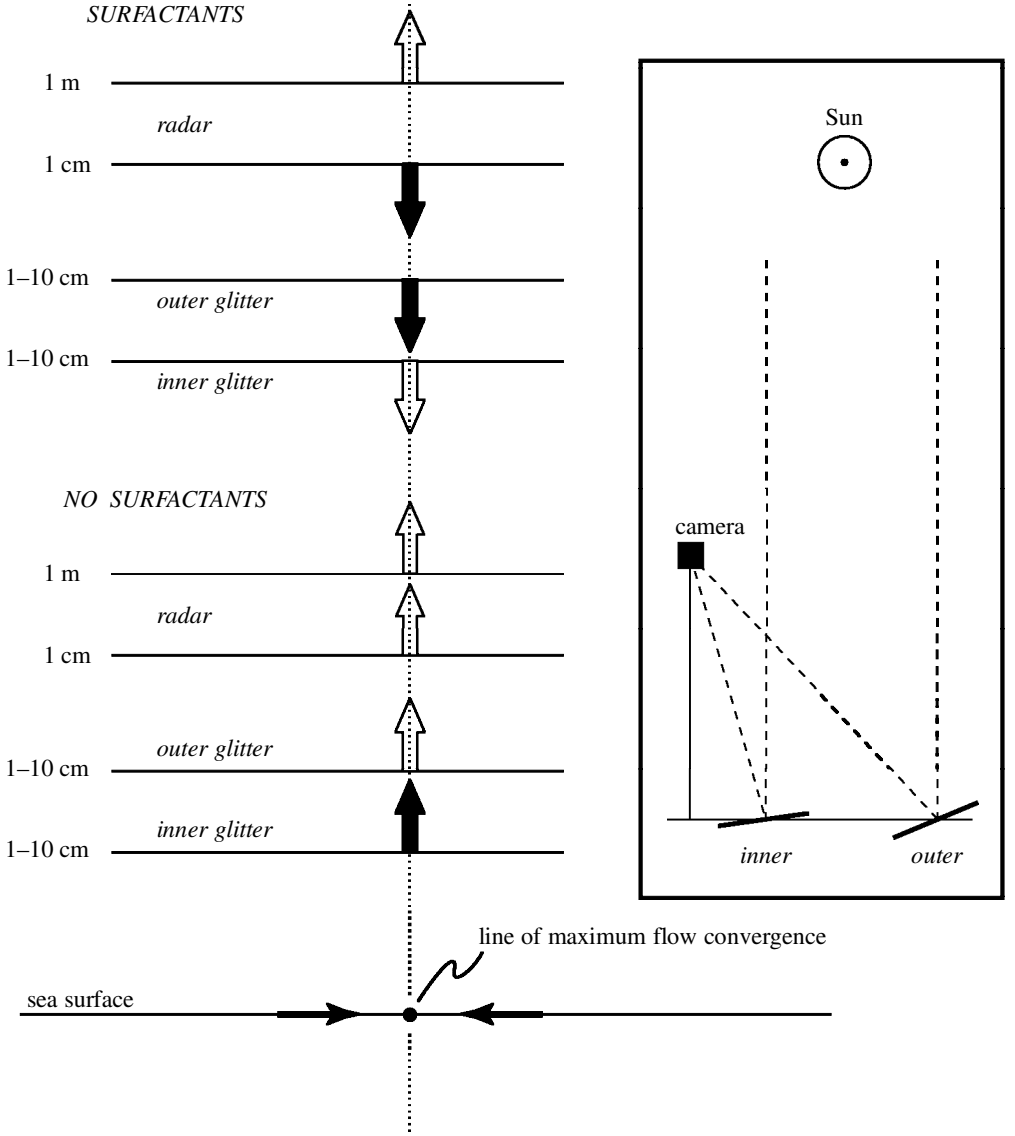

Figure 17. Upward/downward arrows designate rough/smooth sea surface along a line of maximum surface flow convergence; open/filled arrows designate light/dark line on image. Incoming parallel rays from the Sun (at infinite distance) are reflected by the rippled surface toward the camera, requiring steep wave facets in the outer glitter, and small slopes in the inner glitter.

In a paper entitled 'A line in the sea', Yoder *et al.* (1994) report coordinated observations from space, air and sea of a line stretching for hundreds of kilometres in the equatorial Pacific. The line marks the boundary between the 24 °C waters of the South Equatorial Current and the 28 °C waters of the North Equatorial Counter Current. Simultaneous shipboard measurements reveal extremely high concentrations of buoyant diatoms along the line.

Flament & Armi (2000) report a cyclonic front with high vertical stratification

and an intense horizontal current shear off the California coast. A lower limit to the frontal shear of the order of $10^{-3}\,\mathrm{s}^{-1}$ was obtained from the deflection of the ship track at a constant heading. The cross-frontal convergence was at least $0.1\,\mathrm{m\,s}^{-1}$ over 1 km or $10^{-4}\,\mathrm{s}^{-1}$. The following description is of interest: 'A 20-m wide accumulation of debris, consisting of seaweeds ... , ship refuse, sonobuoy containers, and bales of *Canabis Sativa*, was found along the sharp front ... The drifters launched east of the jet were retrieved in this debris line, which extended straight from horizon to horizon.'

Lyzenga & Marmorino (1998) observed long linear slicks near the edge of the Gulf Stream, and computed a mean surface convergence of *ca.* $0.2 \times 10^{-4}\,\mathrm{s}^{-1}$ and a cyclonic vorticity of $10^{-4}\,\mathrm{s}^{-1}$, based on currents inferred from the motion of the slicks. They concluded that the location of the slicks were essentially random but their orientations were determined by the current gradients. They further postulated a set of conditions (on the current gradients) required for the formation of such slicks.

We summarize as follows. To generate smooth elongated lines requires (i) the collection of irregular surfactant patches into contiguous areas with near 100% surfactant coverage, at the expense of neighbouring areas, and (ii) the deformation of these contiguous areas into organized elongated stripes. For internal waves above the inertial frequency the deformation is of the convergent–divergent type, so that the divergent orbital flow field accounts for both (i) and (ii). The image of the radiating internal solitary waves in figure 8 owes the regularity and periodicity of the arcs to the organized structure of the divergence field. Similar considerations apply to the ubiquitous wind streaks associated with atmospheric rolls and aligned with the wind field. They owe their linearity to the coherence of the wind structure.

We distinguish the signatures of internal waves and wind streaks from another class of lines associated with regions of major current shear and regions of frontal formation. We refer to these as 'shear lines'. The deformation includes a stretching component oriented along a principal axis of strain rate (Lyzenga & Mamorino 1998). The component does not contribute to the collection of surfactants; so that steps (i) and (ii) are then quite distinct.

Most of the linear features in the halftone figures are probably wind streaks associated with previous wind events prior to the calm conditions favourable to their detection in the sunglitter. They may owe their astounding persistence to the radiation stress divergence of the short damped waves (Thorpe 1995), or to variations in the Stokes drift associated with wave refraction (Garrett 1976; Phillips 1977, p. 290; Leibovich 1983). Some of the lines are shear lines. Eddies are made visible through their action of twisting linear features into a spiral configuration. The fact that the shear lines are relatively prominent is not an accident. The frontal formation which we propose to be a precondition for the formation of spiral eddies is also favourable to the formation of shear lines. The linearity is simply a consequence of the fact that frontal processes are inherently anisotropic.

5. Spirals along the East Greenland shelf

We start with a situation that is fairly well understood. Cold cyclonic spiral eddies have been detected along the edge of the East Greenland shelf. According to Bruce (1995) these are formed by dense water overflowing the sill of Denmark Strait in 1.5–2.5-day pulses and subsequently moving southwestward along the shelf (figure 13).

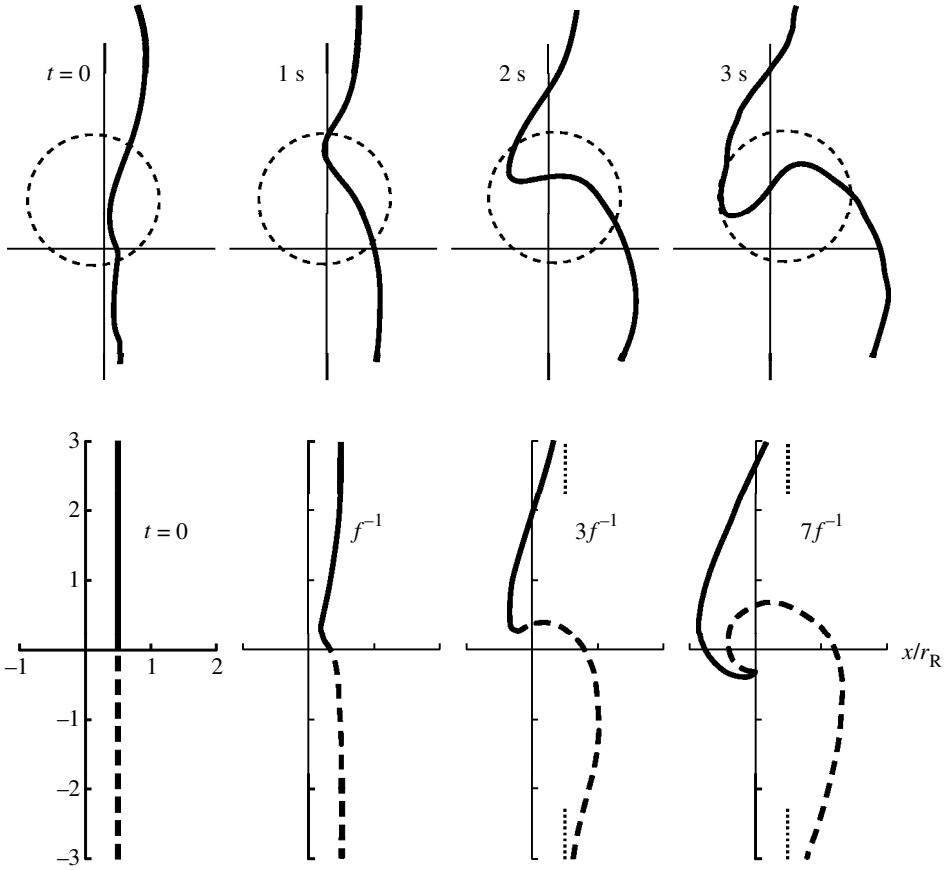

Figure 18. (Top) Laboratory experiment of Greenland Sea eddy formation (adapted from Whitehead (1990)), showing time evolution of a streak of dye injected just under the surface relative to an eddy moving slowly 'eastward'. The eddy was formed by squirting dense salt water upward along a sloping bottom in a rotating tank filled with fresh water. (Bottom) Computed deformation associated with the cylindrical Rossby adjustment problem. A line along $x = 0.5r_{\mathrm{R}}$ (r_{R} is Rossby radius of deformation) is strained by the velocity field associated with the collapse of a cylindrical cone of initial radius $r_0 = r_{\mathrm{R}}$. Subsequent to an initial inward bending for small positive y, the line is distorted into a spiral-like feature, but remains along $x = 0.5r_{\mathrm{R}}$ for $|y| \to \infty$ (dashed). The time $t = 7f^{-1}$ corresponds roughly to one day.

The cyclonic rotation is accounted for by the vortex stretching associated with the collapse of the heavy water bubbles.† A model was tested in the laboratory by Whitehead *et al.* (1990). The eddy was formed by squirting dense salt upward along a sloping bottom in a rotating tank filled with fresh water (figure 18). A dye streak injected just under the surface was distorted in accordance with the early development of a spiral formation. Four other methods (including one as simple as placing an ice cube in the water over the sloping bottom) led to comparable eddy forma-

† This is in contrast to the very stable *anticyclonic* 'Meddies' at mid-depth due to the interior injection of mixed Mediterranean water and associated mid-water high pressure distribution.

tion, suggesting 'that they are robust structures which might be anticipated under a variety of conditions'.

To gain further insight, we have derived a solution to the so-called 'Rossby adjustment problem' for an initial conical peak in the lower layer of a two-layer fluid (Appendix B). The remarkable finding by Rossby (1938) is that an initial localized disturbance does not collapse to zero for $t \to \infty$ (as it would in a non-rotating system) but indefinitely retains a geostrophically balanced residual circulation (see Gill 1982, § 7.2). An initial line of particles is twisted into spiral configuration in a time of the order of one day, resembling the Whitehead experimental result.

The model accounts simply for the three questions posed in the introduction. The scaling follows from Rossby dynamics, and symmetry is broken by vortex stretching associated with the collapse of the initial dome. The thermal front along the East Greenland shelf provides for the visualization in the infrared images.

But we have abandoned, with reluctance, the foregoing model as an explanation for the widespread occurrence of spiral features. For one thing, the buoyancy flux associated with the bubbles of dense water through Denmark Strait cannot be generally matched. Suppose we have a two-layer ocean with $\Delta\rho/\rho = 10^{-4}$. This corresponds to a temperature change by $\Delta T = a^{-1}\Delta\rho/\rho = 0.4\,^{\circ}\mathrm{C}$ for $a = 2.5 \times 10^{-4}\,^{\circ}\mathrm{C}^{-1}$. The change in heat energy of a layer of thickness $h = 10$ m is then

$$\frac{\Delta E}{\text{Area}} = \rho c h \Delta T = 10^3 \cdot 4 \times 10^3 \cdot 10 \cdot 0.4 = 1.6 \times 10^7 \text{ J m}^2,$$

where c is the specific heat of water. In order for this to happen in a time 10^4 s (with no appreciable geostrophic adjustment), it requires a surface flux of 1.6×10^3 W m^2, far too large to be plausible.

What is required here is a more sudden injection of negative buoyancy than can be expected from heat loss through the air–sea boundary. We have considered the breaking of internal waves over a shoaling bottom, injecting globs of dense fluid onto an upper lighter fluid. Recent work on coastal solitons have documented violent breaking processes associated with considerable buoyancy injections. But this still leaves the third question unanswered. What draws the line (equivalent to the laboratory injection of a dye streak) at the right place and time to document the subsequent collapse of the heavy globs? We conclude that the spirals along the East Greenland shelf are not representative of the spirals found elsewhere in the global oceans.

6. Vortex formation

Some of the spiral images (figures 1, 2, 4, 5, 11 and 12) bear a striking resemblance to classical laboratory experiments of instabilities of a shear flow (Brown & Roshko 1974; Winant & Browand 1974). The distinctive streamlines of these flows has been known as the 'cat's-eye' pattern since Kelvin's (1880) celebrated solution. We find it convenient to discuss the vortex formation in terms of the very simple, but fully nonlinear, Stuart (1967) solution (§ 6 *a*). The insight gained and the ease with which properties of the flow can be computed allow us to extend the solution to aspects of the transient problem (§ 6 *b*). Starting from parallel shear flow with an inflection point, figure 19 shows the development of the most unstable mode in a numerical simulation (Corcos & Sherman 1976, 1984). Particles inserted along the interface

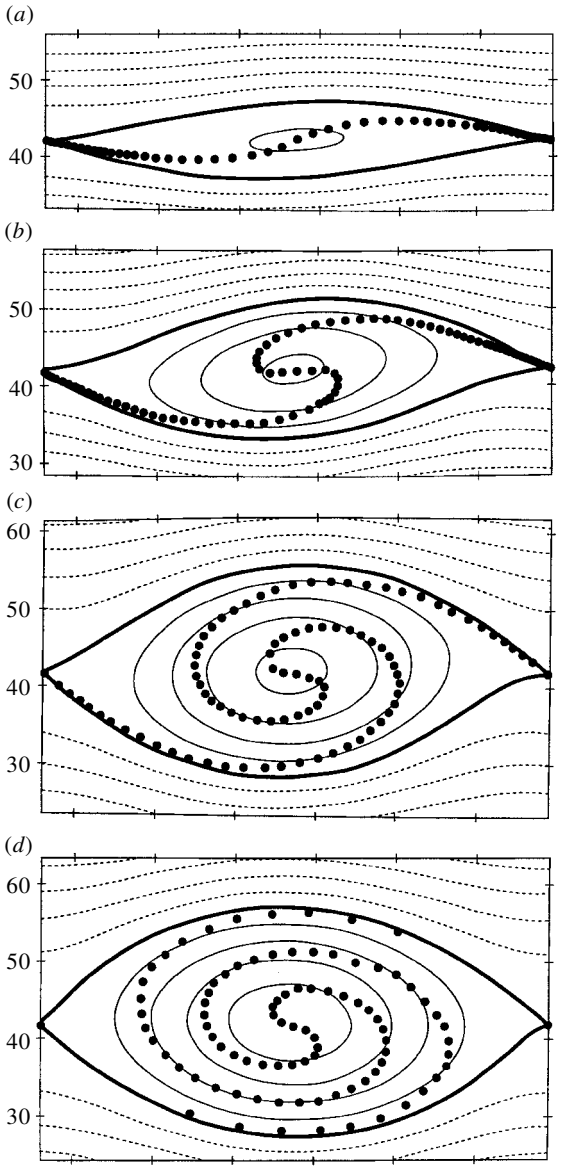

Figure 19. Computer simulations of a developing shear instability (Corcos & Sherman 1984). The four panels show the streamlines at stated times t in $2\pi/(kU)$ units; the heavy line is the 'cat's-eye' streamline through the stagnation points. The dots represent particle positions initially placed on the interface; they are initially crowded near the two stagnation points to allow for a subsequent large strain. The model allows for diffusion and viscosity. We have reversed the original figure from anticyclonic to cyclonic rotation. (a) $t = 0.5$, (b) $t = 1.0$, (c) $t = 1.5$, (d) $t = 2.0$.

(§ 6 c, d) exhibit the growth of a spiral (question A). Allowing for rotation (§ 6 e) and associated instabilities (§ 6 f) leads to breaking of symmetry (B). An attractive feature is that shear instabilities provide a possible link to the visualization problem

(C) in that the developing spiral braids are associated with a unique strain field. A tilting vortex solution (§ 6 *g*) provides for a connection with frontal preconditioning.

(*a*) *The Stuart solution*

Taking first the simplest case of a non-rotating, incompressible equal-density fluid,

$$\frac{\mathrm{D}\boldsymbol{v}}{\mathrm{D}t} = -\rho^{-1}\nabla p, \tag{6.1 a}$$

$$\nabla \cdot \boldsymbol{v} = 0 \tag{6.1 b}$$

can be combined to yield the conservation of vorticity:

$$\frac{\mathrm{D}\zeta}{\mathrm{D}t} = \left(\frac{\partial}{\partial t} + \boldsymbol{v}\cdot\nabla\right)\zeta = 0 \tag{6.2}$$

with

$$\zeta = \frac{\partial v}{\partial x} - \frac{\partial u}{\partial y} = -\nabla^2\psi, \qquad u = \frac{\partial \psi}{\partial y}, \qquad v = -\frac{\partial \psi}{\partial x}, \tag{6.3}$$

where ψ is the stream function.

An *exact steady-state* solution ($\mathrm{D}\zeta/\mathrm{D}t = 0$) by Stuart (1967)

$$\psi(x,y) = -k^{-1}U\log q, \qquad \zeta = +kU(1-\alpha^2)q^{-2}, \tag{6.4}$$

$$q = \cosh ky - \alpha\cos kx \tag{6.5}$$

yields the well-known cat's-eye configuration (figure 20). The stagnation streamlines (the braids) separate the closed interior circulation (the core) from the only slightly perturbed exterior stream lines. α is an arbitrary parameter, $0 \leqslant \alpha \leqslant 1$. For $\alpha = 0$,

$$u(y) = -U\tanh ky, \qquad v = 0, \qquad \zeta = kU/\cosh^2 ky \tag{6.6}$$

going from $u(\pm\infty) = \mp U$ (U is positive). Most of the current shear is between $ky = \pm 1$. As $\alpha \to 1$, we have $q \to 0$, $\zeta \to \infty$ at the core centre, yielding concentrated point vortices.

We shall need some numerical magnitudes. We suggest

$$k = 3\times 10^{-4}\ \mathrm{m}^{-1}, \qquad \zeta_0 = 10^{-4}\ \mathrm{s}^{-1},$$

where $\zeta_0 = kU$ is the vorticity at $y = 0$ for $\alpha = 0$. This implies a distance $2\pi/k \approx 20$ km between stagnation points and a time scale of 10^{-4} rad s^{-1} for winding up the spirals (or about one day per revolution). The initial shear zone of width $2k^{-1} = 7$ km separates the velocity differential of $\pm U = \pm 0.3$ m s^{-1}.

We now convert to dimensionless coordinates, referring distances to k^{-1} and times to ζ_0^{-1}. At the stagnation points $x = \pm\pi$, $y = 0$

$$q = 1+\alpha, \qquad \zeta = (1-\alpha)/(1+\alpha), \tag{6.7}$$

whereas at the core centre $x = 0$, $y = 0$

$$q = 1-\alpha, \qquad \zeta = (1+\alpha)/(1-\alpha). \tag{6.8}$$

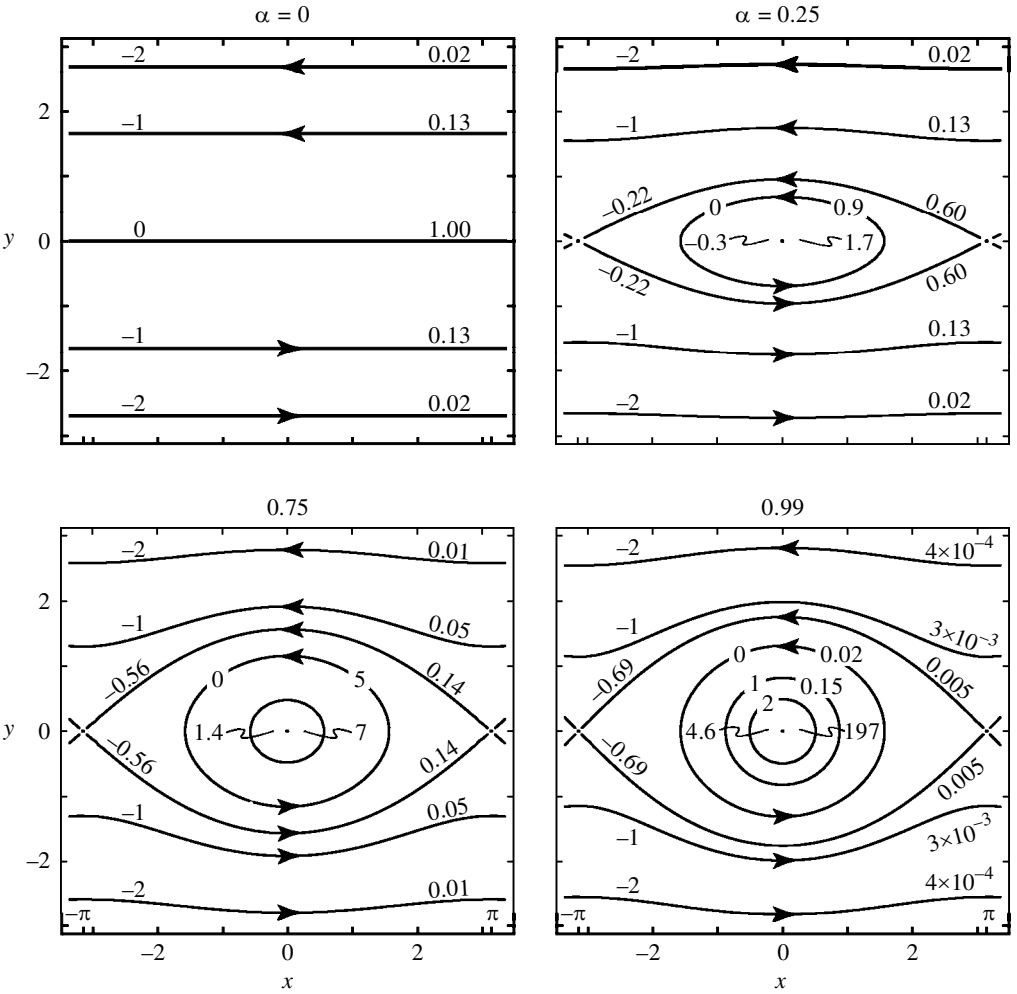

Figure 20. Stuart (1967) solution portraying a steady flow conserving vorticity. Contours designate both dimensionless streamlines $\Psi = \log q$, $q = \cosh y - \alpha \cos x$, and lines of constant vorticity $\zeta = (1-\alpha^2)q^{-2}$, with values indicated to the left and right, respectively, in each panel. For $\alpha = 0$ the velocity profile is given by $u = -\tanh y$. Stagnation points at $x = \pm\pi$, $y = 0$ are connected by 'braids' separating the closed 'core' circulation from the outer flow. With increasing α an increasing fraction of vorticity is concentrated within the core.

The tilt θ of the stream lines at the stagnation points is given by

$$\tan\theta = \pm\sqrt{\alpha} = \sqrt{(\zeta-1)/(\zeta+1)}$$

(Milne-Thomson 1960). The local inclination of the stagnation stream lines (the 'braids') is given by

$$\sin\theta = \sqrt{\frac{\alpha}{1+\alpha}}\sin(\tfrac{1}{2}x). \tag{6.9}$$

The velocity component and the rate of strain along the braid are

$$V_{\text{braid}} = 2\sqrt{\frac{\alpha}{1+\alpha}}\cos(\tfrac{1}{2}x), \tag{6.10}$$

$$\gamma = \sqrt{\frac{\alpha}{1+\alpha}}\sin(\tfrac{1}{2}x)\left[1-\frac{\alpha}{1+\alpha}\sin(\tfrac{1}{2}x)\right]^{1/2}, \tag{6.11}$$

with the principal strain axis directed along the braids.

Certain integral properties follow readily. The integrated vorticity per unit wavelength $2\pi/k$ is given by the circulation

$$\Gamma = 4\pi U/k \tag{6.12}$$

with a fraction

$$\Gamma_{\text{C}}/\Gamma = 4\pi^{-1}\tan^{-1}\sqrt{\alpha} \tag{6.13}$$

within the stagnation streamlines (the core circulation).

The integrated vorticity Γ for the four cases in figure 20 is the same, but we must not regard the panels as successive stages of a developing shear instability. In two-dimensional flow, vorticity can be redistributed but not created, yet the appearance of core vorticity $(1+\alpha)/(1-\alpha)$ exceeds unit vorticity of the initial shear flow. Away from the concentrated cores the flow field depends on the integrated vorticity Γ, not on its distribution or maximum value. With some caution the Stuart formalism can then provide a convenient framework for a discussion of a growing shear instability.

(*b*) *The transient solution*

Corcos & Sherman (1976) have treated the transient problem in the context of the Stuart formalism, remarking that the 'seductive ease' with which properties can be discovered may have subtly influenced their choice (as it has ours) of this model. The result is

$$\frac{H}{\lambda} = \frac{\mu^{-1}C\mathrm{e}^{t/2}}{1+C\mathrm{e}^{t/2}}, \tag{6.14}$$

where H and λ are the height and span of the stagnation streamline. C is determined by comparison with our notation

$$\frac{H}{\lambda} = \frac{\cosh^{-1}(1+2a)}{2\pi} = \frac{\sqrt{\alpha}}{\pi} + O(\alpha^{3/2}). \tag{6.15}$$

Initially, $\alpha = \alpha_0\mathrm{e}^t$ grows at the rate of the basic vorticity scale. The final value ($\alpha = 1$) determines

$$\mu = 2\pi/\cosh^{-1}3 = 3.56.$$

The Stuart transient solution captures the vorticity redistribution process, and yields deformation and velocity fields in the neighbourhood of the braids which agree well with numerical calculations, but it does not yield any details about the spiral structure in the core. The Biot–Savart law (cf. Sherman 1990, p. 29) tells us that the velocity can be obtained from the vorticity field by suitable integration. In the far-field outside the core, this depends only on the integrals of the complex inner vorticity

field, namely the core circulation, which is correctly modelled by the Stuart solution. The $\alpha(t)$ computed according to (6.14), (6.15) does not agree too well with the subsequent numerical simulation by the same authors (figure 19); the growth is somewhat too rapid for $t < 1$ and too slow for $t > 1$.

(c) *Particle configuration*

The motion of a particle is governed by

$$\frac{\mathrm{d}x}{\mathrm{d}t} = -\frac{\partial \log q}{\partial y}, \qquad \frac{\mathrm{d}y}{\mathrm{d}t} = +\frac{\partial \log q}{\partial x}. \tag{6.16}$$

Figure 21 shows the straining of three lines of particles according to the Stuart solution modified by a variable $\alpha(t)$ in accordance with (6.15). The lines introduced along the x-axis at time zero wind into spirals in a few dimensionless time units. The band defined by the particles is stretched and thinned by the deformation field. It can be shown that numerical simulation with fixed α leads to similar results, so that even the (steady) Stuart solution has the deformation field appropriate to forming Lagrangian spiral configurations.

(d) *Kinematics of spiral formation*

The spirals have the distinctive signatures of horizontal shear instability. The evolution proceeds as follows: the initial vorticity is distributed nearly uniformly about an inflection point maximum. In two-dimensional flows, vorticity $\zeta(x, y)$ cannot be amplified, it can only be redistributed and diffused. Vortex cores are formed by clumping vorticity, but the maximum vorticity in the clumps cannot exceed that which was there initially, $\zeta_0 = kU$. In a cut through the developing core, the peak of $\zeta(0, y)$ about $y = 0$ broadens but remains near ζ_0. In a cut through a stagnation point, $\zeta(\pm\pi, y)$ narrows and diminishes. We are describing a redistribution mechanism with an integral constraint that the total circulation $\int\int \zeta(x, y)\,\mathrm{d}x\,\mathrm{d}y$ remains conserved.

The initial shear and associated vorticity field is unstable. Even in the linearized solution, the growing instability includes stagnation points and enclosed streamlines, the Kelvin (1880) 'cat's eyes'. Throughout the redistribution of the initial vorticity, the topology of the cores and stagnation points remains the same, only the distribution of vorticity changes. At the centre of the vortex core, where the vorticity is largest, the fluid is in solid-body rotation near ζ_0. Beyond this, the angular velocity decreases and the spiral lags behind its more rapidly rotating centre.

A rough idea of the size of the core can be had from the Lagrangian spiral, as for example in figure 19, by taking a normal to the line of particles at the centre and estimating the distances along the normal to the next arm of the spiral. By the time $t = 2$, the spiral has rotated 3π rad. The size of the region in near solid-body rotation is roughly half of the core diameter.

The stagnation points have the unique property of being a maximum of induced strain. As the vorticity is advected into the cores, the strain field in the neighbourhood of the stagnation points brings particle lines closer together and elongates them at the same time, conserving area (figure 21). But as the instability grows, the rotation of the particle lines lags behind that of the instantaneous streamlines

(figure 19). Note that the particle line is always within the expanding stagnation streamline. The core appears as a spiral with fluid entrained from both sides of the stagnation streamline.

At the climax state, the size of the cores is about one-fifth of the core spacing. This is well represented in figure 2 with core diameter of *ca.* 2 km and core spacing of *ca.* 10 km. A similar ratio applies to figure 12 (the only case with temporal information). The cores in figures 3, 7, 9 and 11 all have similar diameters. The cores in figures 1 and 4 appear smaller and more concentrated. We believe that these may be well past the climax state and that some diffusion has reduced the size of the solid-body rotation core and hence increased the relative size of the spiral.

(*e*) *Modification by rotation*

There is, of course, no breaking of symmetry in any of the solutions to (6.1). The obvious step is to add the Coriolis acceleration by replacing (6.1 *a*) with

$$\frac{\mathrm{D}\boldsymbol{v}}{\mathrm{D}t} + \boldsymbol{f} \times \boldsymbol{v} = -\rho^{-1}\nabla p. \tag{6.17}$$

The conservation of vorticity (6.2) now becomes $\mathrm{D}(f+\zeta)/\mathrm{D}t = 0$; for solutions in the f-plane there is no change in the streamlines or the distribution of vorticity. But there is a change in the pressure distribution.† It can be verified that

$$\frac{p}{\rho U^2} = -\frac{\cosh ky + \alpha \cos kx}{2q} + \frac{1}{Ro}\log q, \qquad Ro = \frac{\zeta_0}{f} \tag{6.18}$$

is a solution to (6.17). The first term alone gives the pressure distribution for either cyclonic or anticyclonic cat's-eyes in the case of no rotation ($f = 0$) (top panels in figure 22). The bottom panels represent the oceanographically familiar situation of near-geostrophic balance in which isobars and streamlines are coincident. p is constant for $\alpha = 0$; with increasing α there is a deepening trough at the core centre. The pressure field balances the particle acceleration into and out of the stagnation points, and the centrifugal acceleration of the circulation around the core. Note the transition with increasing f from an inertially balanced central low to a geostrophically balanced high for the anticyclonic case (right panels going down). This corresponds to the transition at the inertial frequency ($Ro = -1$) of an anticyclonic circular vortex. There is no such transition for the cyclonic case, a low remains a low: this fundamental distinction is associated (as we shall see) with the difference in the stability of cyclonic and anticyclonic circulation. Friction has been ignored; the associated ageostrophic flow down the pressure gradient will intensify the cyclonic low, aiding the development of the spiral. In the anticyclonic case the down pressure flow is outward and will tend to dissipate the high.

We have here applied a two-dimensional model to the upper ocean mixed layer bounded by a pycnocline below. For a variable pycnocline the motion cannot be horizontal, as assumed, unless the streamlines are also lines of constant pressure (i.e. constant pycnocline depth). This is because vertical vortex lines will be stretched by the pycnocline displacement as they follow the streamlines. For near-geostrophic

† This is consistent with the criterion established by Hide (1977, 1997): a two-dimensional velocity field that is a solution without rotation is also a solution in a rotating system, but the pressure gradient field is modified by rotation.

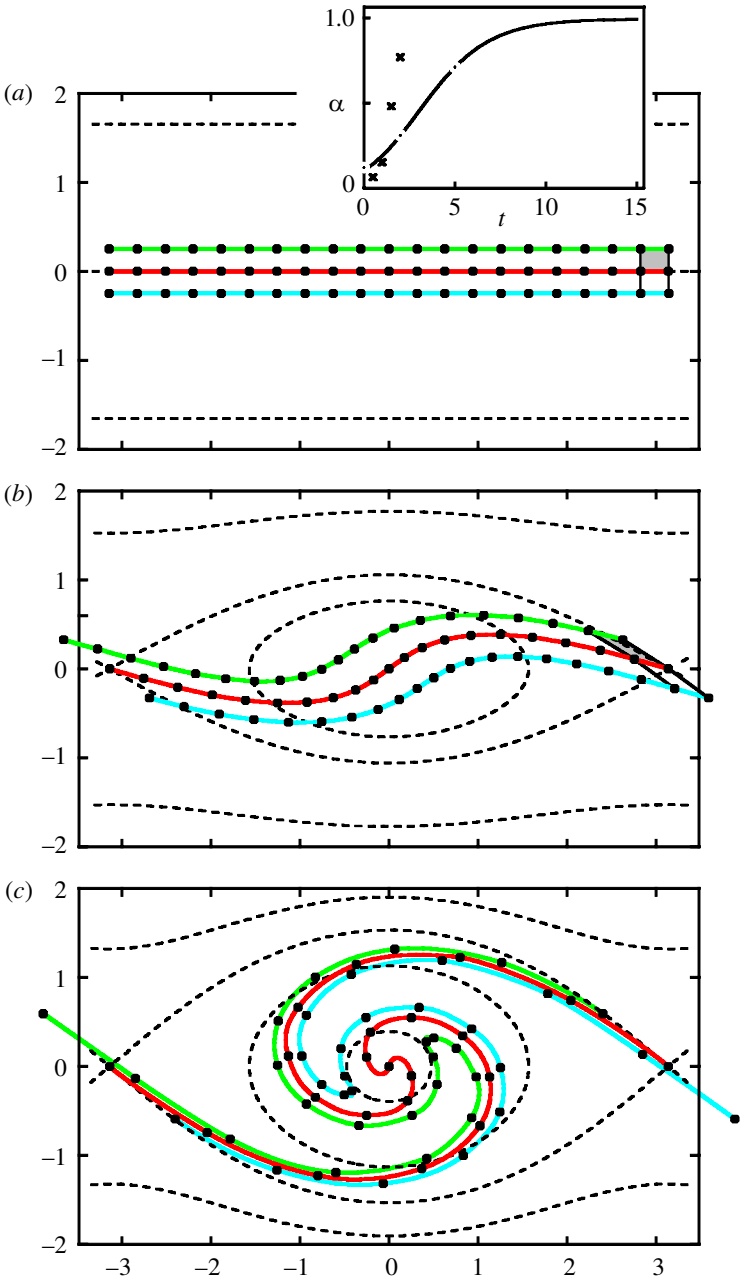

Figure 21. Particle distribution in a Stuart vortex. Particles are initially placed between stagnation points $x = \pm\pi$ along the three lines $y = 0, \pm 0.25$. Subsequent positions are computed for $\alpha(t)$ determined by the incipient stability calculations of Corcos & Sherman (1976). Particles are concentrated along the widening braids and injected into the core. The deformation of a rectangle formed by four particles (including the fixed stagnation point) is shown. (*a*) $t = 0$, $\alpha = 0.12$; (*b*) $t = 2$, $\alpha = 0.31$; (*c*) $t = 5$, $\alpha = 0.71$.

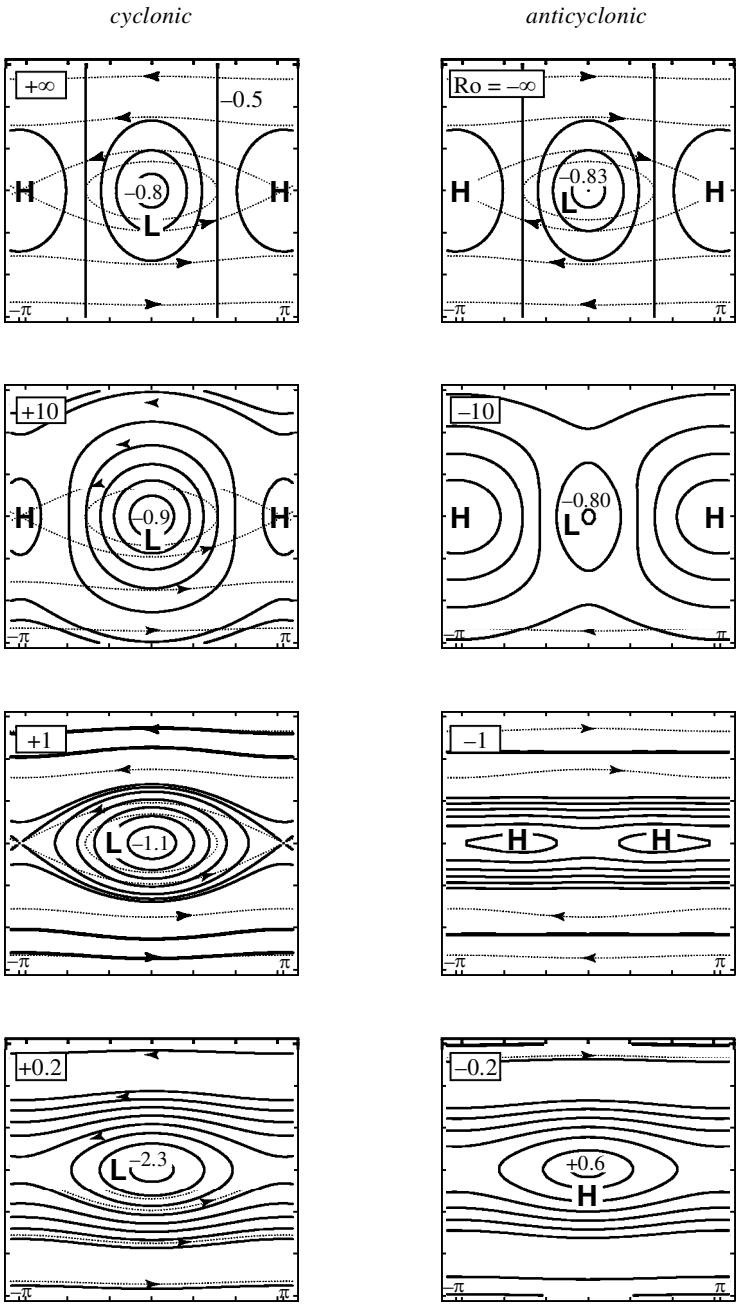

Figure 22. The pressure field associated with the Stuart solution for $\alpha = 0.25$, modified with rotation for (left) cyclonic and (right) anticyclonic conditions. Rossby numbers $Ro = \zeta/f$ are indicated in left top corners. Dimensionless pressures $p/(\rho U^2)$ at the vortex centre are shown. Bottom panels correspond to a near-geostrophic balance typical for large-scale ocean conditions and top panels correspond to non-rotating laboratory experiments. The transition takes place at Rossby numbers of the order of 1. H, high; L, low.

flow (the two bottom panels of figure 22) the pressure and streamline fields do in fact nearly coincide. In all events, for typical pycnocline strengths the depth changes associated with the pressure perturbations are quite small. This is reflected in the small internal Froude number F^2 of these flows. With $\Delta u = \frac{1}{4}\,\mathrm{m\,s^{-1}}$, $\Delta\rho/\rho = 2 \times 10^{-3}$, $h = 100$ m, we have $F^2 = 0.03$.

(*f*) *Rayleigh instability*

There is ample numerical and experimental evidence for instabilities that impede the development of anticyclonic vortices but have no such effect on cyclonic vortices. Extensive numerical experiments with vertical columnar vortices by Potylitsin & Peltier (1998) demonstrate that 'the dominant instability mechanism which drives the (selective) destruction of anticyclonic vortices ... may be understood to constitute a three-dimensional inertial (centrifugal) instability.' Similar conclusions are reached by Métais *et al*. (1995) and Orlandi & Carnevale (1999). Lesieur *et al*. (1991) refer to very regular cyclonic vortices and the 'catastrophic disruption' in anticyclonic flow.

The distinction is equally clear in laboratory experiments, so much so that Bidokhti & Tritton (1992) use the terms *stabilizing* and *destabilizing* as synonymous with *cyclonic* and moderately *anticyclonic*. Kloosterziel (1990) observed experimentally that 'it is virtually impossible to create anticyclonic vortices in the rotating tank if one attempts to do so by simply stirring the fluid locally. But cyclonic vortices are easily created in this way! In the anticyclonic case stirring ... leads to turbulent motion and the generation of waves whereas by cyclonic stirring a well-defined smooth vortex forms.' The flow past a circular cylinder in a rotating water channel shows distinctly different behaviour between the eddies on the two sides (Boyer & Davies 1982). As the free-stream speed is increased to values for which separation begins to take place, the cyclonic eddy dominates. The authors refer to a cloud photograph of vortices in the lee of Guadaloupe Island taken from Skylab which 'shows strong cyclonic vortices with relatively weak or non-existing anticyclonic motions.' Figure 10 shows a similar oceanic situation in the lee of Isla Santa Catalina in the Gulf of California. Afanasyev & Peltier (1998) demonstrate the robustness of the centrifugal instability criterion in a series of laboratory experiments. The conclusions are not substantially modified by background stratification or departures from the circular geometry. We are encouraged to apply this criterion to the Stuart cat's-eye configuration.

The Rayleigh criterion (Drazin & Reid 1981; Sherman 1990) for the instability of a circular vortex is

$$\frac{\mathrm{d}}{\mathrm{d}r}[rv(r)]^2 < 0, \tag{6.19}$$

where v refers to the azimuthal velocity in non-rotating coordinates. Under condition (6.19) the interchange of two neighbouring rotating annuli, each conserving angular momentum, leads to a *decrease* in total energy, thus indicating instability. Combining (6.19) with the vertical component of vorticity

$$\zeta = \frac{1}{r}\frac{\mathrm{d}}{\mathrm{d}r}(rv) \tag{6.20}$$

yields the Rayleigh† instability criterion $v\zeta < 0$.

† This is not related to the usual Rayleigh number which defines the onset of thermal convection.

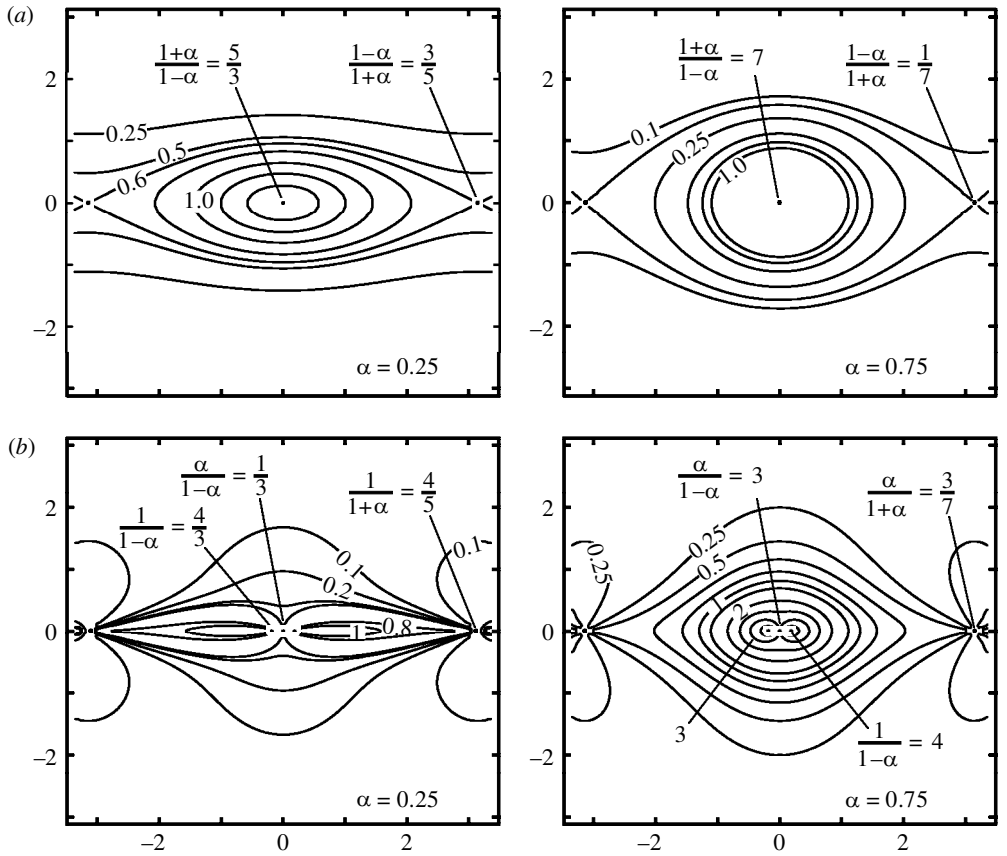

Figure 23. Contour plots of the absolute values of (*a*) the dimensionless vorticity $|\zeta|/\zeta_0$ and (*b*) the dimensionless centrifugal parameter $|V|/(\mathcal{R}\zeta_0)$ for the Stuart cat's-eye solution. The cyclonic case is always stable. For the anticyclonic case centrifugal instability dominates over inertial instability.

To extend the criterion to the case of background rotation, replace rv in (6.19) by $rv + \frac{1}{2}r^2 f$, where $\frac{1}{2}r^2 f$ is the planetary circulation. The result is

$$Ra = \left[1 + \frac{\zeta}{f}\right]\left[1 + \frac{2V/r}{f}\right] < 0, \tag{6.21}$$

where $V = \pm\sqrt{u^2 + v^2}$ is the local velocity for cyclonic/anticyclonic flow. As $r \to \infty$, (6.21) reduces to the 'inertial instability' criterion,

$$Ro = \zeta/f < -1, \tag{6.22}$$

which goes back to Pedley (1969) and to Tritton's (1992) 'displaced-particle' approach.†

To apply the Rayleigh instability criterion to the Stuart cat's-eye solution, we replace r in (6.21) by the local radius of curvature $\mathcal{R}$ (figure 23). The cyclonic case is

† Oceanographers are familiar with the vertical shear instability for $\mathrm{d}u/\mathrm{d}z > 2N$ but surprisingly unfamiliar with the inertial instability for $-\zeta = \mathrm{d}u/\mathrm{d}y > f$ in anticyclonic horizontal shear.

always stable. For the anticyclonic case (ζ and V negative) instability occurs when one of the two brackets in (6.23) becomes negative. It can be shown that the earliest instability (smallest α) occurs along the x-axis near the core, where

$$Ra = \left[1 - \left(\frac{1+\alpha}{1-\alpha}\right)\frac{\zeta_0}{f}\right]\left[1 - \left(\frac{2}{1-\alpha}\right)\frac{\zeta_0}{f}\right],$$

so that with increasing α the right bracket will go negative first. The conclusion is that the development of anticyclonic cat's-eyes may be limited by centrifugal instability.

(g) *Modification by tilt*

The Stuart solution may be further modified to apply to a tilting y-axis, as pertains to the frontal solutions in the next sections. Consider a frontal surface sloping upwards in the positive y-direction along $z = y\tan\iota$, and write $y' = y - z\cot\iota$ for the distance from the tilting front at depth z. Replace the previous solution (6.4) for the stream function $\psi(x, y)$ and (6.18) for the pressure $p(x, y)$ by $\psi(x, y')$ and $p(x, y')$, giving the departure $p(x, y') = \rho U^2\tilde{p}(x, y')$ from the hydrostatic pressure $p_0(z) = \int_z^0 g\rho_0(z)\,\mathrm{d}z$, with horizontal pressure gradients exactly balancing the field accelerations. We now inquire whether there is a density field $\rho(x, y, z) = \rho_0(z) + \Delta\rho(x, y'(x, z))$ that can balance the total pressure field $p_0(z) + p(x, y'(x, z))$. The hydrostatic condition

$$g\Delta\rho(x, y') = -\frac{\partial p(x, y')}{\partial z} = -\frac{\partial p}{\partial y'}\frac{\partial y'}{\partial z} = \frac{1}{\tan\iota}\frac{\partial p}{\partial y'}$$

yields

$$\Delta\rho(x, y') = \rho_0\frac{kU^2}{g\tan\iota}\frac{\sinh y'}{q^2(x, y')}\left(\alpha\cos x + \frac{1}{Ro}q(x, y')\right). \tag{6.23}$$

We have thus arrived at a cat's-eye solution in the presence of rotation and tilt which provides for a gentle transition from the geostrophically balanced tilting frontal solutions to be developed in the following sections.

(h) *Summary*

The Kelvin–Helmholtz cat's-eye pattern has the ingredients required to respond to the three questions posed in the introduction:

(A) a rotational core that winds particles into spirals,

(B) breaking of symmetry in favour of the stable cyclonic rotation, and

(C) a unique deformation field which one expects to become visible in the sunglitter.

We require a preconditioning phase in which the ambient shear is amplified to permit a ready initiation of the spiraling process. For that purpose we examine existing models of ocean fronts.

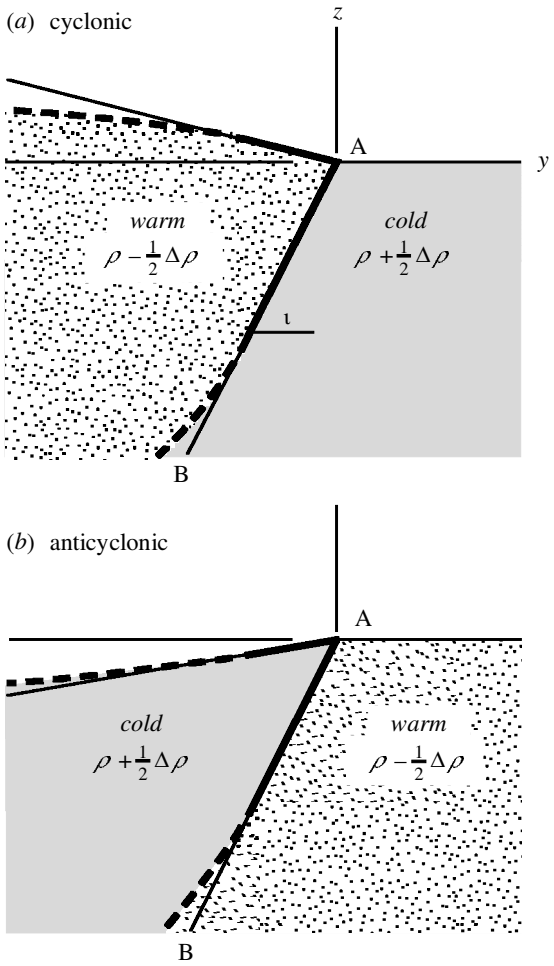

Figure 24. A sharp front, with boundary AB along $z = y \tan \iota$, $y < 0$. The y-axis (northward) across the front is in the up-slope direction, with $y = 0$ representing the frontal outcrop (the association with geographic directions is for ease of discussion only). (*a*) The front separates a wedge of warm water to the south (left) from cold underlying water to the north, with $\rho_c = \rho_w + \Delta\rho$. In order for the horizontal pressure gradient to vanish at depth (as assumed), the surface must rise south of A, associated with geostrophic eastward currents (out of the paper) and concentrated cyclonic shear at the frontal boundary. For large negative y, the frontal inclination ι, surface slope and geostrophic current all diminish (as indicated by the dashed curves). (*b*) For a cold wedge the frontal shear is anticyclonic, but this situation is associated with a statically unstable stratification of cold water above warm water.

7. The Margules front

(*a*) *A sharp front*

The basics go back to the Austrian and Bergen schools of meteorology in the early 20th century (Margules 1904; Bjerknes *et al.* 1933). Essential considerations are summarized in figure 24. If variations in the x-direction (along the front) are negligible,

then in a steady state the pressure varies along the front according to

$$\delta p = \frac{\partial p}{\partial y}\,\mathrm{d}y + \frac{\partial p}{\partial z}\,\mathrm{d}z. \tag{7.1}$$

The pressures at the cold and warm sides of the frontal boundary must equal,

$$\Delta p = p_{\mathrm{c}} - p_{\mathrm{w}} = 0. \tag{7.2}$$

Hence in (7.1) with $\delta(\Delta p) = 0$, the frontal inclination ι is given by

$$\tan\iota = \left(\frac{\mathrm{d}z}{\mathrm{d}y}\right)_{\mathrm{front}} = \frac{(\partial p/\partial y)_{\mathrm{c}} - (\partial p/\partial y)_{\mathrm{w}}}{g(\rho_{\mathrm{c}} - \rho_{\mathrm{w}})} \tag{7.3}$$

for the hydrostatic condition $\partial p/\partial z = -\rho g$. We assume that the along-the-front component of current is in geostrophic balance,

$$u = -\frac{1}{f\rho}\frac{\partial p}{\partial y}. \tag{7.4}$$

From (7.3)

$$\tan\iota = f\frac{\rho_{\mathrm{w}}u_{\mathrm{w}} - \rho_{\mathrm{c}}u_{\mathrm{c}}}{g(\rho_{\mathrm{c}} - \rho_{\mathrm{w}})} \approx \frac{-f\Delta u}{g\Delta\rho/\rho}, \tag{7.5}$$

where Δ denotes cold minus warm. This is essentially a statement of the thermal-wind balance, and is known as 'Margules's law' when written in terms of temperature. The classical Margules (1904) front is the traditional starting point for a discussion of frontal effects, but there are shortcomings. Ocean fronts do not extend to great depth; this can be accommodated by a decrease with depth of the frontal inclination ι, and the associated decrease of surface inclination and geostrophic flow (figure 24). For the cyclonic case, this leads to a weak anticyclonic circulation to the south of the front.

For a warm-water wedge (figure 24*a*) the frontal shear is cyclonic; for a cold-water wedge (figure 24*b*) it is anticyclonic. The latter case is excluded by the independent condition that heavy fluid above light fluid is statically unstable (Bluestein 1993). The general statement that 'all fronts are cyclonic' is based on this consideration. It is tempting to offer this argument as an 'explanation' of the dominance of cyclonic spirals. But, as shown next, the anticyclonic front is statically stable for a sufficiently gradual density transition.

(*b*) *A softened front*

We consider the front as a limiting case of a finite transition (frontal surfaces of zero and first order in the notation of Palmén & Newton (1969)). Under these circumstances anticyclonic frontal zones are shown to be statically stable provided that their width Δy exceeds some critical value. In contrast, the cyclonic fronts are stable for all Δy.

The frontal zone is centred along

$$z_{\mathrm{F}} = y\tan\iota \tag{7.6}$$

for $y < 0$. The transition of the density field across the frontal zone is represented by

$$\left.\begin{aligned} \rho(y,z) = \rho_0(z) \mp \tfrac{1}{2}\Delta\rho \tanh\chi, \qquad \chi(y,z) = \frac{z - z_{\mathrm{F}}(y)}{\Delta z} = \tilde{z} - \tilde{y}, \\ \tilde{z} = \frac{z}{\Delta z}, \qquad \tilde{y} = \frac{y}{\Delta y}, \qquad \tan\iota = \frac{\Delta z}{\Delta y} \end{aligned}\right\} \tag{7.7}$$

for the cyclonic/anticyclonic case, respectively, with $\Delta\rho = \rho_{\mathrm{cold}} - \rho_{\mathrm{warm}}$. The Brunt–Väisälä (buoyancy) frequency $N = \sqrt{g\rho^{-1}(-\partial\rho/\partial z)}$ is then given by

$$N^2(y,z) = N_\infty^2(z) \pm \Delta N^2 \operatorname{sech}^2(\chi), \qquad \Delta N^2 = \tfrac{1}{2}g(\Delta\rho/\rho)\Delta z^{-1}, \tag{7.8}$$

where $N_\infty^2(z) = g\rho^{-1}(-\partial\rho_0/\partial z)$ refers to the underlying stratification on either side far away from the front, $\chi \to \pm\infty$. We take $N_\infty = 25f = 2.5 \times 10^{-3}\,\mathrm{s}^{-1}$ as representative of a mixed layer; relative to this value, the frontal stratification $N_0^2 = N_\infty^2 \pm \Delta N^2$ is enhanced for the cyclonic case and diminished for the anticyclonic case, with important stability implications. For numerical values $\tan\iota = +0.02$, $\Delta\rho/\rho = 10^{-4}$, the thermal wind equation (7.5) yields $\Delta u = 0.2\,\mathrm{m\,s}^{-1}$.

The pressure at depth $z = -H$ is given by

$$p(y,H) = g\int_{-H}^{0} \rho_0(z)\,\mathrm{d}z + \rho_0 g\eta \pm \tfrac{1}{2}\Delta\rho g\,\Delta z\,P(y,H), \tag{7.9}$$

where $\eta(y)$ is a surface displacement (as yet unspecified) of density ρ_0 , and

$$P(\tilde{y},\tilde{H}) = \mu(\tilde{H} + \tilde{y}) - \mu(\tilde{y}), \qquad \mu(\chi) = \int \tanh\chi\,\mathrm{d}\chi = \log\cosh\chi. \tag{7.10}$$

For large $|\chi|$, $\mu(\chi) = |\chi| - \log 2$. Thus well beneath the front, $\tilde{H} + \tilde{y} \gg 1$, $\tilde{y} < 0$.

$$P(\tilde{y},\tilde{H}) = \tilde{H} + \tilde{y} - \log 2 - \mu(\tilde{y}). \tag{7.11}$$

By setting

$$\eta(y) = \pm\tfrac{1}{2}(\Delta\rho/\rho)\Delta z[\mu(\tilde{y}) + \log 2 - \tilde{y}] \tag{7.12}$$

all horizontal pressure gradients vanish well beneath the front. $\eta(y)$ varies from 0 at large positive y to

$$\eta(y) = \mp(\Delta\rho/\rho)\Delta z\,\tilde{y} = \mp(\Delta\rho/\rho)z_{\mathrm{F}}(y) \tag{7.13}$$

for large negative y. Going back to (7.9), the general expression for the pressure at any depth (negative z) is given by

$$p(y,z) = g\int_{z}^{0} \rho_0(z')\,\mathrm{d}z' \pm \tfrac{1}{2}\Delta\rho g\,\Delta z[\log 2\cosh(\tilde{z} - \tilde{y}) - \tilde{y}]. \tag{7.14}$$

The associated geostrophic velocity is

$$u(y,z) = -\frac{1}{f\rho}\frac{\partial p}{\partial y} = \pm\tfrac{1}{2}\Delta u[1 + \tanh(\tilde{z} - \tilde{y})], \qquad \Delta u = \frac{g\tan\iota\,\Delta\rho/\rho}{f}. \tag{7.15}$$

It can be verified that $f\partial u/\partial z = +(g/\rho)\partial\rho/\partial y$ in accordance with the thermal wind relation. Figure 25 shows independent realizations for three frontal widths Δy; the right panels ($\Delta y = 1$ km) come close to the previous figures for a sharp front.

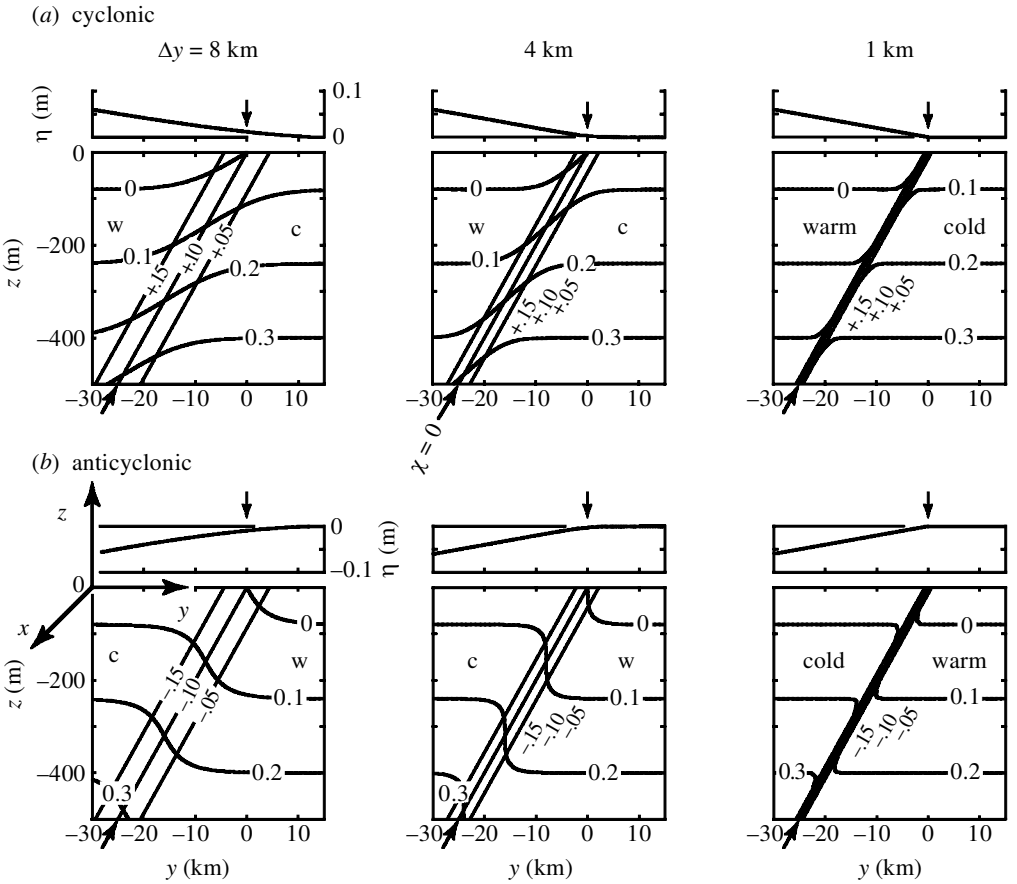

Figure 25. 'Soft' fronts, with the fields of density and velocity for three configurations. Frontal sharpness increases from left to right. (The far right panels resemble the sharp fronts in the previous figure.) Frontal inclination is fixed at $\tan\iota = 0.02$. Isodensity contours are from 1000.0 to 1000.3 kg m^{-3}. Velocities in m s^{-1} (positive eastward, out of the paper), with cyclonic frontal shear for the upper three panels, and westward with anticyclonic shear in the lower three panels. The anticyclonic front is statically unstable for $\Delta y < 4$ km. The middle contour of the three isovelocity contours is at the frontal centre; the difference between the outer contours is fixed at 0.1 m s^{-1}. The associated surface displacement $\eta(y)$ is displayed above the panels. Numerical values are $\Delta\rho/\rho_0 = 10^{-4}$, $N_\infty = 25f = 2.5 \times 10^{-3}$ s^{-1}.

Instabilities

Static instability for the anticyclonic case (figure 25*b*) sets in for $\Delta y = 4$ km or smaller. It will next be shown that vertical shear instability is even more limiting. It is convenient to introduce the dimensionless parameter

$$\nu = \frac{\tan\iota\, N_\infty}{f} = \frac{N_\infty \Delta u}{g\Delta\rho/\rho} \tag{7.16}$$

as a measure of the relative contribution of the velocity change Δu and the density change $\Delta\rho$ across the front. We need a dimensionless measure for the frontal perturbation in the stratification. In recognition of the early work by Hesselberg (1918),

Väisälä (1925) and Brunt (1927), we introduce the equivalent notations

$$He = \frac{N^2 - N_\infty^2}{N_\infty^2} = \frac{V\ddot{a}^2}{V\ddot{a}_\infty^2} - 1, \qquad V\ddot{a}^2 = \frac{N^2}{f^2}, \tag{7.17}$$

where N is the Brunt–Väsälä frequency. We now consider the instabilities at the frontal centre $\chi = 0$, where the gradients are concentrated. It follows from (7.7), (7.8), (7.15), (7.16), (7.17) that

$$\left.\begin{aligned} Ro = -\frac{\partial u/\partial y}{f} &= \nu^2 He, \\ Ri^{-1/2} = \frac{\partial u/\partial z}{N} &= \frac{\nu He}{\sqrt{1+He}}, \\ \Delta y = \frac{W}{\nu|He|}, \qquad W &= \frac{1}{2}\frac{g}{f^2}\frac{\Delta\rho}{\rho}\frac{f}{N_\infty}. \end{aligned}\right\} \tag{7.18}$$

In our special model He, Ro, Ri, u, $\partial\rho/\partial z$ (but not ρ) are all constant along frontal surfaces χ, and diminish with distance from the frontal centre. For a fixed Ri, (7.18) gives a quadratic in He yielding

$$Ro^{\pm} = \nu^2 He = \tfrac{1}{2} Ri^{-1}(1 \pm \sqrt{1 + 4\nu^2 Ri}).$$

Thus

$$Ro^{+} = +Ri^{-1} + \nu^2 + \cdots, \qquad Ro^{-} = -\nu^2 + \tfrac{1}{4} Ri\, \nu^4 + \cdots, \qquad \nu \ll 1, \tag{7.19}$$

for the cyclonic/anticyclonic fronts, respectively. The Rossby numbers associated with critical vertical shear† $Ri = \frac{1}{4}$ are $Ro^{\pm} = +4 + \nu^2$, $-\nu^2 + \nu^4/16$, and so the development of anticyclonic horizontal shear is severely impeded relative to cyclonic horizontal shear.

Static instability ($N = 0$) is associated with $He = -1$ and $Ro_{\text{static}} = -\nu^2$. There is no static instability for the cyclonic case; for the anticyclonic case shear is always more limiting than static instability. For the case shown in figure 25, shear instability sets in at $\Delta y = 4.2$ km, compared with 4 km for the static instability. For the cyclonic case $\Delta y_{\text{shear}} = \frac{1}{4} W\nu$ yields $\frac{1}{4}$ km, and all three upper panels are stable.

Potential vorticity

Figure 25 can be regarded as giving independent realizations of fronts of various degrees of sharpness. For simplicity we have taken constant frontal inclinations, $\tan\iota = 0.02$. We now need to consider the potential vorticity

$$\rho q = (\boldsymbol{f} + \boldsymbol{\zeta}) \cdot \nabla\rho = \left(f - \frac{\partial u}{\partial y}\right)\frac{\partial \rho}{\partial z} + \frac{\partial u}{\partial z}\frac{\partial \rho}{\partial y} + \cdots. \tag{7.20}$$

The second term (tilting potential) is of first order in any thermal wind model. The thermal wind equation

$$\frac{\partial \rho}{\partial y} = f\rho g^{-1}\frac{\partial u}{\partial z}$$

† We use the necessary condition $Ri = \frac{1}{4}$ throughout the paper.

then yields a dimensionless vorticity (Rudnick & Luyten 1996)

$$Q \equiv \frac{gq}{fN_\infty^2} = \frac{N^2}{N_\infty^2}(-1 - Ro + Ri^{-1}) \tag{7.21}$$

for the three terms on the right-hand side in (7.20). For our model, this reduces to a very simple relation:

$$-Q = (1 + He)\left(1 + \nu^2 He - \frac{\nu^2 He^2}{1 + He}\right) = 1 + Ro + He. \tag{7.22}$$

Consider the frontal 'sharpness' $W/\Delta y \sim |\nu He| = \sqrt{|Ro\, He|}$ at constant $-Q = 1 + Ro + He$. For a maximum product $Ro\, He$, subject to a constant sum $Ro + He$, we have

$$Ro = He = \tfrac{1}{2}(-Q - 1), \qquad W/\Delta y_{\min} = \tfrac{1}{2}(-Q - 1). \tag{7.23}$$

But $Ro = \nu^2 He$, and so

$$\nu = 1, \qquad \tan \iota = \nu\left(\frac{f}{N_\infty}\right) = \frac{f}{N_\infty} \tag{7.24}$$

at maximum frontal sharpness. To interpret the existence of a minimum value for Δy, consider that $\Delta y \to \infty$ as $\nu \to 0$ because the layer approaches the horizontal, and again $\Delta y \to \infty$ as $\nu \to \infty$ because the horizontal density gradient across the front vanishes. A minimum is reached for $\nu = 1$. The conclusion is that in an ensemble of frontal models with the same potential vorticity and obeying the thermal wind condition, those models for which $Ro = He$ have a minimum in frontal width and a frontal inclination f/N_∞.

Figure 25 was drawn for a fixed inclination $\tan \iota$. One wishes to examine frontal formation for which potential vorticity is conserved. Figure 26 shows independent realizations of $\rho(y, z)$ and $u(y, z)$ fields for the case of fixed vorticities $Q = -2.25$ (cyclonic), -0.25 (anticyclonic). The frontal width Δy decreases, and the absolute Rossby number $|Ro|$ increases from left to right. The right-hand panels represent maximum frontal sharpness (minimum Δy). The slanting lines show the velocity field along the frontal surface, which steepens with increasing frontal sharpness. The velocity *difference* across the three lines is held at a constant $0.1\ \mathrm{m\ s^{-1}}$. The frontal shear and isopycnal slopes $\partial\rho/\partial y$ both increase from left to right. But $\partial\rho/\partial z$, and hence N, decreases for the cyclonic case, and increases for the anticyclonic case: the enhancement of horizontal cyclonic (anticyclonic) shear is associated with the relaxation of an overstratified (understratified) region toward the unperturbed stratification N_∞. This follows from the definition (7.20) for potential vorticity: an increase in positive ζ is associated with a decrease in N; for the anticyclonic case an increase in negative ζ and resulting decrease in $f + \zeta$ is associated with an increase in N. An important point is that the sequence of panels constitutes realizations at a constant potential vorticity and might suggest a time history of frontal formation.

Figure 27 is an attempt to pull together in stratification, vorticity-space these diverse considerations. Lines of constant Q, ν, and Ri are plotted. Shadings indicate areas of vertical shear instability $Ri < \frac{1}{4}$, static instability $He < -1$ (or equivalently $V\ddot{a} < 0$) and inertial instability $Ro < -1$. Positive Ro designates cyclonic frontal

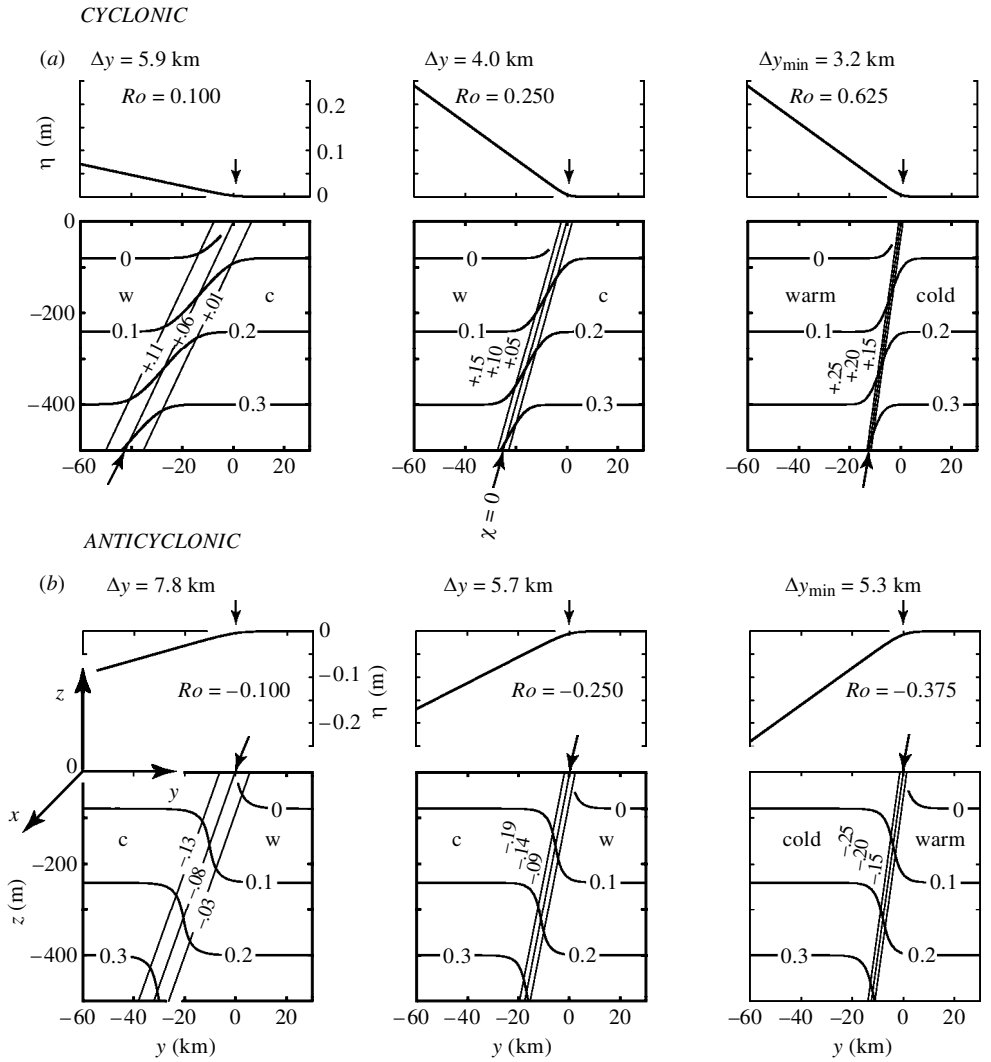

Figure 26. The fields of density and velocity for three frontal configurations at fixed potential vorticities $Q = -2.25$ (cyclonic (a)) and $Q = -0.25$ (anticyclonic (b)). The frontal inclination and the frontal shear increase with increasing frontal sharpness. Parameters are the same as in previous figure.

shear, negative Ro designates anticyclonic frontal shear. The line $\nu = 1$ corresponds to minimum Δy and maximum $|Ro|$.

The anticyclonic space is mined with instabilities. The only available space is the white area in the bottom left quarter. For $Q = 0$ the largest negative Rossby number is $-\frac{1}{2}$, and the extreme value (the intersection of $\nu = 1$ with $Ri = \frac{1}{4}$) is $-2(\sqrt{2} - 1) = -0.82$. For the cyclonic case Ro attains a maximum value $Ro = 5$ where $\nu = 1$ intersects $Ri = Ri_c = \frac{1}{4}$ (red dot). Evidently the model excludes frontal shears with large negative Rossby numbers, but permits the large positive Rossby numbers associated with cyclonic fronts.

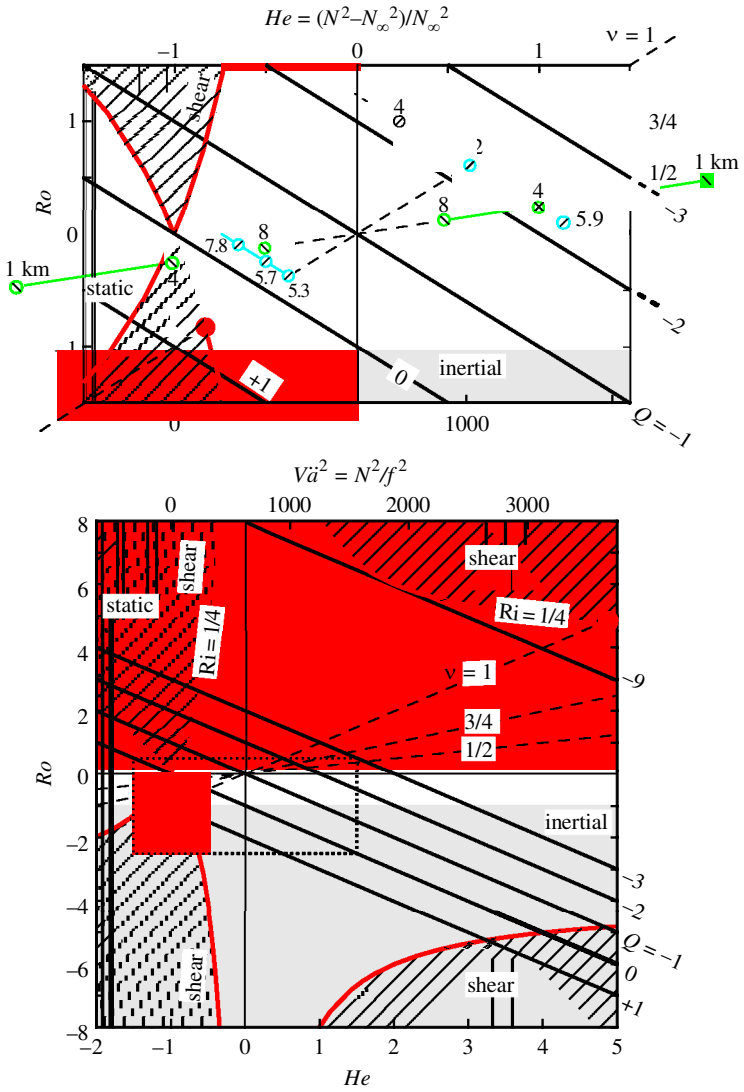

Figure 27. Frontal stability in $V\ddot{a}^2, Ro$-space, or equivalently in He, Ro-space (upper panel shows dotted box on an enlarged scale). Positive Ro designates cyclonic frontal shear, negative Ro designates anticyclonic frontal shear. Inertial instability occurs for $Ro < -1$. Static instability occurs for $V\ddot{a} < 0$ (or equivalently $He < -1$). Vertical shear instability is associated with $Ri < Ri_c = 1/4$ (red lines). Slanting solid lines designate equal potential vorticity Q in units N_∞^2/f^2, where N_∞ is the stratification far away to both sides of the front. $\nu = \tan\iota\, N_\infty/f$ is a measure of frontal inclination ι. Green lines connect points associated with figure 25, blue lines with figure 26, with Δy (in km) indicated.

8. The Hoskins–Bretherton front

The foregoing model deals with realizations of frontal configurations subject to the conservation of potential vorticity along the frontal surface. It does not deal explicitly with the time history of the frontal formation. Nor does it take explicit account of the

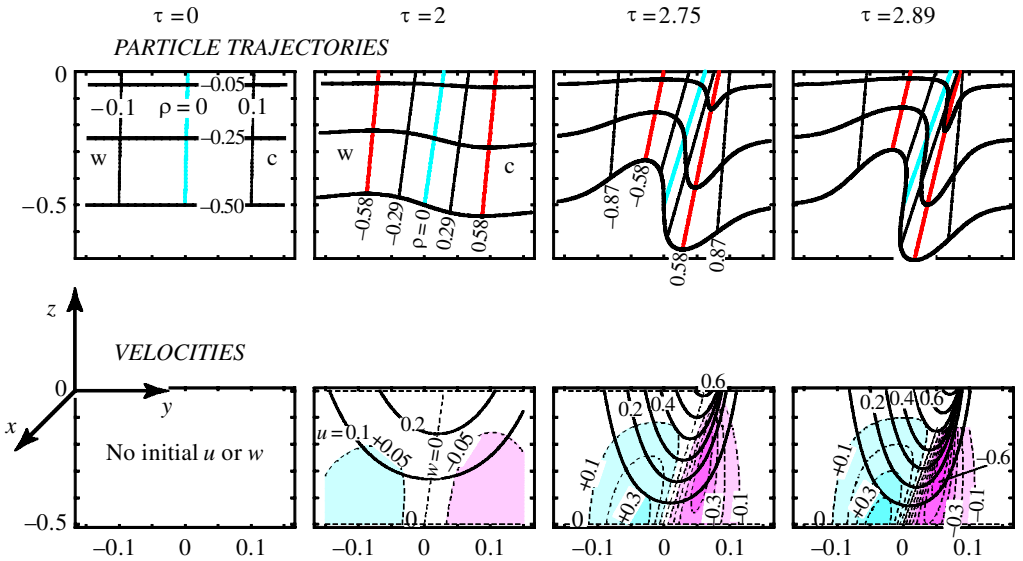

Figure 28. Cross-frontal vertical sections (y northward in 50 km units, z upward in 200 m units) with indicated times τ (approximately days). A uniform strain rate $\gamma = -0.1f$ on an initial northward density increase in a vertically mixed layer generates an eastward frontal jet. (Top) Black lines mark particles initially near the surface (10 m depth), in the middle (50 m) and at the bottom of the 100 m mixed layer. Slanting lines (initially vertical) are isopycnals (kg m^{-3}) with blue line at the centre of the density transition. The 'frontal isopycnals' $\rho_F = \pm\sqrt{1/3} = \pm 0.58$ define the centres of the developing cyclonic/anticyclonic shears. (Bottom) Eastward velocities u (in 0.5 m s^{-1} units) and vertical velocities w (blue is upward, red is downward, in 0.2 cm s^{-1} units). The front sharpens and tilts forward to the north, developing a cyclonic north wall with density and velocity discontinuities at the surface, and a relatively weak anticyclonic south flank. The mixed layer deepens under the north wall and shoals under the south flank.

condition that density and potential vorticity needs to be conserved for individual particles:

$$\frac{\mathrm{D}\rho}{\mathrm{D}t} = 0, \qquad \frac{\mathrm{D}q}{\mathrm{D}t} = 0. \tag{8.1}$$

This problem has been treated by Hoskins & Bretherton (1972)† for the special case $q = 0$ and $N_\infty = 0$. The resulting frontal concentration of density, velocity and surface particles as part of the preconditioning process is shown in the following figures.

Hoskins & Bretherton assume solutions of the form

$$u = \gamma x + u'(y, z, t), \qquad v = -\gamma y + v'(y, z, t), \tag{8.2}$$

where γx, $-\gamma y$ is an underlying deformation field which strains an initial density transition

$$\rho = \rho_0 + \Delta\rho \tanh(y/\Delta y) \tag{8.3}$$

† It is not easy to write down operational formulae based on the Hoskins & Bretherton paper. We are greatly indebted to D. Rudnick (personal communication, 1999) for the following discussion.

toward a frontal formation. MacVean & Woods (1980) present arguments for a strain of the order of $\gamma = 10^{-5}\ \mathrm{s}^{-1} = 0.1f$, and we shall use this value; it can be interpreted as a mesoscale variability of $\frac{1}{4}\ \mathrm{m\,s}^{-1}$ over a distance of 25 km. Espedal *et al.* (1998) have reported convergent currents of the order of $10^{-3}\ \mathrm{s}^{-1}$ on a slick zone off the coast of Norway; Rudnick (1996) chooses $10^{-6}\ \mathrm{s}^{-1}$. Initial conditions are $(u', v', w') = 0$. Boundary conditions are $w = 0$ at $z = 0$ and $z = -H = -200$ m; we interpret $\frac{1}{2}H = 100$ m as the depth of a mixed layer.

Subject to these conditions and the approximations resulting from the cross-front length-scale being much shorter than the long-front scale, the equations can be solved as a function of the *state* of strain $\tau = \int_0^t \gamma(t')\,\mathrm{d}t'$ independent of the detailed history of the *rate* of strain $\gamma(t)$. For the case of constant γ, τ is a dimensionless time in units of roughly one day.

As before, horizontal coordinates are scaled by Δy, and vertical coordinates by H. The initial dimensionless density distribution is given by

$$\rho(y_0) = \frac{\tilde{\rho} - \tilde{\rho}_0}{\Delta\tilde{\rho}} = \tanh y_0. \tag{8.4}$$

Solutions for the particle positions can be written

$$\left.\begin{aligned} x(x_0, y_0, 0, \tau) &= [x_0 + \tfrac{1}{2}Bu(f/\gamma)\rho'\tau]\mathrm{e}^{\tau}, \\ y(y_0, z_0, \tau) &= y_0\mathrm{e}^{-\tau} + Bu\,\rho'(\tfrac{1}{2} + z)\mathrm{e}^{\tau}, \\ z(y_0, z_0, \tau) &= \frac{1}{2L}[-1 + \sqrt{1 + 4L(\tfrac{1}{2} + z_0) + L^2}], \end{aligned}\right\} \tag{8.5}$$

where $\rho' = \mathrm{d}\rho/\mathrm{d}y_0$, etc.,

$$Bu = \frac{g\Delta\rho/\rho}{f^2\Delta y}\frac{H}{\Delta y}, \qquad L = \tfrac{1}{2}Bu\,\rho''\mathrm{e}^{2\tau}$$

is the Burger number, and $Bu \ll 1$ to satisfy initial conditions. For the numerical values $\Delta\rho/\rho = 10^{-4}$ (2×10^{-4} for the total frontal transition), $f = 10^{-4}\ \mathrm{s}^{-1}$, $\gamma = 10^{-5}\ \mathrm{s}^{-1}$, $\Delta y = 50$ km, $H = 200$ m, we have $Bu = 1/125$.

Velocities follow from $u = \mathrm{d}x/\mathrm{d}\tau$, etc. Horizontal velocities are scaled by $\gamma\Delta y = 0.5\ \mathrm{m\,s}^{-1}$, vertical velocities by $\gamma H = 0.2\ \mathrm{cm\,s}^{-1}$. The results are

$$\left.\begin{aligned} u(x, y, z, \tau) &= x + Bu(f/\gamma)(\tfrac{1}{2} + z)\rho'\mathrm{e}^{\tau}, \\ v(y, z, \tau) &= -y_0\mathrm{e}^{-\tau} + Bu(\tfrac{1}{2} + z + w)\rho'\mathrm{e}^{\tau}, \\ w(y, z, \tau) &= \frac{-Bu(z + z^2)\rho''\mathrm{e}^{2\tau}}{1 + Bu(\tfrac{1}{2} + z)\rho''\mathrm{e}^{2\tau}}. \end{aligned}\right\} \tag{8.6}$$

The functions $y_0(y, z, \tau)$, $\rho'(y, z, \tau)$, etc., are obtained by numerical methods. It can be verified that potential vorticity is conserved in accordance with (8.1).

Figure 28 shows the development of a density front and eastward jet in accordance with (8.5) and (8.6). The tilt of the initially vertical isopycnals diminishes according to $\delta z/\delta y = (Bu\,\rho')^{-1}\mathrm{e}^{-\tau}$. The cross-front gradient

$$\frac{\partial\rho}{\partial y} = \frac{\partial\rho/\partial y_0}{\partial y/\partial y_0} = \frac{\rho'}{\mathrm{e}^{-\tau} + Bu(\tfrac{1}{2} + z)\rho''\mathrm{e}^{\tau}} \tag{8.7}$$

Table 1. *Definition of critical isopycnals*

	central isopycnal $\rho_{\mathrm{C}}(y_0)$	frontal isopycnal $\rho_{\mathrm{F}}(y_0)$
y_0	0	$\pm\sinh^{-1}\sqrt{\frac{1}{2}} = \pm 0.66$
$\rho = \tanh y_0$	0	$\pm\sqrt{\frac{1}{3}} = \pm 0.58$
$\rho' = \operatorname{sech}^2 y_0$	1	$+\frac{2}{3}$
$\rho'' = -2\operatorname{sech}^2 y_0 \tanh y_0$	0	$\mp\frac{4}{3\sqrt{3}} = \mp 0.77$
$\rho''' = \operatorname{sech}^2 y_0(\operatorname{sech}^2 y_0 - 2\tanh^2 y_0)$	1	0

becomes infinite in *finite* time $\tau^\star$ when the denominator vanishes. The earliest possible instability is associated with maximum negative ρ'', hence $\rho''' = 0$ with roots $y_0 = \pm\sinh^{-1}(\sqrt{\frac{1}{2}})$ defining the 'frontal isopycnals' $\rho_{\mathrm{F}} = \pm\sqrt{\frac{1}{3}}$ on the cyclonic/anticyclonic sides of the developing jet (table 1). The discontinuity first develops at the surface, $z = 0$, at a time

$$\tau^\star = \tfrac{1}{2}\ln\left(\frac{3\sqrt{3}}{2Bu}\right) = 2.89 \tag{8.8}$$

for $Bu = \frac{1}{125}$. The logarithmic dependence of $\tau^\star$ on the frontal parameters lends some credence to the conclusion that the front will form in a few days. Isotacs of the developing eastward jet become increasingly concentrated at the cyclonic side. Eventually $\partial u/\partial y \to \infty$ at the same time and place as $\partial\rho/\partial y \to \infty$, so that the cyclonic density and velocity fronts coincide. We note a dramatic downward jet beneath the cyclonic north wall and a broad zone of upwelling on the anticyclonic side.

Figure 29 shows cross-front surface profiles at various times for density and velocities (the vertical velocity is profiled just beneath the surface). The eastward jet $u(y)$ develops a sharp cyclonic front at the north flank, and a weak anticyclonic front at the south flank, corresponding to extremi in positive and negative Rossby numbers, respectively. The frontal development is eventually limited by vertical shear at the cyclonic front just beneath the surface at time $\tau = 2.75$.

The procedure is as follows. Using $u(x, y, z, \tau)$ from (8.6) yields

$$Ri(y, z, \tau) = 1 + Bu(\tfrac{1}{2} + z)\rho''\mathrm{e}^{2\tau}. \tag{8.9}$$

The Rossby number is readily computed from $-1 - Ro + Ri^{-1} = 0$. The negative maximum $\rho'' = -4\sqrt{1/27}$ defines a minimum (unstable) Richardson number and a maximum cyclonic Rossby number; for $\tau = \tau^\star$ the values are $Ri = 0$ and $Ro = \infty$. The positive extremum $\rho'' = +4\sqrt{1/27}$ is associated with a maximum (stable) Ri and maximum anticyclonic $-Ro$; for $\tau^\star$ the values are $+2$ and $-\frac{1}{2}$. Vertical shear instability is attained before the formation of a discontinuous front. Equation (8.9) yields $\tau = 2.75$ for $Ri = \frac{1}{4}$, hence $Ro = +3$. The associated anticyclonic values are $Ri = 1.75$ and $Ro = -0.43$. The conclusion is that cyclonic Rossby numbers well above unity can be sustained before vertical shear instability sets in, but that anticyclonic Rossby numbers fall far short of -1 (table 2).

Figure 30 emphasizes the rapid development just prior to and following Richardson instability. It remains to interpret the situation in terms of a redistribution of passive surface tracers (figure 31). Four particles initially form a rectangle centred

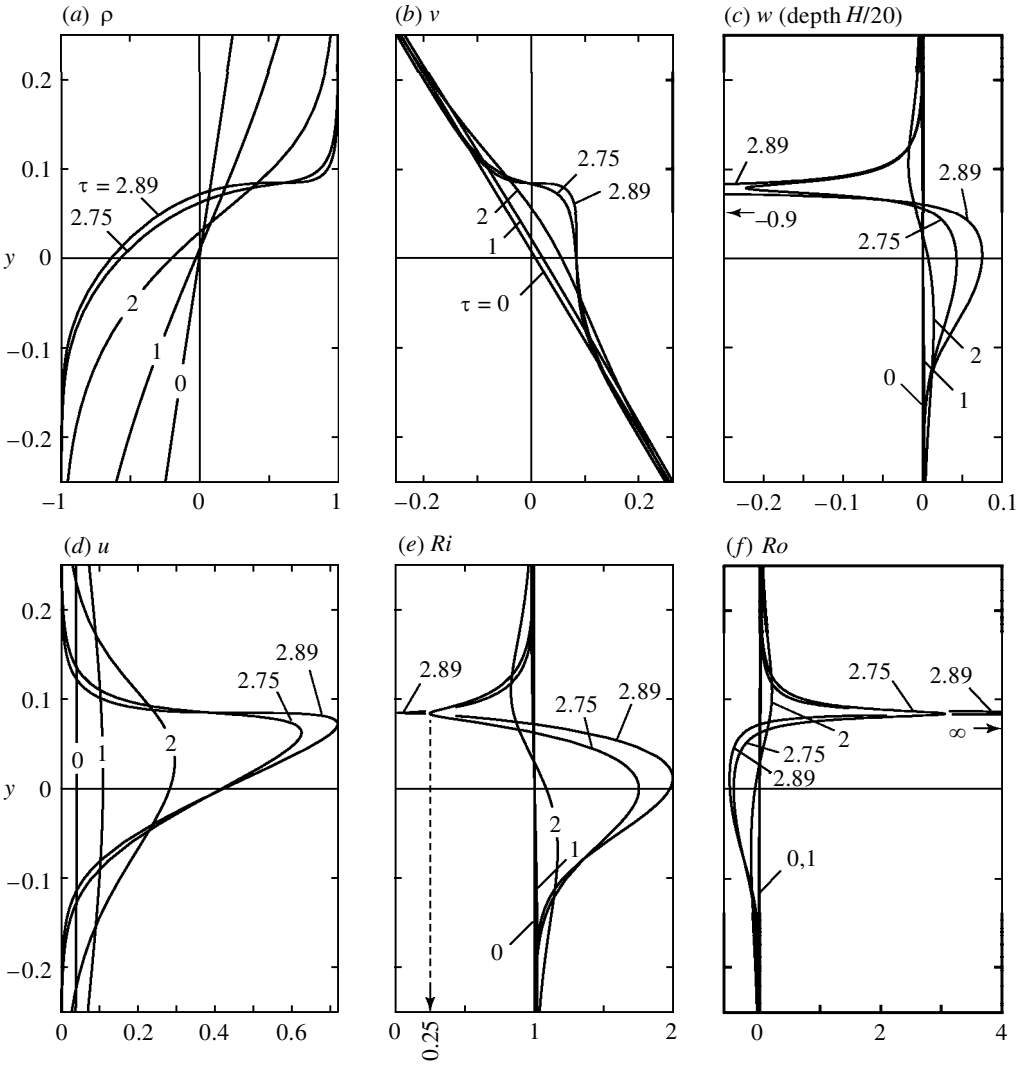

Figure 29. Cross-frontal surface profiles (y northward in 50 km units) at $x = 0$ and indicated times τ. At $\tau = 2.75$ the vertical shear becomes critical ($Ri = 1/4$) at $y = +0.08$, 4 km northward of the centre of the initial density transition. The Rossby number increases rapidly from $Ro = 3$ at $\tau = 2.75$ to infinity at $\tau = 2.89$ along an abrupt cyclonic north wall, whereas $Ro = -0.5$ in the weak anticyclonic southern flank. The north wall is associated with a sharp tongue of downwelling (order 0.1 cm s^{-1}); the south flank is in a broad zone of upwelling (0.01 cm s^{-1}). A weak cross-frontal northward flow $v(y)$ (order 0.1 m s^{-1}) develops at the late stages of frontogenesis.

on the frontal isopycnals with dimension $\delta x_0, \delta y_0$. From (8.5), this is distorted into a parallelogram with dimensions

$$\delta x = \mathrm{e}^{\tau}\delta x_0, \qquad \delta y = (\mathrm{e}^{-\tau} + \tfrac{1}{2}Bu\,\rho''\mathrm{e}^{\tau})\delta y_0$$

of area

$$\delta x \delta y = (1 + \tfrac{1}{2}Bu\,\rho''\mathrm{e}^{2\tau})\delta x_0 \delta y_0 = Ri\delta x_0 \delta y_0.$$

Table 2. *Critical stages in the development of frontal shear*

(The parameter $\Pi = (8/\sqrt{3})Bu\,\mathrm{e}^{2\tau}$; τ_1 and τ_2 are dimensionless times (very roughly in days) for Bu_1, Bu_2, respectively. Numerical values are mixed layer depth $\frac{1}{2}H = 100$ m, $f = 10^{-4}$ s^{-1}, $\Delta\rho/\rho = 10^{-4}$, $\Delta y_1 = 50$ km, $\Delta y_2 = 25$ km. $Bu_1 = 0.008$, $Bu_2 = 0.032$.)

			cyclonic		anticyclonic		
Π	τ_1	τ_2	*Ro*	*Ri*	*Ro*	*Ri*	comments
0	0	0	0	1	0	1	
1.2	1.74	1.05	0.11	0.9	−0.09	11	ambient ocean condition
4	2.34	1.65	1/2	2/3	−1/4	4/3	
6	2.55	1.85	1	1/2	−1/3	3/2	start of cat's-eye formation
9	2.75	2.05	3	1/4	−0.43	1.75	vertical shear instability
12	2.89	1.49	∞	0	−1/2	2	frontal discontinuity

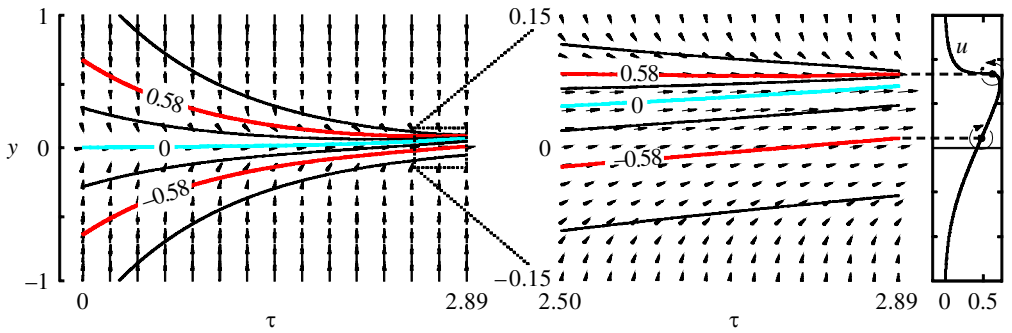

Figure 30. Surface view of frontal development. The 'frontal isopycnals' ($\rho_\mathrm{F} = \pm\sqrt{1/3} = \pm 0.58$) are at the centre of the developing cyclonic/anticyclonic shears. A cyclonic frontal discontinuity forms at $\tau = 2.89$, with the late development shown on an enlarged scale. Velocity vectors exhibit increasing frontal shear, especially on the cyclonic side. The right panel shows the eastward velocity u (0.5 m s^{-1} units) at $\tau = 2.89$.

On the cyclonic side (negative ρ'') the area is compressed by 4:1 at the time $\tau = 2.75$ when $Ri = \frac{1}{4}$, and infinitely compressed at $\tau = 2.89$; the area is *extended* (by a factor 1.75, 2 for $\tau = 2.75, 2.89$) on the anticyclonic side. For both cases the along-front extension is by a factor e^τ.

The situation can again be summarized in a frontal stability diagram (figure 32). Potential vorticity is zero, and so the Richardson number is uniquely related to the Rossby number, with vertical shear and static instabilities indicated by the shaded areas. The history of seven isopycnals is shown. The initial growth of vorticity is slow. The cyclonic frontal isopycnal $\rho_\mathrm{F} = +0.58$ is the first to reach $Ro = 1$ (at $\tau = 2.55$); subsequently the vorticity rapidly grows to $Ro = 3$ (at $\tau = 2.75$) when critical vertical shear is reached near the surface. In contrast, the most rapidly growing anticyclonic isopycnal $\rho_\mathrm{F} = -0.58$ never grows beyond $Ro = -\frac{1}{2}$ (at $\tau = 2.89$). The central isopycnal $\rho_\mathrm{C} = 0$ remains at zero Rossby number. Critical stages are summarized in table 2.

The Hoskins–Bretherton model lends itself to preconditioning for the formation of cyclonic vortices, both from the point of view of generating super-f cyclonic shear and compacting surfactants for visualization.

9. Frontal preconditioning

Analytical models and numerical simulations both exhibit destabilizing effects for anticyclonic frontal formation, but not so for the cyclonic case. This parallels the discussion of vortex formation (§ 6).

(*a*) *Breaking symmetry in frontal models*

We have examined two types of frontal models. Traditional models of the Margules type (§ 7) lead to ramp-like (but not necessarily discontinuous) frontal transitions of density and velocity, superimposed upon a stable density configuration. The initial transition, if sufficiently gradual, can be either cyclonic or anticyclonic. As the front sharpens, the vertical density gradient strengthens for the cyclonic case and weakens for the anticyclonic case. In the anticyclonic case this leads to a decrease in Richardson number (Ri in equation (7.18)), early vulnerability to vertical shear instability, and ultimately to static instabilities. The model can be made to maintain the overall potential vorticity in the frontal zone.

A Lagrangian treatment which conserves the density and potential vorticity of particles (§ 8) has been made tractable for the special case of zero potential vorticity and zero initial stratification by Hoskins & Bretherton (1972). It was adapted to oceanic conditions by MacVean & Woods (1980). The model leads to the generation of jet-like (rather than ramp-like) frontal currents with intensive downdrafts on the cyclonic side and broad regions of upwelling on the anticyclonic side, as observed along the Malta Front by Woods *et al.* (1977). The model predicts in some detail the tilting, crowding and focusing of the frontal isopycnals, and is a useful guide in discussions of the frontal preconditioning toward the vortex and spiral formation. A weakness is the specific conditions under which it has been derived.

(*b*) *Breaking symmetry in numerical simulations*

The stability of rotating frontal shear flow has been considered in extensive numerical simulations by Métais *et al.* (1995). The 'mixing layer' solution (with a ramp-like distribution as in § 7) is stabilized by rotation for $-1 < Ro < +\infty$. For *moderate* anticyclonic rotation, $Ro < -1$, the flow is strongly destabilized, with strong longitudinal alternate vortex tubes slightly inclined with respect to the x-direction. The horizontal shear vortices are suppressed. The situation is similar for a rotating 'wake' (corresponding to a symmetrical jet), with three-dimensional perturbations suppressed for $-1 < Ro < +\infty$. But for $Ro < -1$ on the anticyclonic side, the two-dimensional anticyclonic vortices disappear and are replaced by intense longitudinal vortices. 'Thus a moderate rotation has produced a dramatic symmetry breaking in the wake topology.'

In § 8 we dealt with a frontal jet formation dominated by strong shear on the cyclonic side. The work of Métais *et al.* suggests that even for a symmetric jet of sufficient strength, $|Ro| > 1$, inertial instability on the anticyclonic side would lead to a dominance of two-dimensional flow on the cyclonic side.

(*c*) *Shear in the open ocean*

We contrast these frontal conditions with the 'normal' open-ocean situation. Horizontal temperature and salinity perturbation in the upper ocean exhibit 'spiciness' (hot and salty) in the sense that their contributions to the density perturbation $\Delta\rho = a\Delta\theta + b\Delta S$ show a high degree of cancellation (a is negative). From 1000 km tows in the North Pacific, Rudnick & Ferrari (1999) find compensated temperature and salinity 'jumps' on all scales but only very weak density transitions. In the mixed layer in the winter a representative value is $N_\infty = 25f = 2.5 \times 10^{-3}$ s^{-1} with 100% variability. The parameter $He = (N^2 - N_\infty^2)/N_\infty^2$ is then of the order of $\pm$ unity, with possibly much higher values for locally and temporarily uncompensated temperature or salinity perturbations. Measurements of velocity on the same tows (D. Rudnick, personal communication, 1999) yield a distribution in Rossby numbers shown in figure 33 with $Ro \approx 0 \pm 0.12$. We can interpret this magnitude in terms of mesoscale velocity perturbations by ± 0.25 m s^{-1} over distances of the order of 50 km. There is little distinction here between cyclonic and anticyclonic shear, though the distribution shows a slight skewness in favour of cyclonic shear.†

10. Hypothesis of ocean spirals

The development of spiral eddies which we propose is cartooned in figure 34. The geostrophically balanced ambient ocean vorticity of the order of $\pm 10^{-1} f$ is enhanced by local intermittent frontogenic processes. The emphasis is on baroclinic y, z-processes (x is taken along the front), with concentration of surfactants along a converging line. When the frontal shear becomes comparable with f, instabilities in the x, y-plane lead to cross-frontal flow accompanied by the development of a cat's-eye circulation pattern. Surfactants are generally present on the ocean surface; they are often concentrated in streaks responding to stream-wise rolls in the atmospheric boundary layer. The cat's-eyes circulation twists the convergence line and the neighbouring linear features into a cyclonic spiral which stretches and further thins the lines of surfactant concentration.

The frontal preconditioning stage (§ 9) is strongly model dependent. We have assumed two types of frontal formation. A softened Margules front has a ramp-like density and velocity frontal transition, cyclonic or anticyclonic. The anticyclonic fronts are limited to sub-f vorticities by vertical shear instability, possibly by static instability, and ultimately by inertial instability. There are no such limits to the cyclonic fronts. Our treatment consists of independent realizations at constant potential vorticity, and does not explicitly allow for the Lagrangian dynamics of vorticity conservation.

Our second model follows the Lagrangian formalism of Hoskins & Bretherton (1972). An initial horizontal density transition in a thoroughly mixed layer with an imposed horizontal flow convergence develops into a jet with a strong cyclonic 'north wall' and a weak anticyclonic southern flank.‡ The north wall eventually reaches vertical shear instability, but not until horizontal shear of the order of $+3f$ has been attained. At the same time the anticyclonic vorticity is only $-\frac{1}{2}f$ at most.

† This has been confirmed by Rudnick from measurements in other ocean basins. The sampling interval of 3 km would suppress any skewness associated with very sharp gradients.

‡ For convenience we use 'north' as a synonym for the up-front direction, towards the cold side of the jet.

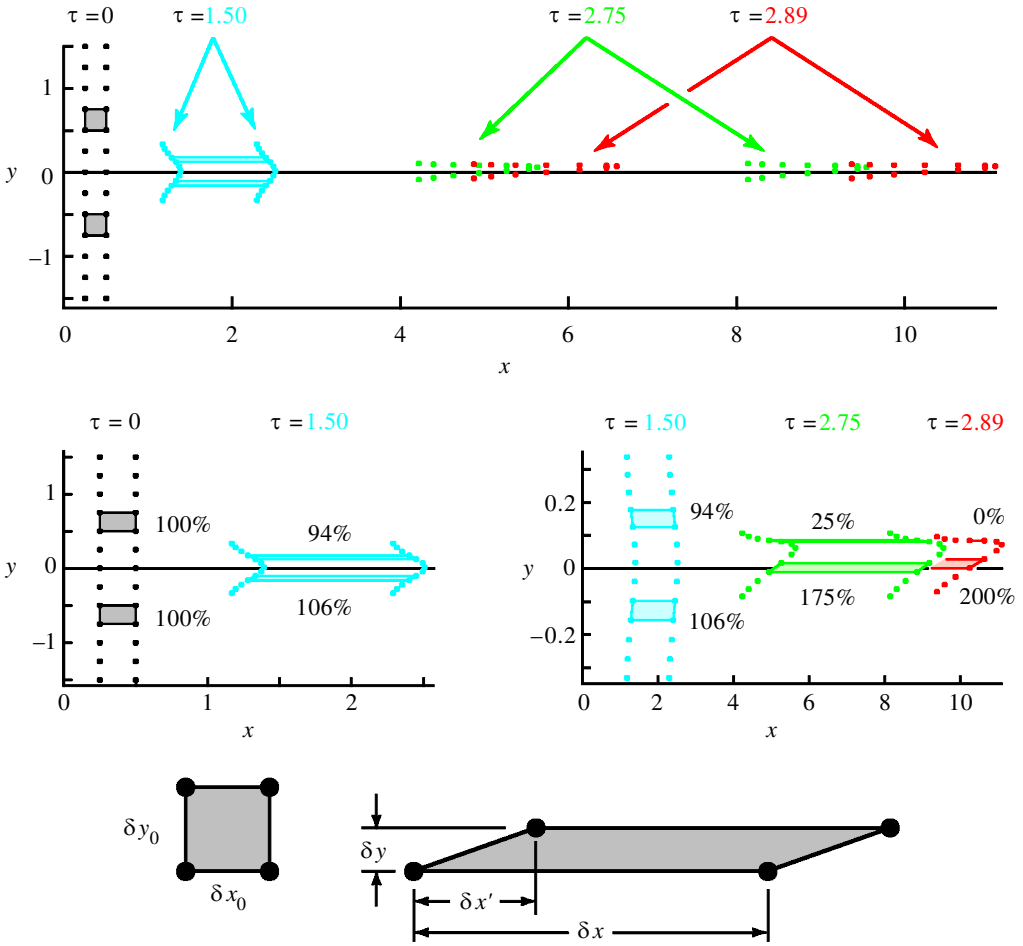

Figure 31. Successive snapshots of surface particles. Two lines of 13 particles each which are initially normal to the front are turned and stretched along the front. The initial redistribution from $\tau = 0$ to 1.5, and subsequent surface straining from $\tau = 1.5$ to 2.75 (the onset of vertical shear instability) and 2.89, are shown below on an enlarged and distorted scale. The shaded squares designate the initial positions of the particles just north and south of the developing fronts. For the cyclonic front the square thins and stretches, with a 4:1 areal compression at $\tau = 2.75$ (infinite compression at $\tau = 2.89$, only the rightmost dots are shown in the detail). The anticyclonic square also thins and stretches, but the overall area *expands* by a factor 2.

We visualize the following course of events. The starting point is a mesoscale variability associated with $\Delta u = \pm\frac{1}{4}\,\mathrm{m\,s^{-1}}$, $\Delta y = 25\,\mathrm{km}$, hence $\zeta = \pm 0.1f$. After a day or two of frontal development (taking an initial τ of 1.74 from table 2) we have $\Delta y = 2.5\,\mathrm{km}$ and $\zeta = +1f/-\frac{1}{3}f$ at the north/south flanks of the developing jet. Our previous choice for the initiation of the Stuart cat's-eyes was 3 km and f, so this is a suitable hand-over time: beginning with $Ro = +1$, the cyclonic frontal shear zone becomes the breeding ground for spiral eddies with expected time-scale of the order of f^{-1} and spatial scale of the order of the Rossby radius, long before significant anticyclonic vorticity has been generated. Should the anticyclonic f-limit

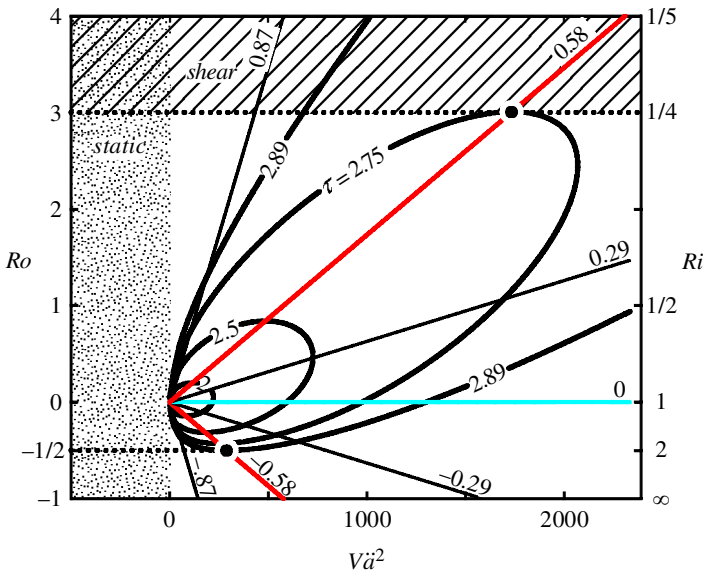

Figure 32. Frontal stability diagram for the Lagrangian model of Bretherton & Hoskins (1972). The red radial lines show the growth in Ro and $V\ddot{a}^2 = N^2/f^2$ along the frontal isopycnals $\rho_F = \pm 0.58$. The cyclonic vorticity grows rapidly to $Ro = +3$ at time $\tau = 2.75$ (when first encountering vertical shear instability $Ri = 1/4$) and to $Ro = \infty$ at $\tau = 2.89$. The anticyclonic vorticity grows slowly to $Ro = -1/2$ at $\tau = 2.89$. The Rossby number remains at zero along the blue central isopycnal $\rho_C = 0$.

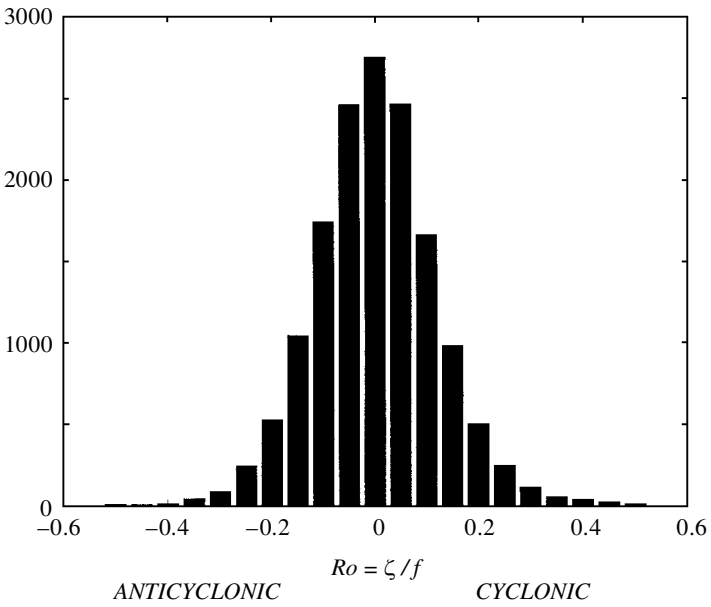

Figure 33. Rossby number in the upper 250 m sampled at 3 km intervals along 140° W from 25° N to 35° N in the North Pacific (Rudnick & Ferrari 1999). At large $|Ro|$ there is a slight skewness in favour of cyclonic vorticity.

be broached (as may be the case with other processes such as the separation of flow past islands, figure 10), the further development is limited by centrifugal and inertial instabilities. Cyclonic cat's-eyes are exempt from centrifugal and inertial instabilities.

In parallel with the development of strong cyclonic shear there is surface convergence which further concentrates ambient surfactant material into a narrow band. There is no such convergence on the anticyclonic side. From this point of view, if there were no other lines present, one could attribute the cyclonic predominance to a visibility issue.

The cartoon leans towards a Hoskins–Bretherton model for providing a powerful apparatus in the analysis in the preconditioning stage. A weakness is the almost singular dependence on zero potential vorticity, zero initial density stratification and a somewhat arbitrary imposed strain field.

We take the following positions on the three questions asked in the introduction:

(A) *How are the spirals wound?* By the cat's-eye circulation associated with horizontal shear instability. But the answer is far from unique: almost any spiral pattern of particle distribution can be interpreted as a legacy of past vortex deformation.

(B) *How is symmetry broken in favour of cyclonic rotation?* Finding *one* credible process was our initial focus. There are in fact many processes favouring the cyclonic rotation: (i) the relatively rapid development of super-f shear on the cyclonic side of frontal jets (as described in § 8); (ii) shear, static, centrifugal and inertial instabilities which selectively target the anticyclonic development of cat's-eye vortices (§ 6 *f*);† The central issue is not (as we had asked initially) *why the dominance of cyclonic eddies?*, but *which of the proposed mechanisms limits the formation of anticyclonic vortices?* Why did the dog *not* bark?‡

(C) *What makes the spirals visible?* Most of the linear features seen on the halftone figures are wind streaks associated with atmospheric rolls, generated by winds prior to the relatively calm conditions favourable to detection in the sunglitter and on SAR. Eddies are then visible through their action of twisting and straining these linear features, even without active frontal convergence. However, the frontal convergence which produces the shear required for the subsequent cat's-eye formation will also produce shear lines. All lines in the near-field of the stagnation streamline, streaks and shear lines, accumulate onto this streamline (figure 21) and contribute to its visibility (figures 1, 3 and 11).

With regard to the concentration of spiral images in the fall in the Cretan Sea, we note that the seasonal northwesterly to northerly 'Meltemi' winds of the eastern Mediterranean end in October when strong events are followed abruptly by the calm conditions required for visibility. With regard to the equatorial void, both frontal models assume the thermal wind relation which is not applicable near the equator, where the mid-latitude Rossby radius Cf^{-1} (10 km at 30° latitude for $C = 1\ \mathrm{m\ s^{-1}}$) increases to within a factor of 2 (say) of the equatorial Rossby radius $\sqrt{C/(2\beta)} =$

† Contrary to our findings, numerical models show that anticyclones are more persistent than cyclones when the flow evolves freely from random initial conditions (Polvani *et al.* 1994; Shen & Evans 1994).

‡ Dr Watson quotes Inspector Gregory asking Sherlock Holmes (Doyle 1892): 'Is there any other point to which you wish to draw my attention?' 'To the curious incident of the dog in the night-time.' 'The dog did nothing in the night-time.' 'That was a curious incident' remarked Sherlock Holmes.

140 km, with $\beta = \mathrm{d}f/\mathrm{d}y = 2 \times 10^{-8}\ \mathrm{m}^{-1}\ \mathrm{s}^{-1}$. This happens at *ca.* 6° latitude. The appropriate time constant is then 10 times and the horizontal shear is one-tenth of what it is outside the tropics. We also note a resemblance of the global spiral distribution to the relatively high level of abundance of natural biogenic films in marginal seas, and the relatively low level of films (productivity) in the Southern Hemisphere (Bresciano *et al.* 1998).

In our analytical treatment we have separated the frontal preconditioning from the horizontal shear instability. At one extreme the instability might proceed from ambient shear without any appreciable frontal preconditioning. At the other extreme, frontogenesis proceeds rapidly toward a Margules-like sharp front (with *a priori* elimination of anticyclons) leading to frontal instability in the Orlanski (1968) and Iga (1993) sense. Yet another possibility is that the problem cannot be sensibly separated into sequential baroclinic and barotropic phases, but needs a full three-dimensional treatment. Ultimately these issues will have to be resolved by numerical modelling. Eldevik & Dysthe (1999) have done numerical simulations starting with a cyclonic shear zone of *ca.* 2 km width. They generate a short-scale predominantly baroclinic frontal instability accompanied by particle concentrations with spiral-like character.

Spiral eddies are a manifestation of a sub-mesoscale oceanography which may constitute an important link in the balance of generating and dissipating ocean processes. We have already associated the preconditioning phase with a vigorous vertical circulation. The spiral circulation contributes to horizontal diffusion. A rough estimate of the eddy diffusivity is given by $\kappa = c\,l'u'$ with $c = \frac{1}{4}$ (table 4.1 of Tennekes & Lumley 1972). For a characteristic length l' we take the minor axis of the Stuart core, and for u' the maximum velocity along the braid. The result is

$$\kappa = 4k^{-2} f \sqrt{\frac{\alpha}{1+\alpha}} \cosh^{-1}(1+\alpha) \approx 10^3\ \mathrm{m}^2\ \mathrm{s}^{-1}$$

for $k = 3 \times 10^{-4}\ \mathrm{m}^{-1}$, $f = 10^{-4}\ \mathrm{s}^{-1}$, $\alpha = 1$. This is a representative value for horizontal eddy diffusivities.

Spiral eddies are at an awkward scale, with features virtually impossible to recognize from shipboard, and too large to be encompassed from aircraft. The discovery had to await the early space missions. A separate question is why the problem has received so little attention in the intervening 30 years. We assert that the fashion during these years has been statistical rather than phenomenological descriptions of ocean features, and here we are concerned with a truly phenomenological problem.

We acknowledge the singular contribution of Paul Scully-Power, the first and last (so far) Oceanographer-Astronaut. Half of the photographs reproduced in this paper were taken by Scully-Power with a hand-held Hasselblad camera. We thank C. Cox, C. Dysthe, T. Eldevik, D. Farmer, C. Garrett, O. M. Johannessen, J. Miles, R. Parker, S. Thorpe and the two referees for their helpful comments. Support was received from MEDEA. We are indebted to Ms Susan Runco, curator of the Still Photo Archive, NASA Johnson Space Flight Center. We are greatly indebted to D. Rudnick for clarification of the Hoskins–Bretherton model. W.M. holds the Secretary of the Navy Chair in Oceanography. L.A.'s research is supported by the Office of Naval Research. F.Z. conducted his work as Green Fellow at the Scripps Institution of Oceanography. Illustrations were prepared by Breck Betts.

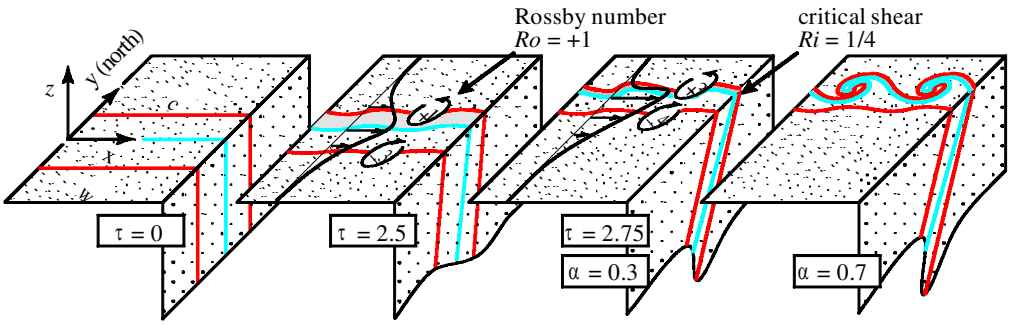

Figure 34. Cartoon for the generation of ocean spirals. An initial horizontal density gradient (cold to the north) in a mixed upper layer is portrayed by the central isopycnal (blue) and the two frontal isopycnals (red). With increasing time τ, the isopycnals move together, tilt towards the north, translate northward and eventually converge at the surface on the positive frontal isopycnal. A developing eastward jet turns increasingly asymmetric, with strong cyclonic shear (large positive Rossby numbers) to the north and weak anticyclonic shear to the south. A downward tongue under the 'north wall' and upwelling to the south modify the depth of the mixed layer. The Rossby number along the north wall increases rapidly from +1 to +3 between the times $\tau = 2.5$ and 2.75, when critical vertical shear develops near the surface. Horizontal shear instability develops along the north wall for $Ro > 1$, with an intensifying cat's-eye flow pattern. Ambient surfactants are compressed and aligned along the north wall, and wound into cyclonic spirals.

Appendix A.

(*a*) *Extracts from the Paul Scully-Power unedited tape recording*

MET:† 00:11:01 ... a neat spiral near the coastline on the Black Sea.

MET:01:00:52 ... superb spirals and fronts in the central Mediterranean.

MET:01:00:53 ... incredible spirals and contorted structure. Just spectacular spiral eddies throughout this whole region, just spectacular.

MET:01:00:54 We're coming over Cyprus now ... The more you see here, the more you just see of more spiral eddies, fronts and of very long internal waves. They're not quite as long as solitons, but getting that way, they have soliton structure. The Mediterranean is equally as complex as the Mozambique Channel, if not more so. There's connected spirals all the way across from coastline to coastline, just spectacular dynamics. Perhaps the more interesting thing is that these quasi-solitons that I've seen are laid right across the spiral structure ...

MET:01:02:49 We have just come across the Gulf of Aden, the perfect spectacular point for the sunglitter but there was absolutely no structure there whatsoever.

MET:02:01:01 We have just come over the eastern Mediterranean with the most spectacular sun glint pass you have ever seen: mile after mile of arranged, in a line, spiral eddies.

MET:02:06:54 (Cape Cod). There was one or two small spirals and quite a number of long linear streaks; they did not seem to be organized in any particular pattern.

† Mission elapsed time starting 5 October 1984: 0703 AM EDT.

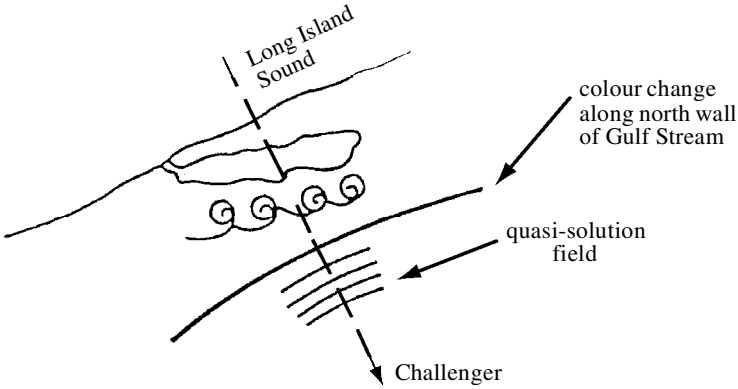

Figure 35. Sketch made on REV69.

MET:03:23:00 When we passed Lake Van (Gulf of Oman??) back a few minutes ago, there's a neat set of spiral eddies in the middle of that which seem to have a constant pattern; they've been there the last three days.

MET:04:10:50 We're on Rev #72, coming down the eastern North Pacific. When you see the ocean out here even this far from shore, once again you continue to see these spiral structures connected by a linear front; some of them are linear; some are not linear but at least they're slick patterns, long thin slick patterns connecting the spirals ... maybe the whole ocean is like this. I don't know.

MET:05:00:03 Took wonderful photo ... of the spiral eddies between Ireland and England.

MET:05:00:04 ... Coming down towards the southern shores of the Mediterranean ..., you see the water and once again there's some small spirals. There also appears to be pretty long streaks, not internal waves, but long streaky patterns in the water. They're fine streaks forming streaky patterns that are running parallel to the coastline. As we come up on the coast of Egypt I guess what we are looking at is some long lines of internal waves and then right near the shore we go from that pattern into classic spirals connected with long streamers.

MET:05:00:26 ... Low Sun angles in the glint can be very useful if you're trying to scan a rather long area ...

MET:05:07:34 Gulf of Mexico ... plenty of spirals.

MET:05:23:46 Straight of Dover. Standard pattern of slicks and tight spirals. (time gap) Once again as we approach the (southern Mediterranean) coastline here, there's just a whole series of convoluted spirals, just like the Stevenson spiral in the Agulhas current.

(*b*) *Extracts from on-board written notes*

MET:00:23:11 orbit 16. Great spiral in the Gulf of Oman, together with many linear slicks and one strong front approx. 30 mi. long.

REV #17, The Red Sea has some structure, but the Gulf of Aden has none.

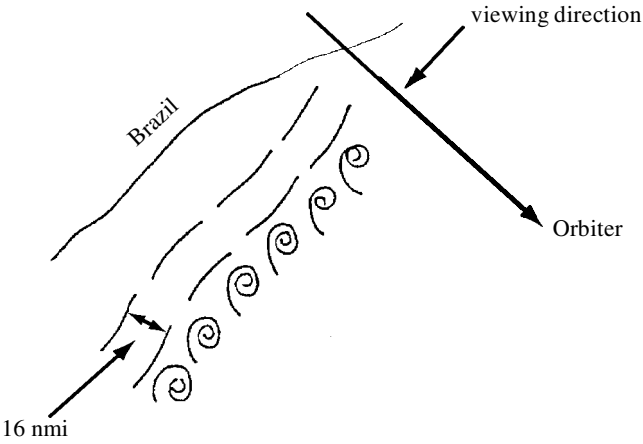

Figure 36. Sketch made on REV102.

REF #33, day 3. The Adriatic/Mediterranean section was incredible dynamics in the sunglint. Hundreds of miles of connected spiral eddies. At one point there were 4 or 5 spirals connected on a line like a VonKarman vortex street.

REV #69. Long Island Sound. Then clear over the Atlantic. As we headed southeast the first thing we saw was a long line of spiral eddies off the eastern shore of Long Island. Then smooth ocean. Then a series of long (approx. 100 mi) slicks which looked like quasi-solitons. There was a group of about four. Then it became obvious that these were aligned with a colour change in the ocean—the north wall of the Gulf Stream. The quasi-soliton field was aligned parallel to the north wall of the Gulf Stream and (I think) further toward the southeast (figure 35).

REF #73. Great sunglint/dynamics (slicks, front, spirals and internal waves) along eastern shore of the Kamchatka Peninsula.

REV #84. Tried out the polarizing filter by hand. The effects are dramatic—in the sunglint you can really see through the glint. But the most dramatic effect is coastal effects—high colour dynamics which are subtle to the naked eye are intensified and made higher contrast by the filter. Hence the dynamic boundaries which were subtle now jump out at you.

REV #97. English Channel: Clear for the first time. Saw the now 'typical' slicks and spirals.

REV #102. On crossing ... the southeast corner of Brazil, ... offshore there were two straight line slick/fronts which I timed to be 16 mi. apart ... and approximately 50 mi. long. Then I was able to look down the lie of the fronts and saw they were part of a larger pattern of similar slicks which stopped and started. On the seaward side of these fronts were a whole line of spiral eddies (figure 36).

Appendix B. Rossby adjustment in cylindrical coordinates

The collapse of a cylindrical dome in rotating coordinates yields a spiral-like distortion of a line of particles which resembles the observations along the East Greenland

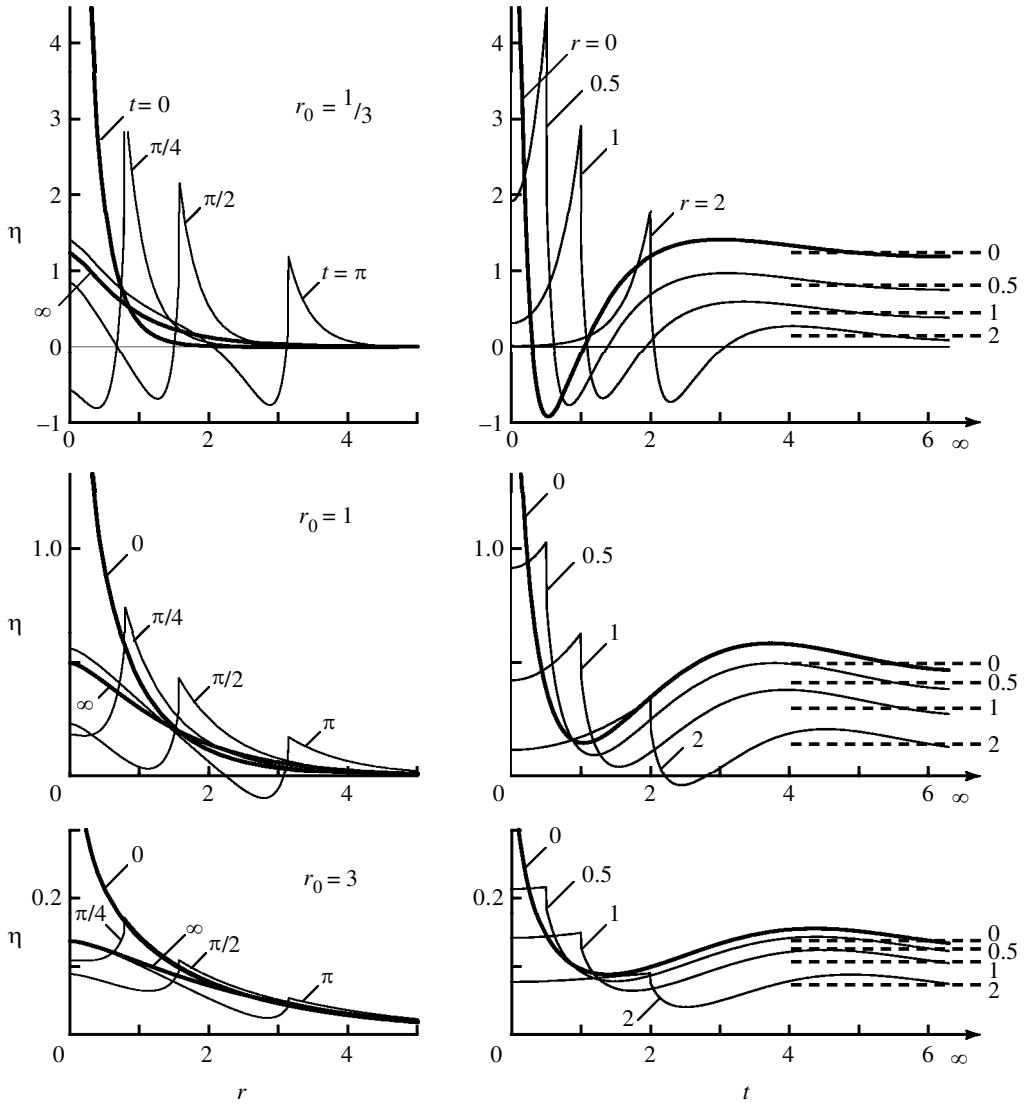

Figure 37. The collapse of a cylindrical peak in accordance with the 'Rossby adjustment problem'. An initial conical elevation (marked 0) in the lower layer of a two-layer fluid collapses to a dome (∞), which is in geostrophic balance with a cyclonic flow around the dome. The result is shown for an initial radius $r_0 = 1/3$, 1 and 3 times the internal Rossby radius of deformation r_{R}. The left panels show the elevations at various dimensionless times as a function of the dimensionless radial coordinate. The right panels show the time history at various points.

shelf (figure 13) and associated laboratory experiments (figure 18). The collapse is portrayed in figure 37. We append a derivation.

The simplest set of equations to break the symmetry is the traditional f-plane formulation

$$\frac{\partial \boldsymbol{u}}{\partial t} + \boldsymbol{f} \times \boldsymbol{u} = -g\nabla\eta, \qquad h\nabla \cdot \boldsymbol{u} = -\frac{\partial \eta}{\partial t}, \tag{B 1}$$

where η is the surface displacement and h the ocean depth. The governing length-scale is the Rossby radius of deformation

$$r_{\mathrm{R}} = \sqrt{gh} f^{-1}. \tag{B 2}$$

The results will be interpreted in terms of the equivalent two-layer problem using the Gill manipulation (Gill 1982, § 6.3). Let ρ_1 and ρ_2 designate the densities in the upper and lower layers, respectively. The surface displacement is $\eta_1(x, y, t)$, and the interior boundary is at $z = -h_1 + \eta_2(x, y, z)$. The flat bottom is at $z \equiv -(h_1 + h_2) = -h$. Then replacing the one-layer depth h by the equivalent depth $h_e = (\Delta\rho/\rho)(h_1 h_2/h)$ and the Rossby radius by $\sqrt{gh_e} f^{-1}$, all results for η apply to the doming η_2 of the interior layer. This presumes $\Delta\rho \ll \rho$ and $\eta_1 \ll \eta_2$.

We adopt dimensionless variables with horizontal length-scale r_{R}, time scale f^{-1} and vertical displacement scale αh. Then for zero initial velocity, the foregoing equations can be combined (Gill 1982, p. 192):

$$\left(\frac{\partial^2}{\partial t^2} - \nabla^2 + 1\right)\eta = \eta_0 = K_0\left(\frac{r}{\beta}\right), \qquad \nabla^2 = \frac{1}{r}\frac{\partial}{\partial r}\left(r\frac{\partial}{\partial r}\right), \tag{B 3}$$

with the boundary condition that $\partial\eta/\partial r = 0$ at $r = 0$, corresponding to the radial velocity $u = 0$ at $r = 0$. The solution to the steady homogeneous equation is $K_0(r)$, and this suggests taking $\eta_0(r) = K_0(r/\beta)$ for an initial elevation. This gives an (integrable) infinity at $r = 0$, but the initial volume

$$q_0 = 2\pi \int_0^\infty \eta_0(r) r \, \mathrm{d}r = 2\pi\beta^2$$

is finite (GR 6.56.16).† In dimensional units, using $\alpha = \tilde{A}/\tilde{H}$ as previously,

$$\tilde{q}_0 = 2\pi \int_0^\infty \tilde{y}_0(\tilde{r}) \tilde{r} \, \mathrm{d}\tilde{r} = 2\pi\alpha\beta^2 \cdot \tilde{H}\tilde{R}o^2 \quad (\mathrm{km}^3)$$

with α determined by comparison with the 'measured' volume displacement.

The homogeneous equation (B 3) is satisfied by terms $J_0(kr)\cos\omega t$ provided $\omega^2 = k^2 + 1$. Thus the homogeneous solution can be taken as

$$\eta_{\mathrm{HO}}(r, t) = \int_0^\infty \mathrm{d}k \, F(k) J_0(kr) \cos(t\sqrt{1 + k^2}) \tag{B 4}$$

with $F(k)$ to be determined by the initial displacement. As $t \to \infty$ we approach a steady-state governed by the equation,

$$\left[-\frac{1}{r}\frac{\partial}{\partial r}\left(r\frac{\partial}{\partial r}\right) + 1\right]\eta = K_0\left(\frac{r}{\beta}\right),$$

with the homogeneous and inhomogeneous solutions,

$$\eta_1(r) = CK_0(r), \qquad \eta_2(r) = \mu^{-2} K_0(r/\beta), \tag{B 5}$$

respectively. The boundary condition $\partial\eta/\partial r = 0$ at $r = 0$ is already satisfied by $\eta_{\mathrm{HO}}(r, t)$. Then since $K_0(r/\beta) \to \log r + \text{constant} + \text{order}(r^2 \log r)$ as $r \to 0$, we have $C = -\mu^{-2}$ and so

$$\eta_\infty(r) = \mu^{-2}[K_0(r/\beta) - K_0(r)] \tag{B 6}$$

† See Gradshteyn & Ryzhik (1965).

and

$$\eta(r,t) = \eta_\infty(r) + \eta_{\mathrm{HO}}(r,t). \tag{B 7}$$

To evaluate $F(k)$ we set $\eta(r,0) = \eta_0(r)$ and apply the Fourier–Bessel transform (GR 6.521.2), (GR 6.532.4):

$$\begin{aligned} F(k) &= \int_0^\infty \mathrm{d}rk\, r[\eta_0(r) - \eta_\infty(r)]J_0(kr) \\ &= \mu^{-2}\left[\frac{k}{1+k^2} - \frac{k}{1+\beta^2k^2}\right] = \frac{\beta^2k^3}{(1+k^2)(1+\beta^2k^2)}. \end{aligned} \tag{B 8}$$

It can be verified that

$$\eta_{\mathrm{early}}(r,t) = \eta_0(r)\mu^{-2}(1-\beta^{-2}\cos\mu t), \qquad \eta_0 = K_0(r/\beta), \qquad t < r, \tag{B 9}$$

obeys the differential equation and boundary condition except at $r = 0$. For $t \geqslant r$ we depend on a numerical evaluation of η_{H0}. We are indebted to R. Parker (personal communication) for the following procedure. To exploit the behaviour of the integrand in the complex plane, write

$$\eta_{\mathrm{HO}} = \mathrm{Re}\int_0^\infty \mathrm{d}k\, F(k)J_0(kr)\exp(\mathrm{i}(t\sqrt{1+k^2})).$$

We choose the contour as follows: a segment along real axis to k_0, then along $k_0 + \mathrm{i}y$, where $0 \leqslant y$. The choice of k_0 is very flexible, but $k_0 = 1$ seems to work well in practice, as it keeps well clear of the poles, but doesn't require many oscillations of the real integral. Thus

$$\eta_{\mathrm{HO}} = \int_0^{k_0} \mathrm{d}k\, F(k)J_0(kr)\cos(t\sqrt{1+k^2}) + \mathrm{Re}\int_0^\infty \mathrm{i}\,\mathrm{d}y\, F(k)J_0(kr)\exp(\mathrm{i}(t\sqrt{1+k^2})) \tag{B 10}$$

with $k(y) = k_0 + \mathrm{i}y$.

(*a*) *Velocities*

These are found from

$$\frac{1}{r}\frac{\partial}{\partial r}(ru) = -\alpha\frac{\partial\eta}{\partial t}, \qquad \frac{1}{r}\frac{\partial}{\partial r}(rv) = \alpha(\eta - \eta_0).$$

Using (B 5) we have

$$\begin{pmatrix} u_{\mathrm{early}}(r,t) \\ v_{\mathrm{early}}(r,t) \end{pmatrix} = \frac{\alpha K_1(r/\beta)}{\beta\mu^2}\begin{pmatrix} +\mu\sin\mu t \\ -(1-\cos\mu t) \end{pmatrix} \tag{B 11}$$

for $t \leqslant r$. From (B 7)

$$\begin{pmatrix} u_{\mathrm{late}}(r,t) \\ v_{\mathrm{late}}(r,t) \end{pmatrix} = \begin{pmatrix} 0 \\ v_\infty \end{pmatrix} + \alpha\int_0^\infty \mathrm{d}k\, J_1(kr)\begin{pmatrix} F_u(k)\sin(t\sqrt{1+k^2}) \\ F_v(k)\cos(t\sqrt{1+k^2}) \end{pmatrix}, \tag{B 12}$$

$$v_\infty(r) = -\alpha\mu^{-2}[\beta^{-1}K_1(r/\beta) - K_1(r)] \tag{B 13}$$

for $t \geqslant r$, where

$$F_u(k) = \frac{\beta^2 k^2}{\sqrt{1+k^2}(1+\beta^2 k^2)}, \qquad F_v(k) = \frac{\beta^2 k^2}{(1+k^2)(1+\beta^2 k^2)}. \tag{B 14}$$

It can be verified that $v_\infty = \mathrm{d}\eta_\infty/\mathrm{d}r$ in accordance with geostrophy. The evaluation of (B 12) follows the procedure (B 10).

(*b*) *Particle trajectories*

The trajectories $r_\mathrm{L}(r_0, \theta_0, t), \theta_\mathrm{L}(r_0, \theta_0, t)$ of a particle initially at r_0, θ_0 is given by

$$\frac{\mathrm{d}r_\mathrm{L}}{\mathrm{d}t} = u(r_\mathrm{L}, t), \qquad r_\mathrm{L}\frac{\mathrm{d}\theta_\mathrm{L}}{\mathrm{d}t} = v(r_\mathrm{L}, t). \tag{B 15}$$

For the cylindrical geometry an analytical solution is limited to the case

$$r \ll \beta, \qquad t \leqslant r$$

for which

$$K_1(z) = z^{-1} + \tfrac{1}{2} z \log(\tfrac{1}{2}z) + \mathrm{order}(z),$$

which yields

$$r^2(r_0, t) = r_0^2 + 2\alpha\mu^{-2}(1 - \cos\mu t) \approx r_0^2 + \alpha t^3$$

for $\beta \approx 1$. We are here concerned with negative α, associated with an initial *inward* movement associated with the gravitational collapse. The 'front' passes at $t = r$, and is soon followed by a geostrophic regime $u \approx 0$, $v \approx v_\infty$. The trajectories have the appearance of circles with an initial stem. They do not resemble the observed spirals.

Consider a line of particles $r_0 = r_0(\theta_0)$ at $t = 0$. Then the Lagrangian solutions $r_\mathrm{L}(r_0(\theta_0), \theta_0, t), \theta_\mathrm{L}(r_0(\theta_0), \theta_0, t)$ at a *fixed time* describe the configuration $r_\mathrm{L}(\theta_0)$, $\theta_\mathrm{L}(\theta_0)$, or $r_\mathrm{L}(\theta_\mathrm{L})$, of the line initially at $r_0(\theta_0)$.

References

Afanasyev, Y. D. & Peltier, W. R. 1998 Three-dimensional instability of anticyclonic swirling flow in rotating fluids: laboratory experiments and related theoretical predictions. *Phys. Fluids* **10**, 3194–3202.

Apel, J. R., Gasparovic, R. F., Thompson, D. R. & Gotwolds, B. L. 1998 Signature of surface wave/internal wave interactions: experiment and theory. *Dyn. Atmos. Oceans* **12**, 89–106.

Bidokhti, A. A. & Tritton, D. J. 1992 The structure of a turbulent free shear layer in a rotating fluid. *J. Fluid Mech.* **241**, 469–502.

Bjerknes, V., Bjerknes, J., Solberg, H. & Bergeron, T. 1933 *Physikalische Hydrodynamik*. Springer.

Bluestein, H. B. 1993 *Synoptic-dynamic meteorology in midlatitudes*. Oxford University Press.

Boyer, D. L. & Davies, P. A. 1982 Flow past a circular cylinder on a β-plane. *Phil. Trans. R. Soc. Lond.* A **306**, 533–556.

Bresciano, S., Espedal, H. A., Jenkins, A. D. & Johannessen, O. M. 1998 On the occurrence of surface slicks in the oceans. NERSC Technical Report 152.

Bretherton, F. P. & Garrett, C. J. R. 1969 Wavetrains in inhomogeneous moving media. *Proc. R. Soc. Lond.* A **299**, 59–75.

Brown, G. L. & Roshko, A. 1974 On density effects and larger structure in turbulent mixing layer. *J. Fluid Mech.* **64**, 775–816.

Brown, R. A. 1980 Longitudinal instabilities and secondary flows in the planetary boundary layer: a review. *Rev. Geophys. Space Phys.* **18**, 683–697.

Bruce, J. G. 1995 Eddies southwest of Denmark Strait. *Deep-Sea Res.* I **42**, 13–29.

Brunt, D. 1927 The period of simple vertical oscillations in the atmosphere. *Q. J. R. Meteorol. Soc.* **53**, 30–32.

Corcos, G. M. & Sherman, F. S. 1976 Vorticity concentration and the dynamics of unstable free shear layers. *J. Fluid Mech.* **73**, 241–264.

Corcos, G. M. & Sherman, F. S. 1984 The mixing layer: deterministic models of a turbulent flow. Part I. Introduction and the two-dimensional flow. *J. Fluid Mech.* **139**, 29–65.

Cox, C. & Munk, W. 1954 Measurement of the roughness of the sea surface from photographs of the Sun's glitter. *J. Opt. Soc. Am.* **44**, 838–850.

Defant, A. 1949 Über interne Gezeitenwellen und ihre Stabilitätsbedingungen. *Arch. Met. Geophys. Bioklimatol.* **1**, 39–61.

Doyle, A. C. 1892 The adventure of Silver Blaze. *The Strand Magazine* (ed. G. Newnes) **4**, 645–660.

Drazin, P. G. & Reid, W. H. 1981 *Hydrodynamic stability.* Cambridge University Press.

Eldevik, T. & Dysthe, K. B. 1999 Short frontal waves: can frontal instabilities generate small scale spiral eddies. *Selected Papers of the ISOFRP* (ed. A. Zatsepin & A. Ostrovskii). UNESCO.

Espedal, H. A., Johannesson, O. M., Johannessen, J. A., Dano, E., Lyzenga, D. R. & Knust, J. C. 1998 COASTWATCH '95: ERS 1/2 SAR detection of natural film on the ocean surface. *J. Geophys. Res.* **103**, 24 969–24 982.

Etling, D. & Brown, R. A. 1993 Roll vortices in the planetary boundary layer: a review. *Boundary-Layer Meteorol.* **65**, 215–248.

Ewing, G. 1950 Relation between band slicks at the surface and internal waves in the sea. *Science* **111**, 91–94.

Flament, P. & Armi, L. 1985 A series of satellite images showing the development of shear instabilities. *Eos* **66**, 523.

Flament, P. & Armi, L. 2000 The shear, convergence and thermocline structure of a front. *J. Phys. Oceanogr.* **30**, 51–66.

Flament, P., Firing, J., Sawyer, M. & Trefois, C. 1994 Amplitude and horizontal structure of a large diurnal sea surface warming event during the Coastal Ocean Dynamics Experiment. *J. Phys. Oceanogr.* **24**, 124–139.

Garrett, C. J. R. 1976 Generation of Langmuir circulations by surface waves—a feedback mechanism. *J. Mar. Res.* **34**, 117–130.

Gasparovic, R. R., Apel, J. R. & Kasichke, E. S. 1988 An overview of the SAR internal wave signature experiment. *J. Geophys. Res.* **93**, 12 304–12 316.

Gerling, T. W. 1986 Structure of the surface wind field from the SEASAT SAR. *J. Geophys. Res.* **91**, 2308–2320.

Gill, A. E. 1982 *Atmosphere–ocean dynamics.* Academic.

Gradshteyn, I. S. & Ryzhik, I. M. 1965 *Table of integrals, series, and products.* Academic.

Hesselberg, Th. 1918 Über die Stabilitätsverhältnissen bei vertikalen Verschiebungen in der Atmosphäre und im Meer. *Ann. Hydr. Mar. Meteor.*, pp. 118–129.

Hide, R. 1977 On the effects of rotation on fluid motions in cylindrical containers of various shapes and topological characteristics. *Dyn. Atmos. Oceans* **27**, 243–256.

Hide, R. 1997 Experiments with rotating fluids. *Q. J. R. Meteorol. Soc.* **103**, 1–28.

Hoskins, B. J. & Bretherton, F. P. 1972 Atmosphere frontogenesis models: mathematical formulation and solution. *J. Atmos. Sci.* **29**, 11–37.

Iga, K. 1993 Reconsideration of Orlanski's instability theory of frontal waves. *J. Fluid Mech.* **255**, 213–236.

Johannessen, J. A., Digranes, G., Espedal, H., Johannessen, O. M. & Samue, P. 1994*a* *SAR ocean feature catalogue*. ESA SP-1174, European Space Agency.

Johannessen, J. A., Vachon, R. W. & Johannessen, O. M. 1994*b* ERS-1 SAR imaging of marine boundary layer processes. *Earth Observation Quart.* **46**, 1–5.

Johannessen, O. M., Johannessen, J. A., Morrison, J. H., Farrelly, B. A. & Svendsen, E. A. S. 1983 Oceanographic conditions in the marginal ice zone north of Svalbard in early fall 1979 with emphasis on mesoscale processes. *J. Geophys. Res.* **88**, 2755–2769.

Johannessen, O. M., Johannessen, J. A., Svendsen, E., Shuchman, R. A., Campbell, W. J. & Josberger, E. G. 1987 Ice edge eddies in the Fram Strait marginal ice zone. *Science* **236**, 427.

Johannessen, O. M., Campbell, W. J., Shuchman, R., Sandven, S., Gloersen, P., Johannessen, J. A., Josberger, E. G. & Haugan, P. M. 1992 *Microwave study programs of air–ice–ocean interactive processes in the seasonal ice zone of the Greenland and Barents Seas*. AGU Geophysical Monograph, vol. 68, ch. 13, pp. 261–289.

Kelvin, Lord 1880 On a disturbing infinity in Lord Rayleigh's solution for waves in a plane vortex stratum. *Nature* **23**, 45–46.

Kloosterziel, R. C. 1990 Barotropic vortices in a rotating fluid. PhD thesis, University of Utrecht, The Netherlands.

Lamb, H. 1932 *Hydrodynamics*. Cambridge University Press.

Lavrova, O., Mityagina, M. & Sabinin, K. 1998 Investigation of perturbing action of atmospheric and internal oceanic processes on the waved sea surface using ocean remote sensing data. *Proc. Conf. Oceans '98, 28 September – 10 October 1998, Nice*, pp. 629–633. IEEE Oceanic Engineering Society.

Leibovich, S. 1983 The form and dynamics of Langmuir circulations. *A. Rev. Fluid Mech.* **15**, 391–427.

Lesieur, M., Yanase, S. & Métais, O. 1991 Stabilizing and destabilizing effects of a solid-body rotation upon quasi-two-dimensional shear layers. *Phys. Fluids* A **3**, 403–407.

Lyzenga, D. R. & Marmorino, G. O. 1998 Measurement of surface currents using sequential synthetic aperture radar images of slick patterns near the edge of the Gulf Stream. *J. Geophys. Res.* **103**, 18 769–18 777.

MacDonald, I. R., Guinasso, Jr., N. L., Ackleson, S. G., Amos, J. F., Duckworth, R., Sassen, R. & Brooks, J. M. 1993 Natural oil slicks in the Gulf of Mexico. *J. Geophys. Res.* **98**, 16 351–16 364.

MacVean, M. K. & Woods, J. D. 1980 Redistribution of scalars during upper ocean frontogenesis: a numerical model. *Q. J. R. Meteorol. Soc.* **106**, 293–311.

Margules, M. 1904 Über die Beziehung zwischen Barometerschwankungen and Kontinuitätsgleichung. *Festschrift Ludwig Boltzmann*, pp. 585–589. Leipzig: J. A. Barth.

Métais, O., Flores, C., Yanase, S., Riley, J. J. & Lesieur, J. 1995 Rotating free-shear flows. Part 2. Numerical simulations. *J. Fluid Mech.* **293**, 47–80.

Milne-Thomson, L. M. 1960 *Theoretical hydrodynamics*, 4th edn. Macmillan.

Moum, J. N., Carlson, D. J. & Cowles, J. 1990 Sea slicks and surface strain. *Deep-Sea Res.* **37**, 767–775.

Ochadlick Jr, A. R., Cho, P. & Evans-Morgis, J. 1992 Synthetic aperture radar observations of currents colocated with slicks. *J. Geophys. Res.* **97**, 5325–5330.

Orlandi, P. & Carnevale, G. F. 1999 Evolution of isolated vortices in a rotating fluid of finite depth. *J. Fluid Mech.* **381**, 239–269.

Orlanski, I. 1968 Instability of frontal waves. *J. Atmos. Sci.* **25**, 178–200.

Palmén, E. & Newton, C. W. 1969 *Atmospheric circulation systems; their structure and physical interpretation*. Academic.

Pedley, T. J. 1969 On the stability of viscous flow in a rapidly rotating pipe. *J. Fluid Mech.* **36**, 177–222.

Peltzer, R. D., Griffin, O. M., Barger, W. R. & Kaiser, J. A. C. 1992 High-resolution measurements of surface-active film redistribution in ship wakes. *J. Geophys. Res.* **97**, 5231–5252.

Phillips, O. M. 1977 *The dynamics of the upper ocean*. Cambridge University Press.

Polvani, L. M., McWilliams, J. C., Spall, M. A. & Ford, R. 1994 The coherent structures of shallow-water turbulence: deformation-radius effect, cyclone/anticyclone asymmetry and gravity-wave generation. *Chaos* **4**, 177–186.

Potylitsin, P. G. & Peltier, W. R. 1998 Stratification effects on the stability of columnar vortices on the f-plane. *J. Fluid Mech.* **355**, 45–79.

Reynolds, O. 1880 On the effect of oil in destroying waves on the surface of water. *Br. Ass. Rep.* Papers 1, 409.

Rossby, C.-G. 1938 On the mutual adjustment of pressure and velocity distributions in certain simple current systems. *J. Mar. Res.* **1**, 15–28.

Rudnick, D. L. 1996 Intensive surveys of the Azores Front. 2. Inferring the geostrophic and vertical velocity fields. *J. Geophys. Res.* **101**, 16 291–16 303.

Rudnick, D. L. & Ferrari, R. 1999 Compensation of horizontal temperature and salinity gradients in the ocean mixed layer. *Science* **283**, 526–529.

Rudnick, D. L. & Luyten, J. R. 1996 Intensive surveys of the Azores Front. 1. Tracers and dynamics. *J. Geophys. Res.* **101**, 923–939.

Scully-Power, P. 1986 Navy Oceanographer Shuttle observations, STS 41-G Mission Report. Naval Underwater Systems Center, NUSC Technical Document 7611.

Shen, C. Y. & Evans, T. E. 1994 On vorticity shedding by unstable jets. *Dyn. Atmos. Oceans* **21**, 105–135.

Sheres, D. K., Kenyon, K. E., Bernstein, R. L. & Beardsley, R. C. 1985 Large horizontal surface velocity shears in the ocean obtained from images of refracting swell and *in situ* moored current data. *J. Geophys. Res.* **90**, 4943–4950.

Sherman, F. S. 1990 *Viscous flow*. McGraw-Hill.

Stevenson, R. E. 1989 Oceanography from the Space Shuttle. Office of Naval Research. The University Corporation for Atmospheric Research.

Stevenson, R. E. 1998 Spiral eddies: the discovery that changed the face of the oceans. *21st Century Sci. Technol.* **11**, 58–71.

Stevenson, R. E. 1999 A view from space: the discovery of nonlinear waves in the ocean's near surface layer. *21st Century Sci. Technol.* **12**, 34–47.

Stuart, J. T. 1967 On finite amplitude oscillations in laminar mixing layers. *J. Fluid Mech.* **29**, 417–440.

Tennekes, H. & Lumley, J. L. 1972 *A first course in turbulence*. MIT Press.

Thompson, T. W., Liu, W. T. & Weissman, D. E. 1983 Synthetic aperture radar observation of ocean roughness from rolls in an unstable marine boundary layer. *Geophys. Res. Lett.* **20**, 1172–1175.

Thorpe, S. A. 1995 Dynamic processes of transfer at the sea surface. *Progr. Oceanogr.* **35**, 315–352.

Tritton, D. J. 1992 Stabilization and destabilization of turbulent shear flow in a rotating fluid. *J. Fluid Mech.* **241**, 503–523.

Väisälä, V. 1925 Über die Wirkung der Windschwankungen auf die Pilotbeobachtungen. *Soc. Sci. Fenn. Commentat. Phys.-Math.* **2**(19), 19–37.

Whitehead, J. A., Stern, M. E., Flierl, G. R. & Klinger, B. A. 1990 Experimental observations of baroclinic eddies on a sloping bottom. *J. Geophys. Res.* **95**, 9585–9610.

Winant, C. D. & Browand, F. K. 1974 Vortex pairing: the mechanism of turbulent mixing—layer growth at moderate Reynolds numbers. *J. Fluid Mech.* **63**, 237–255.

Woodcock, A. H. 1942 Soaring over the open sea. *Sci. Mon.* **55**, 226–232.

Woods, J. D., Wiley, R. I. & Briscoe, M. G. 1977 Vertical circulation at fronts in the upper ocean. *A voyage of discovery* (ed. M. Angel). *Deep-Sea Res.* (Suppl.) **24**, 253–275.

Yoder, J. A., Ackleson, S. G., Barber, R. T., Flament, P. & Balch, W. M. 1994 A line in the sea. *Nature* **371**, 689–692.